UNIVERSIDADE FEDERAL DE SANTA CATARINA
CENTRO TECNOLÓGICO
DEPARTAMENTO DE ENGENHARIA MECÂNICA

Giuliano Luchetta Martins

Development of a methodology to evaluate radiometers equivalence and their behavior on overirradiance events

Florianópolis
2020

Giuliano Luchetta Martins

Development of a methodology to evaluate radiometers equivalence and their behavior on overirradiance events

Trabalho de Conclusão de Curso de graduação em Engenharia Mecânica da Universidade Federal de Santa Catarina, como requisito parcial para a obtenção do título de Bacharel em Engenharia Mecânica
Orientador: Prof. Ricardo Rüther, Ph.D.
Co-orientador: Sylvio Luiz Mantelli Neto, Dr. Eng.

Florianópolis
2020

Ficha de identificação da obra elaborada pelo autor,
através do Programa de Geração Automática da Biblioteca Universitária da UFSC.

Martins, Giuliano
Desenvolvimento de metodologia para avaliar a equivalência de radiômetros e caracterizá-los em relação a eventos de sobreirradiância / Giuliano Martins ; orientador, Ricardo Rüther, coorientador, Sylvio Luiz Mantelli Neto, 2020.
92 p.

Trabalho de Conclusão de Curso (graduação) - Universidade Federal de Santa Catarina, Centro Tecnológico, Graduação em Engenharia Mecânica, Florianópolis, 2020.

Inclui referências.

1. Engenharia Mecânica. 2. Piranômetro. 3. Comparação. 4. Performance. 5. Sobreirradiância. I. Rüther, Ricardo . II. Mantelli Neto, Sylvio Luiz. III. Universidade Federal de Santa Catarina. Graduação em Engenharia Mecânica. IV. Título.

Giuliano Luchetta Martins

Desenvolvimento de metodologia para avaliar a equivalência de radiômetros e caracterizá-los em relação a eventos de sobreirradiância

Este Trabalho de Conclusão de Curso foi julgado adequado para a obtenção do Título de Engenheiro Mecânico e aprovado em sua forma final pela Comissão Examinadora e pelo Curso de Graduação em Engenharia Mecânica da Universidade Federal de Santa Catarina.

_____

Prof. Carlos Enrique Niño Bohórquez, Dr. Eng.

Coordenador do Curso

Comissão Examinadora:

Documento assinado digitalmente
Ricardo Ruther
Data: 21/11/2020 13:29:33-0300
CPF: 388.223.850-04

_____

Prof. Ricardo Rüther, Ph.D.

Orientador

Universidade Federal de Santa Catarina

_____

Sylvio Luiz Mantelli Neto, Dr. Eng.

Co-Orientador

Instituto Nacional de Pesquisas Espaciais

SAULO\Saulo Guths

Assinado digitalmente por SAULO\Saulo Guths
DN: CN=SAULO\Saulo Guths
Razão: Eu sou o autor deste documento
Localização:
Data: 2020-11-23 08:58:06
Foxit Reader Versão: 9.0.1

_____

Prof. Saulo Güths, Dr. Eng.

Membro da Banca

Universidade Federal de Santa Catarina

_____

Lucas Rafael Do Nascimento, Dr. Eng.

Membro da Banca

Universidade Federal de Santa Catarina

Dedico esse trabalho à minha mãe, Margaret, por sempre me incentivar a seguir os meus objetivos, e por me mostrar, desde cedo, que tudo é possível, se for feito com amor e trabalho duro.

AGRADECIMENTOS

Primeiramente, gostaria de aos meus pais pelo incentivo e suporte aos meus estudos desde o início. Em especial à minha mãe, Margaret Groff, que sempre esteve ao meu lado me incentivando a seguir meus objetivos e dar o meu melhor, sempre.

Gostaria de agradecer meu orientador, Prof. Ricardo Rüther, pelo aconselhamento e liderança, não só no desenvolvimento desse trabalho, como também durante todo o meu trabalho no Fotovoltaica-UFSC.

Gostaria de agradecer meu coorientador, Dr. Sylvio Luiz Mantelli Neto, o qual teve grande influência na escolha e desenvolvimento do tópico dessa tese. Por sempre me incentivar a ser mais crítico com meus resultados e almejar sempre a excelência; sendo ele parte fundamental no meu crescente gosto pela estatística e radiometria, estando sempre disposto a sanar minhas dúvidas com toda a paciência e detalhamento necessário, atrelando sempre o conhecimento teórico as atividades práticas.

De maneira geral, mas não menos especial, gostaria de agradecer aos meus irmãos, familiares, colegas de trabalho, amigos e amigas que fizeram parte da minha vida durante esses anos de universidade. Que compartilharam comigo momentos inesquecíveis, e tornaram a jornada da universidade muito mais divertida e única.

No âmbito desse trabalho, gostaria de agradecer os meus queridos amigos Gabriel Rosolem e Rafael Campos, pelas suas contribuições no desenvolvimento desse trabalho. Além disso, gostaria de agradecer ao Dr. Mario Pó, por seu aconselhamento em relação ao desenvolvimento da metodologia, além de valiosas sugestões que vieram a tornar mais robustos os resultados obtidos nessa tese.

Por final, o autor gostaria de agradecer: à EKO Instruments por ter cedido o sensor MS-80, à Hukseflux por ter cedido o sensor SR20-T1, o que viabilizou a realização deste trabalho. Ao Instituto Nacional de Pesquisas Espaciais (INPE) pelo apoio técnico. Além disso, agradecer o apoio financeiro da entidade Agência Nacional de Energia Elétrica (ANEEL), e apoio por meio de projetos de P&D da ENGIE e CPFL.

"*A grandeza da vida não consiste*
em não cair nunca, mas em nos levantarmos
cada vez que caímos" (Nelson Mandela, 1994)

RESUMO

Este trabalho apresenta o desenvolvimento de duas metodologias complementares a fim de avaliar o desempenho de radiômetros e caracterizar o comportamento deles em relação a eventos de sobreirradiância, ou borda de nuvem, utilizando um ano de medições locais. O controle de qualidade dos dados foi baseado nas diretrizes da Baseline Surface Radiation Network (BSRN); além disso, foi proposta uma correção de offset usando a irradiância global horizontal (GHI) combinada, de um pireliômetro local, para irradiância normal direta (DNI) e um piranômetro, para irradiância horizontal difusa (DHI). Posteriormente, calculou-se a incerteza expandida de cada radiômetro, utilizando informações provenientes de trabalhos passados, certificados de calibração e fichas técnicas disponíveis, processo esse realizado por meio da ferramenta SOLARUN. Métricas de erro e ferramentas estatísticas foram implementadas, a fim de avaliar a precisão dos sensores em relação a uma referência, neste caso, um piranômetro Kipp & Zonen modelo SMP22 instalado em um rastreador solar Kipp & Zonen SOLYS2. Os pirânometros pertencentes a Classe A (ISO9060: 2018) apresentaram uma ótimo precisão, entretando, o piranômetro Delta-T, modelo SPN1, mostrou-se bastante impreciso e com uma incerteza de medição bastante elevada. Além disso, a célula de referência analisada, da fabricante IMT, também demonstrou-se imprecisa quando comparada com um radiômetro de referência, especialmente devido as suas diferentes respostas espectrais. A segunda metodologia propôs avaliar a identificação de eventos de borda de nuvem, e o tempo de resposta dos sensores. Posteriormente, elaborou-se um método para classificar os sensores avaliados, por meio das performances. O piranômetro MS-80, da Eko Instruments, foi o melhor classificado. Aspectos importantes também foram avaliados e discutidos, como a medida de irradiância extrema de 1845,5[W/m²], e a influência de eventos de sobreirradiância na energia acumulada ao longo do ano, que representa cerca de 0,7%; entretanto, esses eventos têm uma maior influência nos meses de verão e primavera. Portanto, problemas relacionados a eventos de extremos de sobreirradiância são mais prováveis de serem causados durante os meses com maior geração de energia para a cidade de Florianópolis, Brasil.

Palavras-chave: Piranômetro. Comparação. Performance. Sobreirradiância.

ABSTRACT

This work presents the development of two complementary methodologies to assess radiometers' accuracy performance and characterize their behavior in relation to overirradiance, or cloud enhancement, events, using one year of on-site data. The dataset quality check was done throughout Baseline Surface Radiation Network (BSRN) parameters; in addition, an offset correction was proposed using the combined global horizontal irradiance (GHI) from an on-site pyrheliometer, for direct normal irradiance (DNI) and a pyranometer, for diffuse horizontal irradiance (DHI). Afterward, each radiometer expanded uncertainty was calculated, using data from previous works, calibration certificates, and datasheets. This process was done with the assistance of SOLARUN tool. Furthermore, error metrics and statistical tools were used in order to assess the sensors' accuracy regarding a chosen reference, in this case, a Kipp & Zonen SMP22 pyranometer installed on a Kipp & Zonen tracker (SOLYS2). Class A radiometers had positive performances, however, poor results were found for Delta-T pyranometer, SPN1, and the analyzed IMT silicon photodiode. The second methodology proposed a quantitative assessment of cloud enhancement events identification and a qualitative evaluation of sensors' response time, throughout the calculation of the second derivative for each overirradiance situation. Afterward, both methodologies were executed, an evaluation metric was proposed in order to rank the sensors on-site. Thus, using the results obtained throughout this work to define which radiometers possess better characteristics to identify and properly measure overirradiance events. The best performance was achieved by Eko Instruments' MS-80. Other important aspects were assessed and discussed as well, such as an extreme irradiance measurement of 1845,5[W/m²] and the influence of overirradiance events on accumulated energy over the year, which represents around 0,7%; moreover, these events were found to have a higher frequency on summer and spring months. Therefore, issues related to extreme overirradiance events are more likely to be caused, during the months with higher energy generation, for the site of Florianópolis, Brazil.

Keywords: Pyranometer. Comparison. Performance. Overirradiance.

LIST OF FIGURES

Figure 1 - Fluxogram of the proposed methodology.....28
Figure 2 - Aerial image from radiometric station.....29
Figure 3 - Illustration of different day types. 34
Figure 4 - Expanded Uncertainty [%] in relation to Irradiance [W/m²] for one second time resolution. ((a) For sensor ***#A*** (SMP22); (b) For sensor ***#B*** (SMP22); (c) For sensor ***#C*** (SMP11); (d) For sensor ***#D*** (SR20-T1); (e) For sensor ***#E*** (MS-80); (f) For sensor ***#F*** (SPN1); (g) For sensor ***#G*** (SI02PT100)).....45
Figure 5 - Expanded Uncertainty [%] in relation to Irradiance [W/m²] for one minute average. ((a) For sensor ***#A*** (SMP22); (b) For sensor ***#B*** (SMP22); (c) For sensor ***#C*** (SMP11); (d) For sensor ***#D*** (SR20-T1); (e) For sensor ***#E*** (MS-80); (f) For sensor ***#F*** (SPN1); (g) For sensor ***#G*** (SI02PT100)).....47
Figure 6 - Expanded Uncertainty [%] in relation to Irradiance [W/m²] for fifteen minutes average. ((a) For sensor ***#A*** (SMP22); (b) For sensor ***#B*** (SMP22); (c) For sensor ***#C*** (SMP11); (d) For sensor ***#D*** (SR20-T1); (e) For sensor ***#E*** (MS-80); (f) For sensor ***#F*** (SPN1); (g) For sensor ***#G*** (SI02PT100)).....48
Figure 7 - Expanded Uncertainty [%] in relation to Irradiance [W/m²] for one average. ((a) For sensor ***#A*** (SMP22); (b) For sensor ***#B*** (SMP22); (c) For sensor ***#C*** (SMP11); (d) For sensor ***#D*** (SR20-T1); (e) For sensor ***#E*** (MS-80); (f) For sensor ***#F*** (SPN1); (g) For sensor ***#G*** (SI02PT100)).....49
Figure 8 – Expanded Uncertainty [%] in relation to Irradiance [W/m²] for one day average. ((a) For sensor ***#A*** (SMP22); (b) For sensor ***#B*** (SMP22); (c) For sensor ***#C*** (SMP11); (d) For sensor ***#D*** (SR20-T1); (e) For sensor ***#E*** (MS-80); (f) For sensor ***#F*** (SPN1); (g) For sensor ***#G*** (SI02PT100)).....50
Figure 9 – Expanded Uncertainty [%] in relation to Irradiance [W/m²] for one month average. ((a) For sensor ***#A*** (SMP22); (b) For sensor ***#B*** (SMP22); (c) For sensor ***#C*** (SMP11); (d) For sensor ***#D*** (SR20-T1); (e) For sensor ***#E*** (MS-80); (f) For sensor ***#F*** (SPN1); (g) For sensor ***#G*** (SI02PT100)).....51
Figure 10 – Scatterplots of each sensor in relation to reference ***#A*** (SMP22), for one second time resolution, colored in relation to day type; (For: (a) ***#B*** (SMP22); (b) ***#C*** (SMP11); (c) ***#D*** (SR20-T1); (d) ***#E*** (MS-80); (e) ***#F*** (SPN1); (f) ***#G*** (SI02PT100)).....53

Figure 11 - Scatterplots of each sensor in relation to reference #A (SMP22), for one minute average, colored in relation to day type; (For: (a) #B (SMP22); (b) #C (SMP11); (c) #D (SR20-T1); (d) #E (MS-80); (e) #F (SPN1); (f) #G (SI02PT100)). 53

Figure 12 - Scatterplots of each sensor in relation to reference #A (SMP22), for fifteen minutes average, colored in relation to day type; (For: (a) #B (SMP22); (b) #C (SMP11); (c) #D (SR20-T1); (d) #E (MS-80); (e) #F (SPN1); (f) #G (SI02PT100)). 54

Figure 13 - Scatterplots of each sensor in relation to reference #A (SMP22), for one hour time resolution, colored in relation to day type; (For: (a) #B (SMP22); (b) #C (SMP11); (c) #D (SR20-T1); (d) #E (MS-80); (e) #F (SPN1); (f) #G (SI02PT100)). 54

Figure 14 - Scatterplots of each sensor in relation to reference #A (SMP22), for one day average, colored in relation to day type; (For: (a) #B (SMP22); (b) #C (SMP11); (c) #D (SR20-T1); (d) #E (MS-80); (e) #F (SPN1); (f) #G (SI02PT100)). 55

Figure 15 - Scatterplots of each sensor in relation to reference #A (SMP22), for one month average; (For: (a) #B (SMP22); (b) #C (SMP11); (c) #D (SR20-T1); (d) #E (MS-80); (e) #F (SPN1); (f) #G (SI02PT100)). 56

Figure 16 - Percentual Error (PE) Boxplot graph for radiometers ***#B*** (SMP22), ***#C*** (SMP11), ***#D*** (SR20-T1), ***#E*** (MS-80), ***#F*** (SPN1), ***#G*** (SI02PT100). in relation to the reference (***#A*** (SMP22)), for one second time resolution..... 57

Figure 17 - Percentual Error (PE) Boxplot graph for radiometers ***#B*** (SMP22), ***#C*** (SMP11), ***#D*** (SR20-T1), ***#E*** (MS-80), ***#F*** (SPN1), ***#G*** (SI02PT100). in relation to the reference (***#A*** (SMP22)),for one minute average. 58

Figure 18 - Percentual Error (PE) Boxplot graph for radiometers ***#B*** (SMP22), ***#C*** (SMP11), ***#D*** (SR20-T1), ***#E*** (MS-80), ***#F*** (SPN1), ***#G*** (SI02PT100). in relation to the reference (***#A*** (SMP22)),for fifteen minutes time resolution. 58

Figure 19 - Percentual Error (PE) Boxplot graph for radiometers ***#B*** (SMP22), ***#C*** (SMP11), ***#D*** (SR20-T1), ***#E*** (MS-80), ***#F*** (SPN1), ***#G*** (SI02PT100). in relation to the reference (***#A*** (SMP22)), for one-hour average..... 59

Figure 20 - Percentual Error (PE) Boxplot graph for radiometers ***#B*** (SMP22), ***#C*** (SMP11), ***#D*** (SR20-T1), ***#E*** (MS-80), ***#F*** (SPN1), ***#G*** (SI02PT100). in relation to the reference (***#A*** (SMP22)),for one-day average. 59

Figure 21 - Percentual Error (PE) Boxplot graph for radiometers ***#B*** (SMP22), ***#C*** (SMP11), ***#D*** (SR20-T1), ***#E*** (MS-80), ***#F*** (SPN1), ***#G*** (SI02PT100). in relation to the reference (***#A*** (SMP22)),for one-month average..... 60

Figure 22 - Percentual Error (PE) in relation to Zenith Angle, for one second average, colored according to day type. (For: (a) ***#B*** (SMP22); (b) ***#C*** (SMP11); (c) ***#D*** (SR20-T1); (d) ***#E*** (MS-80); (e) ***#F*** (SPN1); (f) ***#G*** (SI02PT100)). 61

Figure 23 - Percentual Error (PE) in relation to Zenith Angle, for one-minute average, colored according to day type. (For: (a) ***#B*** (SMP22); (b) ***#C*** (SMP11); (c) ***#D*** (SR20-T1); (d) ***#E*** (MS-80); (e) ***#F*** (SPN1); (f) ***#G*** (SI02PT100)). 61

Figure 24 - Percentual Error (PE) in relation to Zenith Angle, for fifteen minutes average, colored according to day type. (For: (a) ***#B*** (SMP22); (b) ***#C*** (SMP11); (c) ***#D*** (SR20-T1); (d) ***#E*** (MS-80); (e) ***#F*** (SPN1); (f) ***#G*** (SI02PT100)). 62

Figure 25 - Percentual Error (PE) in relation to Zenith Angle, for one-hour average, colored according to day type. (For: (a) ***#B*** (SMP22); (b) ***#C*** (SMP11); (c) ***#D*** (SR20-T1); (d) ***#E*** (MS-80); (e) ***#F*** (SPN1); (f) ***#G*** (SI02PT100)). 62

Figure 26 - Daily data for the highest irradiance measurement (2018-11-11), for radiometers ***#A*** (SMP22), ***#B*** (SMP22), ***#C*** (SMP11), ***#D*** (SR20-T1), ***#E*** (MS-80), ***#F*** (SPN1), ***#G*** (SI02PT100). 71

Figure 27 - Approximate data for the highest irradiance measurement (2018-11-11) and its respective error bars, for radiometers ***#A*** (SMP22), ***#B*** (SMP22), ***#C*** (SMP11), ***#D*** (SR20-T1), ***#E*** (MS-80), ***#F*** (SPN1), ***#G*** (SI02PT100). 71

Figure 28 – Boxplot for measured irradiance during overirradiance events, for radiometers ***#A*** (SMP22), ***#B*** (SMP22), ***#C*** (SMP11), ***#D*** (SR20-T1), ***#E*** (MS-80), ***#F*** (SPN1), ***#G*** (SI02PT100). 73

Figure 29 – Boxplot for calculated kt_0 from measured irradiance during overirradiance events, for radiometers ***#A*** (SMP22), ***#B*** (SMP22), ***#C*** (SMP11), ***#D*** (SR20-T1), ***#E*** (MS-80), ***#F*** (SPN1), ***#G*** (SI02PT100). 73

Figure 30 - Boxplot for measured irradiance during extreme overirradiance events, for radiometers ***#A*** (SMP22), ***#B*** (SMP22), ***#C*** (SMP11), ***#D*** (SR20-T1), ***#E*** (MS-80), ***#F*** (SPN1), ***#G*** (SI02PT100). 75

Figure 31 - Boxplot for calculated kt0 from measured irradiance during extreme overirradiance events, for radiometers #A (SMP22), #B (SMP22), #C (SMP11), #D (SR20-T1), #E (MS-80), #F (SPN1), #G (SI02PT100). 76

Figure 32 - Scatterplots, relating the second derivate of each sensor to reference ***#G*** (SI02PT100), for overirradiance events. ((a) For sensor ***#A*** (SMP22); (b) For sensor ***#B*** (SMP22); (c) For sensor ***#C*** (SMP11); (d) For sensor ***#D*** (SR20-T1); (e) For sensor ***#E*** (MS-80); (f) For sensor ***#F*** (SPN1)). 77

Figure 33 - Scatterplots graphs, showing the average of the second derivative of each event. Relating each sensor to the reference ***#G*** (SI02PT100), for overirradiance events. ((a) For sensor ***#A*** (SMP22); (b) For sensor ***#B*** (SMP22); (c) For sensor ***#C*** (SMP11); (d) For sensor ***#D*** (SR20-T1); (e) For sensor ***#E*** (MS-80); (f) For sensor ***#F*** (SPN1)). 78

Figure 34 - Scatterplots, relating the second derivate of each sensor to reference ***#G*** (SI02PT100), for extreme overirradiance events. ((a) For sensor ***#A*** (SMP22); (b) For sensor ***#B*** (SMP22); (c) For sensor ***#C*** (SMP11); (d) For sensor ***#D*** (SR20-T1); (e) For sensor ***#E*** (MS-80); (f) For sensor ***#F*** (SPN1)). 79

Figure 35 - Scatterplots graphs, showing the average of the second derivative of each event. Relating each sensor to the reference ***#G*** (SI02PT100), for extreme overirradiance events. ((a) For sensor ***#A*** (SMP22); (b) For sensor ***#B*** (SMP22); (c) For sensor ***#C*** (SMP11); (d) For sensor ***#D*** (SR20-T1); (e) For sensor ***#E*** (MS-80); (f) For sensor ***#F*** (SPN1)). 80

LIST OF TABLES

Table 1 - Description of radiometers respective position in the radiometric station, models, manufacturers, and reading conditions. 29

Table 2 - Representation of each sensor model compliance with ISO9060:2018 and its sub-categories. 29

Table 3 - Main technical specifications of each radiometer model. 30

Table 4 - Sensor's uncertainty sources, for radiometers ***#A*** (SMP22), ***#B*** (SMP22), ***#C*** (SMP11), ***#D*** (SR20-T1), ***#E*** (MS-80), ***#F*** (SPN1), ***#G*** (SI02PT100). 35

Table 5 - Correlation for informed response time (95%) for each sensor. 39

Table 6 - Offset factor for each sensor according to combined GHI, for radiometers #A (SMP22), #B (SMP22), #C (SMP11), #D (SR20-T1), #E (MS-80), #F (SPN1), #G (SI02PT100). 44

Table 7 - Calculated Mean Expanded Uncertainty (%), for radiometers ***#A*** (SMP22), ***#B*** (SMP22), ***#C*** (SMP11), ***#D*** (SR20-T1), ***#E*** (MS-80), ***#F*** (SPN1), ***#G*** (SI02PT100). 52

Table 8 - Calculated Error metrics for complete dataset, for one-second time resolution, for radiometers ***#B*** (SMP22), ***#C*** (SMP11), ***#D*** (SR20-T1), ***#E*** (MS-80), ***#F*** (SPN1), ***#G*** (SI02PT100). 64

Table 9 - Calculated Error metrics for complete dataset, for one-minute time resolution, for radiometers ***#B*** (SMP22), ***#C*** (SMP11), ***#D*** (SR20-T1), ***#E*** (MS-80), ***#F*** (SPN1), ***#G*** (SI02PT100). 64

Table 10 - Calculated Error metrics for complete dataset, for fifteen minutes time resolution, for radiometers ***#B*** (SMP22), ***#C*** (SMP11), ***#D*** (SR20-T1), ***#E*** (MS-80), ***#F*** (SPN1), ***#G*** (SI02PT100). 64

Table 11 - Calculated Error metrics for complete dataset, for one-hour time resolution, for radiometers ***#B*** (SMP22), ***#C*** (SMP11), ***#D*** (SR20-T1), ***#E*** (MS-80), ***#F*** (SPN1), ***#G*** (SI02PT100). 65

Table 12 - Calculated Error metrics for complete dataset, for one-day time resolution, for radiometers ***#B*** (SMP22), ***#C*** (SMP11), ***#D*** (SR20-T1), ***#E*** (MS-80), ***#F*** (SPN1), ***#G*** (SI02PT100). 65

Table 13 - Calculated Error metrics for complete dataset, for one-month time resolution, for radiometers ***#B*** (SMP22), ***#C*** (SMP11), ***#D*** (SR20-T1), ***#E*** (MS-80), ***#F*** (SPN1), ***#G*** (SI02PT100). 65

Table 14 – Paired ratio hypothesis test results, for radiometers ***#B*** (SMP22), ***#C*** (SMP11), ***#D*** (SR20-T1), ***#E*** (MS-80), ***#F*** (SPN1), ***#G*** (SI02PT100) in relation to the reference (***#A*** (SMP22)). 67

Table 15 - Maximum irradiance measurement occurred in the dataset, for radiometers ***#A*** (SMP22), ***#B*** (SMP22), ***#C*** (SMP11), ***#D*** (SR20-T1), ***#E*** (MS-80), ***#F*** (SPN1), ***#G*** (SI02PT100), and its respective clearness index (kt_0). 70

Table 16 – Assessment of OIR events, their duration in minutes and total accumulated in hours of data observation period, for radiometers ***#A*** (SMP22), ***#B*** (SMP22), ***#C*** (SMP11), ***#D*** (SR20-T1), ***#E*** (MS-80), ***#F*** (SPN1), ***#G*** (SI02PT100). 72

Table 17 – Assessment of OIR events for specific time intervals, for radiometers ***#A*** (SMP22), ***#B*** (SMP22), ***#C*** (SMP11), ***#D*** (SR20-T1), ***#E*** (MS-80), ***#F*** (SPN1), ***#G*** (SI02PT100). 72

Table 18 - Assessment of EOIR events, their duration in minutes and total accumulated in hours of data observation period,, for radiometers ***#A*** (SMP22), ***#B*** (SMP22), ***#C*** (SMP11), ***#D*** (SR20-T1), ***#E*** (MS-80), ***#F*** (SPN1), ***#G*** (SI02PT100). 74

Table 19 - Assessment of EOIR events for specific time intervals, for radiometers ***#A*** (SMP22), ***#B*** (SMP22), ***#C*** (SMP11), ***#D*** (SR20-T1), ***#E*** (MS-80), ***#F*** (SPN1), ***#G*** (SI02PT100). 75

Table 20 - Respective position of each sensor in relation to the evaluation metric, for radiometers ***#A*** (SMP22), ***#B*** (SMP22), ***#C*** (SMP11), ***#D*** (SR20-T1), ***#E*** (MS-80), ***#F*** (SPN1). 82

Table 21 - Ranking for best behavior pyranometer in order to characterize overirradiance events, for radiometers ***#A*** (SMP22), ***#B*** (SMP22), ***#C*** (SMP11), ***#D*** (SR20-T1), ***#E*** (MS-80), ***#F*** (SPN1). 83

Table 22 - Percentual fraction of accumulated energy for general and extreme overirradiance events, stratified for each season, for measured data of pyranometer ***#E*** (MS-80). 83

Table 23 - Percentual fraction of accumulated energy for general and extreme overirradiance events, stratified for each season, for measured data of reference cell ***#G*** (SI02PT100). 84

LIST OF ABBREVIATIONS AND SYMBOLS

Abbreviations

AC	Alternate current
BSRN	Baseline Surface
CE	Cloud enhancement
CF	Correction factor
CI	Confidence interval
CSI	Clear sky irradiance [W/m²]
DC	Direct current
DHI	Diffuse Horizontal Irradiance [W/m²]
DNI	Direct Normal Irradiance [W/m²]
EOIR	Extreme overirradiance
ETH	Extraterrestrial horizontal irradiance [W/m²]
GHI	Global Horizontal Irradiance [W/m²]
GUM	Guide to the Expression of Uncertainty
INPE	Brazilian National Institute for Space research
IR	Infra-red
MAE	Mean absolute error
NREL	National Renewable Energy Laboratory
OIR	Overirradiance
PE	Percentual Error
PV	Photovoltaics
R^2	R-squared error
RMSE	Root mean squared error
SOLARUN	Solar Resource Uncertainty
SONDA	Brazilian national system of environmental data organization
STC	Standard Test Conditions

Symbols

AU	Earth-Sun distance in Astronomical Units
G_0	Solar constant [W/m²]
H_0	Null hypothesis
H_1	Alternative hypothesis
kt	Clear sky clearness index
kt_0	Extraterrestrial clearness index
n	Normalization
θ_z	Solar zenith angle
$\mu 0$	Cosine of solar zenith angle
$S0$	Solar constant at mean Earth-Sun distance
S_a	Solar constant adjusted for Earth-Sun distance
u_i	Standard uncertainty

u_c	Combined uncertainty
υ	Degree of freedom
υ_{eff}	Effective degree of freedom
$U_{exp,95}$	Expanded uncertainty
α	Significance level

SUMMARY

1 INTRODUCTION 15

1.1 MOTIVATION 15

1.2 OBJECTIVES 16

1.2.1 General objectives 16

1.2.2 Specific objectives 17

2 Literature Review 18

2.1 Radiation basic concepts 18

2.2 Statistical tools 18

2.2.1 Error Metrics 18

2.2.2 Hypothesis test 20

2.3 EQUIPMENT OPERATION 21

2.3.1 Thermopile Pyranometer 21

2.3.2 Silicon Photodiode 22

2.4 EQUIPMENT UNCERTAINTY SOURCES 23

2.4.1 Pyranometer 23

2.4.2 Silicon Photodiode 25

2.5 Cloud enhancement (CE) 25

3 Methodology 28

3.1 Data assessment 30

3.1.1 Data acquisition 30

3.1.2 Quality control 30

3.1.3 Data filtering 31

3.1.4 Offset correction 32

3.1.5 Day type definition 33

3.2 Uncertainty characterization 34

3.2.1 General Procedure 34

3.3 Equivalence verification method 37
3.3.1 Statistical analysis 37
3.3.2 Hypothesis test characterization 38
3.4 Overirradiance measurement characterization 39
3.4.1 Data normalization 40
3.4.2 Statistical analyses 40
3.4.3 Response Time assessment 41
3.4.4 Decision Factors 41
3.4.5 Characterize seasonal proportion of overirradiance events as % fraction accumulated energy over the year 42
4 Results and Discussion 43
4.1 Dataset 43
4.1.1 Quality control 43
4.1.2 Offset correction 43
4.2 Uncertainties 44
4.3 Sensor equivalence evaluation 52
4.3.1 Scatterplot variation 52
4.3.2 Percentual Error & Other Error Metrics 56
4.3.3 Hypothesis Test 66
4.4.2.1 Overirradiance (OIR) Events 72
4.4.2.2 Extreme Overirradiance (EOIR) Events 74
4.4.3 Response time assessment 77
4.4.3.1 Overirradiance (OIR) Events 77
4.4.3.2 Extreme Overirradiance (EOIR) Events 78
4.4.4 Results Overview 80
4.4.5 Seasonal proportion of overirradiance events as % fraction accumulated energy over the year 83

5 Conclusion 85
6 Recommendations for future works..... 86
REFERENCES 87

1 INTRODUCTION

Renewable energies are being used extensively to replace fossil fuel sources and are becoming more relevant in the world's energy mix. Photovoltaic energy has been integrated into generation systems in several countries, both centrally and in a distributed way. In order to assess the performance of these systems, solar irradiance sensors or radiometers are commonly used apparatus, which are also associated with solar resource assessment, monitoring, and forecasting. They are indispensable requirements in a photovoltaic (PV) power plant. The market has a wide variety of sensors with a wide range of prices, temporal, spectral response, etc. However, in addition to the characteristics mentioned in the catalogs and manuals, performance evaluation in the field is important to be able to analyze the cost-benefit relationship, and performance between them.

Another common problem in PV systems in subtropical regions is the impact of cloud cover. Clouds are responsible for the greatest source of variability in the solar resource, thus causing irradiance ramps and increasing irradiance variability, therefore generating great impact in renewable's grid integration (Denholm and Margolis, 2007a, 2007b)**.** In addition, due to local climatic conditions and multiple scattering in clouds, an enhancement of irradiance can be caused, which can exceed the extraterrestrial solar irradiation value. This phenomenon does not have a defined nomenclature in the literature and has been named diversely, described by words such as overirradiance, over-irradiance, cloud enhancement (CE), cloud edge, and cloud lensing (Balfour et al., 2011; Braga et al., 2020; do Nascimento et al., 2019; Gueymard, 2017a; Wirth et al., 2015). For this present work overirradiance (OIR) will be used to name the phenomena, in addition, the cloud enhancement term will be used for specific situations. OIR events can cause a series of problems such as overload in the inverters, premature burning in the fuses, and cascade shutdown of the protection circuits in large PV plants (Burger and Rüther, 2006; Chen et al., 2013; Luoma et al., 2012).

1.1 MOTIVATION

Due to the numerous varieties of radiometric sensors, and manufacturers, available in the market, properly evaluating their performance is essential to assure their claimed quality. Furthermore, several time resolutions datasets are required for different purposes. For instance: one second for OIR events identification; one minute, fifteen minutes, and one hour for PV

system performance evaluation and PV plant site certification; in addition, one day and one-month averages in order to calculate PV systems performance metrics, such as performance ratio and yield.

Furthermore, overirradiance events have been reported more constantly as pyranometers with a faster response time were introduced in monitoring stations. However, it is widely known that a thermopile cannot respond as fast as a photodiode to irradiance events. Thus, it still is uncertain how well pyranometers characterize overirradiance events, and which aspects are important for proper identification. On the other hand, silicon-based devices tend to have spectral and directional effects that will overestimate or underestimate overirradiance events. Therefore, neither of them presents an ideal solution for OIR events assessment.

1.2 OBJECTIVES

The present work has a two-fold objective. The first one, to characterize quantitatively, throughout statistical tools, how well is the general measurement performance of each pyranometer.

The second one is to characterize pyranometers' behavior in relation to overirradiance events, thus using quantitative and qualitative metrics to evaluate, for example, how well the phenomenon is being observed and how fast is the response time in comparison with the other sensors. In addition, the second methodology will aim to classify the sensors in accordance with their results, considering the results of the first methodology as well.

Moreover, important aspects such as extreme irradiance measurements and their percentual fraction of accumulated energy over the year will be assessed; however, this issue will not be the main focus of this work.

1.2.1 General objectives

a) Verify accuracy equivalence of different irradiance measurement sensors, for different time resolutions;
b) Characterize the performance of these radiometers to monitor overirradiance events, in order to state which one is the most capable measurement device to assess such events.

1.2.2 Specific objectives

a) Characterize each sensor's expanded uncertainty;
b) Develop a methodology to verify the sensor's measurement equivalency in relation to a reference;
c) Develop a methodology to characterize the behavior of irradiance sensors in relation to over irradiance events;
d) Determine which sensor best observes overirradiance events according to its behavior and accuracy.

2 LITERATURE REVIEW

2.1 RADIATION BASIC CONCEPTS

The measurement of radiation magnitudes is specially related to three complementary measurements. Direct or beam irradiance, which represents the direct radiation beams coming from the sun; diffuse irradiance, related to the refracted fraction of beams, usually caused due to reflection in clouds and scattering with atmospheric particles; and global irradiance, which is essentially the total irradiance observed, in the horizontal plane; thus, it can be represented as the sum of the direct and diffuse irradiance. Commonly, the units of irradiance are represented in W/m^2.

The integral of an irradiance curve represents the irradiation, or the amount of energy available at a certain point, for a specific period, and the common unit is kWh/m^2.

Since the diffuse fraction can vary along time, there is a classification regarding the different day types. Thus, a clear day represents a cloudless situation, thus ideally no radiation is reflected before reaching the earth's surface; partly cloudy and cloudy days would refer to days containing small or several amounts of clouds in the sky; however, direct radiation would still be available throughout this period; at last, the overcast classification is related to days with minimum or inexistence of direct radiation.

2.2 STATISTICAL TOOLS

Statistical tools are essential to support scientific conclusions and outcomes. This section will describe error metrics and further statistical tools which will be used in this work.

2.2.1 Error Metrics

Error metrics have been widely used to evaluate models and assess measurement performance in relation to a reference. Moreover, the error metrics utilized in this work are displayed in the following paragraphs. Which "R" and "O" are a representation of the reference and observed values respectively.

Root mean square error (RMSE) is the square root of the mean of the quadratic differences between reference and observed values. It measures the mean magnitude of the difference.

$$RMSE = \sqrt{\sum_{i=0}^{n} (R_i - O_i)^2} \tag{2.1}$$

Mean absolute error (MAE) describes the average deviation between reference and observed values.

$$MAE = \frac{1}{n} \sum_{i=0}^{n} |R_i - O_i| \tag{2.2}$$

Whilst MAE weights all differences equally, on the other hand, RMSE inputs greater weight to larger deviations (differences squared). Thus, MAE is always less than or equal to the RMSE, being equal only when the magnitude of the differences has the same deviation.

Mean bias error (MBE) represents the same feature as MAE. In addition, this metric illustrates the observed data bias in relation to the reference.

$$MBE = \frac{1}{n} \sum_{i=0}^{n} (R_i - O_i) \tag{2.3}$$

R squared (R^2) is a statistical metric that represents the proportion of the variance which is predictable; thus representing the observed accuracy in relation to the reference. It varies from 0% to 100%.

$$R^2 = \left(1 - \frac{\sum_{i=0}^{n} (R_i - O_i)^2}{\sum_{i=0}^{n} \left(R_{Avg} - O_i\right)^2}\right) * 100 \tag{2.4}$$

In order to compare equally all sorts of errors, they shall be normalized. Thus, the normalization will be defined as:

$$Normalization\ (n) = \frac{Error\ Metric}{R_{Avg}} \tag{2.5}$$

Furthermore, the equation for the percentual error is defined below.

$$Percentual\ Error\ (PE) = \left(\frac{R_i - O_i}{R_i}\right) * 100 \tag{2.6}$$

2.2.2 Hypothesis test

A statistical hypothesis is a statement about the parameters of one or more populations (Montgomery and Runger, 2014). To evaluate a population behavior or characteristic, a hypothesis is stated, commonly known as the null hypothesis (H_0). As a matter to evaluate the veracity of the claim, an alternative hypothesis (H_1) is formulated and taken into evaluation.

The decision tool to compare both hypotheses is declared Hypothesis Test, thus verifying if the statements are according to H_o or not. In order to do so, a confidence interval (CI) is defined, thus the comparison result is valid considering these limits. Therefore, there is a probability of wrongly accepting or rejecting the null hypothesis.

The probability of rejecting a truthful H_o is defined as a type I error. It can be evaluated through the interval's significance level (α). Furthermore, β-error applies whether the test accepts an erroneous H_o, which can be classified as a type II error. In the latter, supposing a mean test value evaluation, it will occur when the real sample value is within the critical boundaries region. The usual procedure is to use a significance level of 0,05 (Montgomery and Runger, 2014).

The null hypothesis will be defined as equality. Thus, alternative statements could be related to greater/smaller than, or both, determining and specific interval, this concept is called one-sided and two-sided hypothesis, respectively. For example, considering a population of sandbags, stating that H_o: μ = 100 g, and supposing H_1: μ > 100 g. Thus, it would be named as a one-sided situation. In this case, mean variations below 100g would not reject H_o. However, for the same situation, adding that H_2: μ < 100 g, thus creating a two-sided case. Therefore, the second would restrain the null hypothesis strictly to its equality, making any output different from 100g to reject the null hypothesis.

Moreover, P-value is an approach widely used in order to assess the test. Which is defined as the smallest level of significance that would lead to the rejection of the null hypothesis, within the given data. Thus, it can be more easily understood as the smallest level

α that the dataset is significant. Therefore, for a pre-defined α, if P-value < α the null hypothesis can be rejected.

2.3 EQUIPMENT OPERATION

2.3.1 Thermopile Pyranometer

A pyranometer is a radiometric sensor, commonly assessing the radiation values through a thermopile. A thermopile consists of a number of thermocouples connected in series underneath a black coating surface, thus incoming radiation can be absorbed for a wide wavelength range. Moreover, below the surface, there are two junctions located, the active (hot) and the passive (cold). The former is located just underneath the blackened surface, thus receiving the heat from external radiation. The latter is in thermal contact with the pyranometer's housing, which functions as a heat sink. To isolate the thermopile from external conditions, one, or two, optical glass domes encapsulate it. In addition, the dome acts as a filter for infrared (IR) radiation, for instance, a pyrgeometer will measure its counterpart, often used as a measure of the warming of the atmosphere.

Thus, the detector generates a voltage difference, proportionally to temperature variation between the hot and the cold junction. The calibration temperature should be around +20°C ("The Importance of Pyranometer Temperature Response - Kipp & Zonen," 2015). Thus, as field temperatures may vary, irradiance measurements should be compensated for temperature variations. However, the thermal offset has been diminished as thermopile technology improved. Therefore, the thermal effects are not as significant as they used to be, thus, the directional response has been increasing its contribution to pyranometers uncertainty.

Thermopile pyranometers have not always been suitable for short term measurements (< 1 minute). Its blackened surface implies thermal inertia which results in a rather slow response for abrupt radiation flux variations. Thus, fast step changes in irradiation can not be easily detected (Brinkworth and Hughes, 1976). Even though, several improvements were achieved throughout time, regarding new materials, components, and operational improvements; it is still not certain that thermopile pyranometers can measure fast irradiance events as well as other sensors, such as photodiode radiometers (Gueymard, 2017a).

Furthermore, the income of micro thermopile technology, which is already in use for infrared applications, could be a step forward to reduce thermopile's inertia. In addition, these

issues have been accessed regarding surface heat flux properties and sensing anisotropy properties, in order to improve efficiency. (Calaza et al., 2004; Singh et al., 2017; Thapa et al., 2012)

In addition, faster thermopiles have been brought to the market (Kipp & Zonnen, 2015), in conjunction with the implementation of digital sensors, which have a built-in processing system embarked and self-stored calibration data. However, it is important to notice that using digital data could cause output delays, due to preprocessing data before it is sent to the datalogger.

As a matter of fact, newer technologies have been brought into the market in order to improve pyranometers performance. One of the radiometers used in this work, MS-80, is described here as an example. Thus, typical for the Class A (former Secondary Standard) thermopile pyranometers are the double domes, which are applied to improve the thermal balance of the sensor and to lower the offset characteristics. The "high-end" pyranometers have domes made of expensive Quartz or Sapphire to reduce the offset uncertainty and are most commonly used for top research specific applications. While the compact MS-80 sensor has only a single glass dome, through clever optical design it is supposed to be immune to thermal offsets, which could contribute to its accurate fast response. Therefore, MS-80's performance rivals the top competition, while significantly less expensive. Without a second dome, the optic was designed to provide a true cosine response and flat spectral responsivity in the range 285nm –3000nm. Furthermore, the isolated thermopile detector is hermetically sealed and accommodated deep inside the sensor body to keep it thermally balanced. The long-term detector responsivity is enhanced and is no longer affected by long-term exposure to UV irradiance, humidity, and pressure fluctuations ("MS-80 Pyranometer | EKO Instruments," n.d.).

2.3.2 Silicon Photodiode

Photodiodes are one of the most basic radiation detectors, being its output a current proportionally to radiation's intensity, with an efficiency which is a function of wavelength (Canfield, 1999). Silicon photodiodes are a solid-state semiconductor device. Therefore, they operate based on the photoelectric principle; thus from a minimum point of incident energy in the semiconductor surface, the excited electrons are able to "jump" from the valence band to the conduction band. Thus, due to electrons concentration gradient, the absence and existence

of electrons in P-type and N-type regions result in a built-in voltage across the junction. (UDT Sensors Inc, 1982)

Furthermore, the inter-diffusion between these two junctions generates no free carriers region, named: depletion region. The interaction of built-in voltage and the depletion region results in an electric field within this region. Thus, the electron-hole pairs generated by radiation exciting electrons are drifted from the depleted region and collected by diffusion by the undepleted region, generating current, which is proportional to the radiation power. (UDT Sensors Inc, 1982)

It is widely known that the maximum output current is proportionally related to the semiconductor area available and on the incident irradiance levels. Therefore, photodiodes have a much smaller maximum irradiance trusted limit, whether pyranometers can assess confidently irradiances over 2000 $[W/m^2]$, reference cells limits are usually up to 1400 $[W/m^2]$ (IngineurBuro Mencke & Tegtmeyer GmbH, 2016).

Previous assessments have shown that silicon photodiodes measurement can deviate up to 4,8% in relation to thermopile pyranometers (Azouzoute et al., 2019), especially due to its shorter wavelength operation band. For the case of overirradiance events, as these deviations vary concerning temperature and radiation spectrum, it does not appear to interfere in the identification of such events, which can achieve values over 1800 $[W/m^2]$ depending on its location and environmental conditions (do Nascimento et al., 2019; Gueymard, 2017a). However, it is important to readdress the fact that, despite silicon photodiodes are extremely capable to identify variable conditions, in terms of quantifying the actual irradiance value there are larger errors associated with the transfer of calibration point of view and, again, instrument characteristics such as spectral and thermal responses.

2.4 EQUIPMENT UNCERTAINTY SOURCES

2.4.1 Pyranometer

There are several uncertainty sources related to pyranometer data. Considering that the output measurement is already temperature compensated, the following uncertainty sources will be discussed: zenith, azimuth, spectral, tilt and temperature response; calibration; measurement equipment (datalogger), and aging per year (Reda, 2011).

Zenith and azimuth response are commonly known as cosine errors. Thus, the combination of these features can be represented as the directional response. It occurs mainly due to imperfections of the glass dome, angular reflections of the blackened surface, and equipment's construction tolerances. It is known that this error increases exponentially for Zenith angles bigger than 80°, as well as previous research demonstrates that it has one of the biggest contributions to the pyranometer's expanded uncertainty (Konings and Habte, 2015; Kratzenberg et al., 2006; Reda, 2011).

Tilt response is related to the deviation of sensor's inclination during calibration. As it is stated by ISO 9847:1992 (International Organization for Standardization, 1998), the sensor can be calibrated through a reference in a specific tilt angle of interest. However, the manufacturers' pattern is to calibrate the pyranometer in a horizontal position, thus using different plans of array will generate uncertainty. Which is usually less than 0,2% for class A pyranometers and less than 1% for Class B and C[1].

The calibration uncertainty is available in every calibration certificate; in addition, it is recommended by the manufacturers a re-calibration every 2 years. The sensor is classified according to ISO9060 (International Organization for Standardization, 2018). Moreover, the procedures are normally in accordance with ISO 9847:1992 (International Organization for Standardization, 1998), performing the measurement referring to the World Radiometric Reference (WRR) according to the World Meteorological Organization (WMO) technical regulations.

The measurement device generates type B uncertainty, which must be assessed to evaluate data uncertainty completely. This uncertainty type represents the aleatory effects on the measurement system, especially regarding resolution and noise. It can be easily assessed throughout calibration certificates, datasheets, and data acquisition systems specifications (Albertazzi and Souza, 2013).

The aging of a sensor, or non-stability, represents the degradation of its value regarding calibration. One of its main reasons is the thermopile's blackened surface degradation throughout time. Even though manufactures recommend that calibration should be renewed every two years, previous studies have shown pyranometer calibration stability over decades (Nelson, 2006). However, degradation occurs and should be taken into account.

[1] Formerly known as secondary standard, first class and second class respectively.

Another important aspect to be taken into account is the non-linearity of response, thus the sensor's sensitivity varies according to the irradiance measured. This factor is generally assessed by manufacturers.

2.4.2 Silicon Photodiode

The uncertainty factors related to photodiode are very similar to the ones expressed in the previous section. Uncertainties regarding tilt response and calibration are very similar.

However, directional errors are minimized for silicon photodiodes, as they do not have a glass dome. Nevertheless, due to a reference cell physical construction, the response for high zenith angles is not very reliable, when the objective is to assess, realistically, the solar resource available.

Moreover, a silicon photodiode is much more susceptible to moisture ingress and chemical reactions reaching the p-n junction, corroborating to the equipment degradation, for this reason, non-stability becomes an important aspect when assessing uncertainty; nonetheless is not as higher as PV module degradation, because of a more careful assembling and special cares; however, it shall be properly considered in its expanded uncertainty.

Finally, another important aspect is the temperature. It has a strong influence on silicon cells, causing them to decrease efficiency, thus affecting measurements directly. Therefore, it is a common practice to use compensate measurements mathematically using the sensor's acquired temperature data.

2.5 CLOUD ENHANCEMENT (CE)

Cloud enhancement (CE) or overirradiance events implies an increase of irradiation on the earth's surface above extraterrestrial horizontal irradiance (ETH) level. With the recent and more widespread uptake of large-scale PV power plants in sunbelt countries prone to particular cloud patterns and distribution; the phenomenon is being discussed and assessed in the literature with renewed interest in recent years (Almeida et al., 2014; do Nascimento et al., 2019; Do Nascimento et al., 2020; Gueymard, 2017b, 2017a; Inman et al., 2016; Järvelä et al., 2020; Lappalainen and Kleissl, 2020; Norris, 1968; Vamvakas et al., 2020; Yordanov et al., 2015).

Overirradiance events take place when idiosyncratic physical interactions occur whilst radiation is on its way to the earth's surface. Normally, radiation would be attenuated, scattered, and reflected due to atmospheric components on its path. However, for partly cloudy and cloudy sky conditions it is possible to observe irradiances with an extraterrestrial clearness index (kt_0) bigger than one. Thus, clouds can scatter radiation to a certain point in the surface, which has already a sun clear observation. Therefore, both radiation effects are summed up, the direct and scattered one, registering a CE event. In addition, the second part is recorded as diffuse radiation, explaining the reason it cannot be accessed by a pyrheliometer (Suehrcke and McCormick, 1988).

Scattering can be defined as the physical process in which particles are obliged to deviate from their linear path due to non-uniformities of the region they are going through. The heterogeneous medium can be defined as the scattering center. Moreover, when analyzing radiation beams, a cloud can be defined as a group of centers; thus, being the main source for multiple scattering situations. Furthermore, as the number of random phenomena occurring simultaneously increases, the outcome unpredictability tends to be diminished, becoming a deterministic process, which could be modeled through diffusion theory (Haskell et al., 1994).

Furthermore, Maxwell's equations are composed of partial differential equations, which is an important component in the definition of classical optics and electromagnetism. Solutions were derived from these equations. Two of them are especially important related to atmospheric conditions, *Rayleigh's theory,* and *Mie Theory*. The former assumes that scattering particles are spherical, and their diameter is 20% smaller than the wavelength of incident radiation; this theory explained the blue sky's color under extremely clear conditions. The latter postulates that particle size is in the order of magnitude of incident radiation, which can be related to scattering in water vapor and dust particles (Iqbal, 1983).

Gustav Mie's solution is being considered as the main reason to cause overirradiance events. Occurring especially at small zenith angles and low-optical-depth clouds (Pecenak et al., 2016; Thuillier et al., 2013; Yordanov, 2015).

Cumulus cloud shapes are commonly related to cloud enhancement situations (Segal and Davis, 1992). Moreover, the cirrus cloud type is being evaluated as it could cause the same phenomena; however, its actual contribution regarding scattering events is not yet certain and is being discussed in the literature (Pecenak et al., 2016; Schade et al., 2007; Thuillier et al., 2013).

In recent years, several overirradiance events have been published, demonstrating that this event occurs in widely different climate conditions, altitudes, and latitude situations (Almeida et al., 2014; Braga et al., 2020; do Nascimento et al., 2019; Gueymard, 2017a; Inman et al., 2016; Vamvakas et al., 2020; Yordanov et al., 2015).

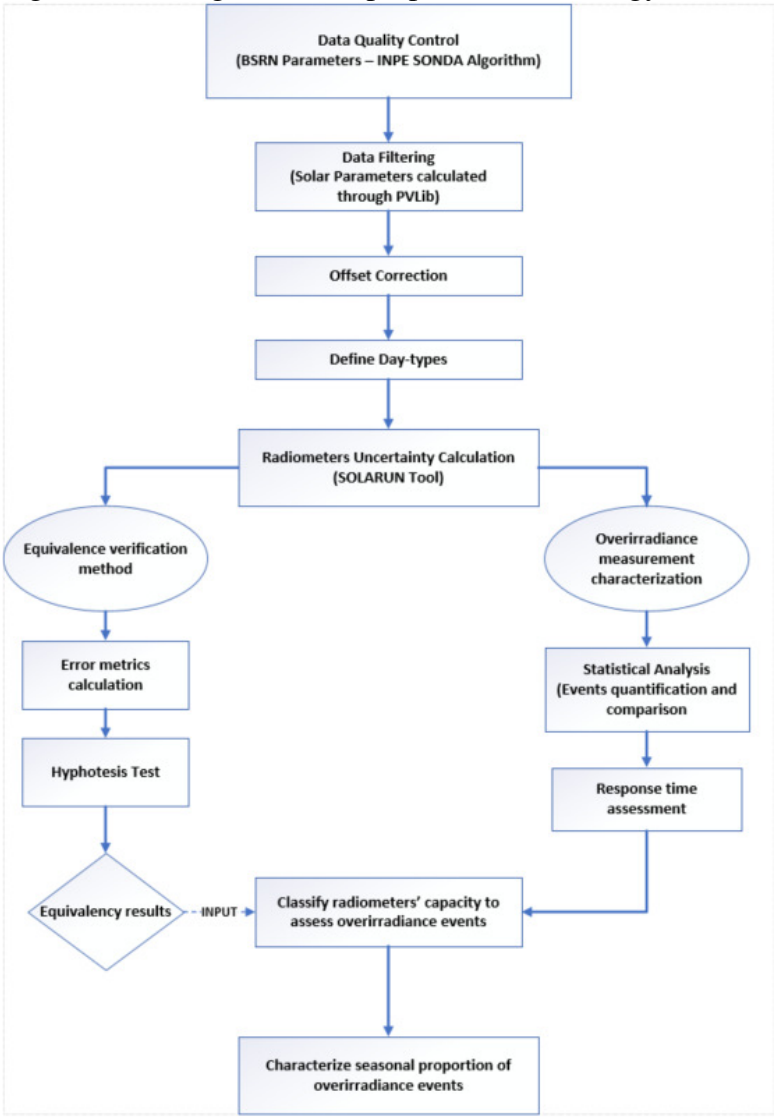
In addition, the effects of these events on photovoltaic (PV) applications are being broadly discussed. For instance, lasting long cloud enhancement events were evaluated to have a degrading impact on PV power plant components and operation and management (O&M). Thus, generating anomalous conditions, which are not foreseen by manufactures or standard test conditions (STC) values (do Nascimento et al., 2019; Ruther et al., 2017).

Recently, the energy contribution of overirradiance is being more carefully assessed. Even though these extreme measurements do not appear to affect the cumulative energy in some locations, tropical and subtropical areas appear to be heavily influenced by them (Braga et al., 2020; Inman et al., 2016; Lappalainen and Kleissl, 2020), with consequences in the operating conditions and DC-AC power conversion capabilities of inverters in large-scale PV power plants (do Nascimento et al., 2019; Ruther et al., 2017).

3 METHODOLOGY

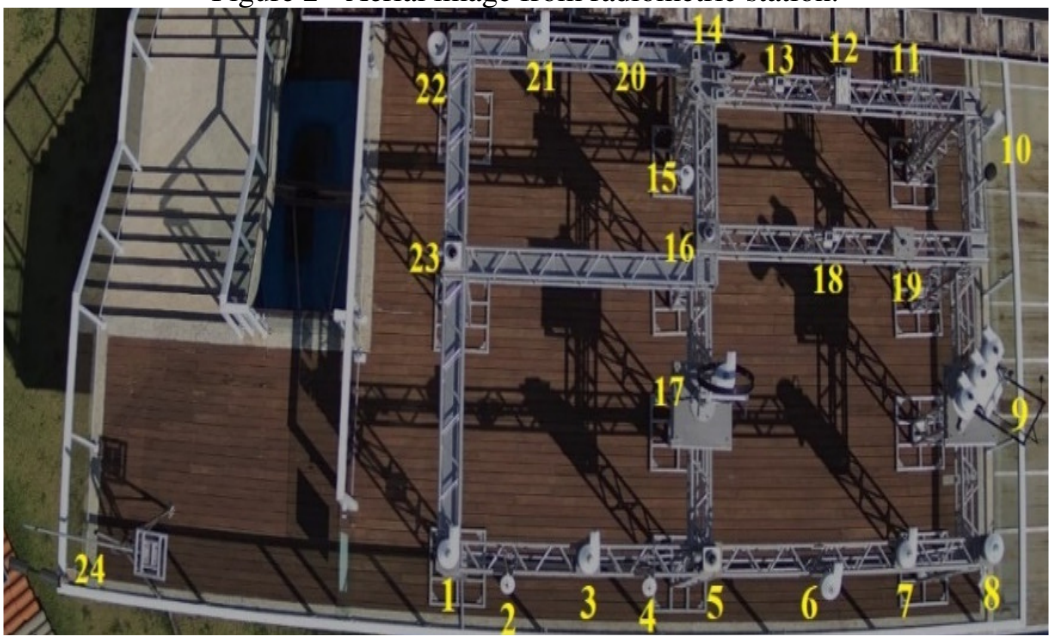
This chapter describes the procedures that will be carried out to compare seven radiometers, determine their accuracy equivalence, and evaluate their performance for assessing overirradiance events. The chapter starts by describing the monitoring station and all radiometers in the present study; furthermore, following the steps presented in Figure 1.

Figure 1 - Fluxogram of the proposed methodology



Source: Elaborate by the author

Figure 2 - Aerial image from radiometric station.



Source: elaborated by the author.

Table 1 - Description of radiometers respective position in the radiometric station, models, manufacturers, and reading conditions.

Sensor	*Position*	*Model*	*Manufacturer*	*Reading*
#A	9b	SMP22	Kipp&Zonnen	Digital
#B	7	SMP22	Kipp&Zonnen	Digital
#C	3	SMP11	Kipp&Zonnen	Digital
#D	20	SR20-T1	Hukseflux	Analog
#E	21	MS-80	EKO Instruments	Analog
#F	16	SPN1	Delta T	Analog
#G	11	SI02PT100	IMT	Analog

Source: elaborated by the author

Table 2 - Representation of each sensor model compliance with ISO9060:2018 and its sub-categories.

Model	*ISO 9060:2018 Class*	*Sub-Category "Fast response"*	*Sub-Category "Spectrally flat"*
SMP22	A	Not compliant	Compliant
SMP11	A	Not compliant	Compliant
SR20-T1	A	Not compliant	Compliant
MS-80	A	Compliant	Compliant
SPN1	C[1]	-	-
SI02PT100	-	-	-

Source: elaborated by the author

[1] Note: SPN1 has not been able to quote compliance with the new ISO9060:2018; however, for ISO9060:1990, the sensor is classified as a Second Class Pyranometer. This information was confirmed by private e-mail communication (Webb, 2020)

Table 3 - Main technical specifications of each radiometer model.

Model	*Response Time (95%)*	*Spectral range (50%)*	*Irradiance range*	*Temperature Operation range*
SMP22	< 2s	250 - 3500 nm	0 - 4000 [W/m²]	-40 to +80 °C
SMP11	< 2s	285 - 2800 nm	0 - 4000 [W/m²]	-40 to +80 °C
SR20-T1	< 4,5s	285 - 3000 nm	0 - 4000 [W/m²]	-40 to +80 °C
MS-80	< 0,5s	285 - 3000 nm	0 - 4000 [W/m²]	-40 to +80 °C
SPN1	<0,2s	400 - 2700 nm	>2000 [W/m²]	-40 to +70 °C
SI02PT100	< 1ms	350 - 1200 nm	0 - 1400 [W/m²]	-35 to +80 °C

Source: elaborated by the author

3.1 DATA ASSESSMENT

In this section data quality assessment will be discussed, alongside filtering parameters and offset corrections.

3.1.1 Data acquisition

The data is acquired on a one-second time basis throughout Campbell's dataloggers CR3000. Digital radiometers are read from Modbus port while analog ones are measured directly by differential channels. The one-second sampling resolution allows data to be averaged and stored to the desired time resolution such as one, 10, 15 minutes, along with maximum, minimum, and standard deviation of the intervals.

A more comprehensive characterization of the measurement systems and their relations to each other was already carried out and published in previous works and will not be reassessed in this text (Mantelli et al., 2020).

3.1.2 Quality control

Baseline Surface Radiation Network (BSRN) has developed quality check parameters to assess data anomalies. These metrics were developed in order to accommodate most of the

existing latitudes and climates (LONG; DUTTON, https://bsrn.awi.de/fileadmin/user_upload/bsrn.awi.de/Publications/BSRN_recommended_QC_tests_V2.pdf). These equations are widely used for data validation. Besides, they are used by the Brazilian National Space Institute INPE's SONDA network to assess their several radiometric stations ("SONDA - Validação dos Dados", ("SONDA - Validação dos Dados," http://sonda.ccst.inpe.br/infos/validacao.html).

The algorithm used here for data assessment was inspired by the one currently in use in the SONDA project. Thus, impossible events and rare ones were flagged individually. The equations are described below:

Global irradiance rare limit:

$$GHI_{Rare,limit} = S_a * 1{,}2 * \mu_0^{1,2} + 50 \text{ [W/m²]} \quad (3.1)$$

Global irradiance physically possible limit:

$$GHI_{Physical,limit} = S_a * 1{,}5 * \mu_0^{1,2} + 100_{\text{[W/m²]}} \quad (3.2)$$

Where:

θ_z = Solar zenith angle

$\mu 0 = Cos\ (\theta_z)$, if $\theta_z > 90°$, then $Cos\ (\theta_z) = 0$

S0 = solar constant at mean Earth-Sun distance

AU = Earth-Sun distance in Astronomical Units

S_a = *S0*/*AU2* = solar constant adjusted for Earth-Sun distance

3.1.3 Data filtering

According to BSRN quality check, impossible events will be filtered out from the dataset; however, rare ones will be analyzed carefully, as they could represent an overirradiance event.

Moreover, the zenith angle for the site was calculated, throughout PVlib ("Package Overview — pvlib-python 0.7.2+0.gb35905a.dirty documentation", https://pvlib-python.readthedocs.io/en/stable/_modules/) python library. Which is a well-known open-source tool for photovoltaics purposes, which has been developed mainly by Sandia National

Laboratories (“Sandia National Laboratories: Exceptional Service in the National Interest”, https://www.sandia.gov/), University of Arizona (“Institute for Energy Solutions |”, https://www.environment.arizona.edu/projects/institute-energy-solutions), alongside with python’s community and other users.

Diffuse irradiation can occur until zenith angles equal 95°, due to radiation refraction and reflection. However, as a PV system requires a certain amount of irradiation to generate energy and, in order to diminish directional errors from radiometric sensors, which are known to increase exponentially after 80° of zenith, literature is commonly imposing limit values between 80° - 85° of zenith angle (Gueymard, 2017a). In this paper, the imposed limit will be 80°, since it is the last cosine error evaluated in the calibration procedure by the manufactures.

3.1.4 Offset correction

As the calibration process occurs in different sites, and usually throughout different data acquisition systems. This causes small systematic differences, and the present work proposes an offset correction to equalize data output.

Three common clear day data for all sensors will be acquired, for one-second resolution. Furthermore, all sensors will be compared with a combination of direct normal and diffuse irradiance. On-site, there is a DNI (SHP1) and a DHI (SMP22) radiometers assembled on a solar tracker (SOLYS2) with a shading ball. Using the GHI combined will allow the sensors to be compared evenly; for instance, if they were corrected using one of the pyranometer’s data, it could have biased the results.

Moreover, the combined GHI is defined by the equation below:

$$GHI_{Combined} = DNI * Cos(\theta_Z) + DHI \quad (3.3)$$

Where:

DNI: Direct normal irradiance

DHI: Diffuse horizontal irradiance

Cos(θ_Z): Cosine of the zenith angle

An iteration best curve fit will be made for each day, determining a correction factor (CF) (International Organization for Standardization, 1998). Initially, a CF is supposed to correct the data of the observed sensor, afterward, the R^2 between reference and corrected values

are calculated. This procedure is repeated until a maximum R^2 value is achieved, thus determining the ideal CF for that specific clear day. The final CFs are averaged and applied to the rest of the dataset.

3.1.5 Day type definition

In order to have a better understanding of data behavior due to different sky conditions, each day type was individually classified as Clear, Partly Cloudy, Cloudy, and Overcast (Dittmann et al., 2011).

The day types assessed are ideally illustrated in Figure 3, for a one-minute time resolution. Thus, a clear sky day would be represented by a constant curve, without irradiation ramps; the partly cloudy condition possess several irradiance variations during the day, however, major or minor constant global irradiance situations are visible; cloudy days do not present any constant pattern during the day, in addition, the irradiance still has a significant magnitude, showing that direct irradiance influences during the day; moreover, overcast days are related only to diffuse irradiance, presenting very low irradiance magnitude throughout the whole day.

In order to facilitate the evaluation of the day types, the clear sky clearness index (kt) was used. Utilizing the clear sky irradiance model (CSI) create by Ineichen and Perez (Ineichen and Perez, 2002).

The kt formulation is displayed below:

$$kt_i = \frac{GHI_i}{CSI_i} \tag{3.4}$$

Where:

i: represents the line number of the dataset;

GHI: Global Horizontal Irradiance;

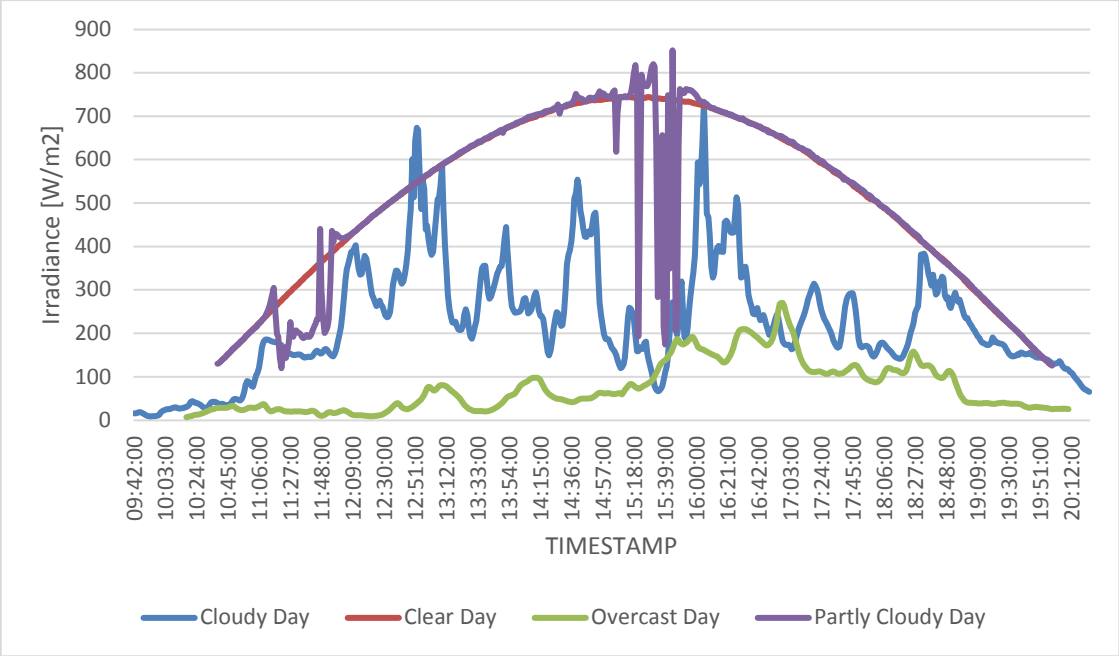
CSI: Clear Sky Irradiance;

kt: Clearness index, based on a clear sky model;

Thus, the daily average kt was calculated for each day. A $kt_{sup} = 0{,}45$ and $kt_{inf} = 0{,}25$ were defined (Iqbal, 1983). Thus, if $kt > kt_{sup}$ it would be defined as a partly cloudy day; for $kt < kt_{inf}$ the day type would be considered overcast; therefore, the other ones would be cloudy

days. Moreover, the partly cloudy days were analyzed individually in a plotted graph to define whether it was a clear day or not. In addition, as this model was not yet validated in the literature, each day was evaluated individually, by graphical illustration, to assure it had the correct classification.

Figure 3 - Illustration of different day types.



Source: elaborated by the author

3.2 UNCERTAINTY CHARACTERIZATION

Sensors uncertainties will be calculated based on the Guide to the Expression of Uncertainty (GUM) Method. In order to simplify the process and assure the quality of calculations, the SOLARUN tool (National Renewable Energy Laboratory (NREL), 2019) will be used. Since it was developed by National Renewable Energy Laboratory (NREL) researchers and it has been successfully validated several times (Habte et al., 2014; Konings and Habte, 2015; Reda, 2011; Reda et al., 2008).

3.2.1 General Procedure

Initially, data information was collected from the respective sensor calibration certificates and datasheets. In the case of missing information, the worst-case scenario was

assumed, in comparison to the other radiometers or referred to ISO9060:2018 (International Organization for Standardization, 2018).

In addition, for those who had a cosine error survey, the maximum error of it was taken to define the directional response. This is a conservative approach since there is no validated cosine error model to specify its error variation properly. Moreover, for sensor ***#A***, as it is located in a solar tracker, the average of the southern azimuth was considered. In our case, latitude below zero, the sensors are turned towards the north and its cable south. Thus, as all of these sensors surveys occurred in northern regions, their results must be mirrored. For the silicon photodiode (***#G***) no directional error was considered, because of zenith angle filter below 80°, the irradiance measurement is not likely to be affected due to its flat glass plate geometry.

Furthermore, the measurement acquisition system uncertainties were obtained as reported in previous work (Mantelli et al., 2020), then the values were also uploaded to the table. Even though zero offsets should be considered an uncertainty source, the SOLARUN tool does not take them into account. Therefore, they will not be considered; however, these offsets do not play an important role in higher irradiances magnitudes (Konings and Habte, 2015), which are especially important for PV systems and one of the main focus of this work (overirradiance events).

Table 4 - Sensor's uncertainty sources, for radiometers ***#A*** (SMP22), ***#B*** (SMP22), ***#C*** (SMP11), ***#D*** (SR20-T1), ***#E*** (MS-80), ***#F*** (SPN1), ***#G*** (SI02PT100).

Sensor	*Sensitivity*	*Calibration*	*Non-Stability*	*Non-Linearity*	*Temperature response*	*Directional response*	*Measurement Setup*
#A	11,17 µV/(W/m²)	0,81%	0,50%	0,20%	0,30%	0,74%	0,1 [W/m²]
#B	11,07 µV/(W/m²)	0,81%	0,50%	0,20%	0,30%	0,61%	0,1 [W/m²]
#C	8,69 µV/(W/m²)	1,35%	0,50%	0,20%	2%	2%	0,1 [W/m²]
#D	17,72 µV/(W/m²)	1,20%	0,80%	0,50%	1%	2%	0,94 [W/m²]
#E	11,103 µV/(W/m²)	0,63%	0,30%	0,20%	0,29%	1,82%	1,62 [W/m²]
#F	1 mV/(W/m²)	8% ± 10 [W/m²]	3,00%	1%	4%	5%	10,65 [W/m²]
#G	55,55 µV/(W/m²)	0,75%	0,50%	0,10%	3%	0%	1,7 [W/m²]

Source: elaborated by the author

All the following uncertainty sources are considered to have a rectangular distribution and symmetric shape, except for the calibration one, which has a normal distribution. This information is in accordance with ISO9060:2018 specifications.

The analytic equations for calculating the uncertainty are described below (Albertazzi and Souza, 2013):

The standard uncertainty (u_i) will be dictated by each distribution case.

For normal, infinite degrees of freedom:

$$u_i = \frac{U_{i,95}}{2} \tag{3.5}$$

For rectangular, infinite degrees of freedom:

$$u_i = \frac{U_{i,95}}{\sqrt{3}} \tag{3.6}$$

Furthermore, the combined uncertainty (u_c) must be calculated throughout the general case:

$${u_c}^2(G) = \sum (\frac{\partial f}{\partial X_i} u_i)^2 \tag{3.7}$$

Then, the effective freedom degree (ϑ_{eff}) can be calculated:

$$\frac{u_c^4}{\vartheta_{eff}} = \sum \frac{u_i^4(i)}{\vartheta_i} \tag{3.8}$$

Finally, being able to calculate the expanded final uncertainty ($U_{exp,95}$), being "t" the value of t-student related to ϑ_{eff} for a 95% interval of confidence:

$$U_{exp,95} = t * u_c \tag{3.9}$$

Thus, it will be applied to every individual value, then the expanded uncertainty for the whole dataset can be calculated.

In order to calculate the uncertainty for further time resolutions, the procedure remains the same for type B sources. Normally, type A uncertainties should be taken into account when assessing averaged values. However, irradiance is a variable measurand, having deviations even

on a millisecond basis, thus the individual values cannot be considered repeated observations (Konings and Habte, 2015). Therefore, the standard deviation will not be taken into account when assessing radiometric sensors' uncertainty.

Since other temporal resolutions are calculated with an average of its second, and the usual approach is to evaluate independently the mean value output, for that specific time resolution. Thus, the uncertainty assessment procedure will remain unchanged for different time resolutions.

3.3 EQUIVALENCE VERIFICATION METHOD

This method will aim to evaluate data equivalency among seven different radiometric sensors, with respect to a reference. The reference sensor will be chosen not only due to its final uncertainty but the physical position as well.

In this setup, it will be sensor ***#A***, since it is one of the most accurate sensors on-site and it is also located on the solar tracker (SOLYS2), without any nearby obstructions and due to the equipment's movement, reducing directional error azimuthal variability. Therefore, it is considered to be the most stable and accurate sensor on site.

In addition, it will be done for six different time resolutions: one second, one minute, fifteen minutes, one hour, one day, one month. Thus, covering several business and research applications related to solar radiation and energy measurements.

3.3.1 Statistical analysis

In order to analyze data behavior in relation to the equations proposed in section 2.2.1 will be applied to the six sensors with respect to reference ***#A***.

The percentual error (PE) will be plotted in relation to the solar zenith angle and throughout a boxplot, in order to evaluate the deviations according to different angles, especially in different cloud cover day type situations. The boxplot will illustrate constant variations and how large their interval is. For instance, it is important to notice that using PE could mislead the analysis for small magnitude data, since dividing a variation with small numbers would lead to high percentual results, thus outputting high errors for non-relevant data. Nevertheless, these minor values are reduced due to the imposed maximum zenith angle, some

of them will still be present due to overcast days. However, they are not the main focus of this work and will be identified as outliers.

Furthermore, a table with relevant statistical features, such as normalized error metrics will be displayed for all temporal resolutions. Naturally, the table will be stratified for each time resolution.

3.3.2 Hypothesis test characterization

As was stated in section 2.2.2 the hypothesis test can be used in order to evaluate the veracity of a supposition over a whole population. Here, the H_0 will be: "*The sensor does NOT present equivalent measurement data in relation to the reference*". Thus, our alternative hypothesis is H_1: "*The sensor presents equivalent measurement data in relation to the reference"*. "Equivalent" is defined here as: The observed sensor generates irradiance measurement within the pre-defined boundaries of the reference output data. The boundary limit will be defined by the reference radiometer's expanded uncertainty. Thus, supposing its expanded uncertainty is 1%, its upper limit would be 1,01 and the lower limit would be 0,99.

The known behavior of radiation data makes it not suitable for all types of hypothesis tests. Irradiance data is highly variable. Thus, absolute differences between reference and observed values vary significantly throughout a dataset.

Even though the paired mean difference test is most usually used to assess if the statement is in accordance with the interval of confidence, it would not be the best alternative in this case. Since it is based on the standard deviation of the differences(MINITAB LLC, 2020a), the unstable pattern of absolute variations in the irradiance dataset could mislead the final conclusion. In addition, situations such as overirradiance events would corroborate to an inequivalence output.

Therefore, the paired ratio average test can be considered the most suitable solution in order to evaluate irradiance data. Its interval of confidence is based on the covariance between reference and observation, along with each standard deviation (MINITAB LLC, 2020b). Even though this specific test was not found to be used in the literature to validate irradiance sensors measurements, equivalence tests are a well-known robust statistical tool and have been used in research throughout the years in order to validate hypotheses (Hauschke et al., 1999; Kaminski et al., 2010; King et al., 2020).

In this situation, a two-sided hypothesis will be defined. Thus, the ratio variation should be bigger than the reference's expanded uncertainty, for a 95% confidence interval, in order to neglect H_0.

Therefore, the hypothesis test will be the main criterion to define sensor equivalence. However, the other error metrics shall be taken into account when evaluating the situation regarding different sky conditions and directional response; thus, demonstrating other important characteristics of the sensors which would not be possible to assess with a single test.

3.4 OVERIRRADIANCE MEASUREMENT CHARACTERIZATION

This section will discuss the methodology to characterize overirradiance measurement sensors' behavior. Previous data treatment and analysis will be considered in order to access their capacity regarding cloud enhancement events.

For this section, as response time is extremely relevant, the determined reference will be sensor ***#G***. It is important to note that although its uncertainty is higher than most Class A pyranometers, its response time is almost instantaneous, representing a very important feature whilst analyzing cloud enhancement events steep irradiance ramps.

Table 5 - Correlation for informed response time (95%) for each sensor.

Sensor	*Model*	*ISO 9060 Class*	*Response Time (95%)*
#A	SMP22	A	< 2s
#B	SMP22	A	< 2s
#C	SMP11	A	< 2s
#D	SR20-T1	A	< 4,5s
#E	MS-80	A	< 0,5s
#F	SPN1	C[1]	< 0,2s
#G	SI02PT100	-	< 1ms

[1] Note: SPN1 has not been able to quote compliance with the new ISO9060:2018; however, for ISO9060:1990, the sensor is classified as a Second Class Pyranometer. This information was confirmed by private e-mail communication (Webb, 2020)

Source: elaborated by the author

The table above illustrates the response time (95%) for all sensors used in this work. All information was obtained from sensors datasheets available on the internet.

3.4.1 Data normalization

The extraterrestrial clearness index (kt_0) can be calculated through the division of measured global horizontal irradiance (GHI) and the extraterrestrial horizontal irradiance (ETH) (Gueymard, 2017a).

$$kt_{0_i} = \frac{GHI_i}{ETH_i} \tag{3.10}$$

Where:

i: represents the line number of the dataset;

GHI: Global Horizontal Irradiance;

ETH: Extraterrestrial Horizontal Irradiance;

Kt_0: Extraterrestrial Clearness index, based on an extraterrestrial model;

Thus, kt_0 will be calculated for the whole dataset and filtered for $kt_0 > 1$, in order to identify overirradiance events.

Furthermore, extreme overirradiance events will also be defined in this work. They will be identified when kt_0 is bigger than one and the GHI is bigger than the solar constant (G_0). Nevertheless, it is not strictly constant, G_0 value in this work will be related to the amount of solar power flux which goes through the mean Earth's orbit. Thus, having a value of 1367 $_{[W/m^2]}$ (Piacentini et al., 2011, 2003; Yordanov et al., 2014).

Pyranometers can measure up to $4000_{[W/m^2]}$ irradiance values. However, photodiodes have a much higher limitation, in our case, the trustable maximum measurement point is at $1400_{[W/m^2]}$ (IngineurBuro Mencke & Tegtmeyer GmbH, 2016). However, the sensor has been observed to measure above this limit. As overirradiance events are reported to go occasionally over the photodiode's maximum point (do Nascimento et al., 2019; Gueymard, 2017a), these specific events above the sensor's maximum trusted points will be evaluated carefully.

3.4.2 Statistical analyses

Statistical analyses will be done for both overirradiance and extreme overirradiance events. As photodiodes are known to have inherent deviation to pyranometers measurements,

for instance, related to the difference in spectral range, thus individual results will not be directly compared.

The amount of identified events will be compared, alongside their lasting time. An overirradiance event is defined in this work as a sequential time series of measured irradiance above kt_0, whilst the extreme one is analogous; however, with GHI bigger than G_0. In addition, an event will begin in the first second before an (extreme) overirradiance measurement occurs, and will end in the second after the last (extreme) overirradiance value in the sequence is measured.

3.4.3 Response Time assessment

In order to evaluate how fast the sensors are regarding the reference, the second-order derivative will be calculated for each individual overirradiance measurement, and the average for each event will be done as well.

The second derivate represents how much a value rate is variating. Therefore, it will allow us to observe qualitatively how similar to the reference a sensor responds to an event, on the same environmental conditions. The smaller the difference between both second derivatives, the closer the response behavior of both sensors would be.

Moreover, a second-order derivative is defined by:

$$\frac{d^2 f(x)}{dx^2} = \lim_{\Delta x \to 0} \frac{f(x + 2\Delta x) - 2f(x + \Delta x) + f(x)}{\Delta x^2} \tag{3.11}$$

3.4.4 Decision Factors

This methodology aims to provide a stratified ranking of the best sensor to observe general and extreme overirradiance events. Therefore, a ranking will be proposed according to their results.

There will be four evaluation metrics: Expanded Uncertainty, Phenomena Observation, Response Time, and Equivalency. For the first three metrics, the sensors will be ranked from first until sixth according to their performance, thus it will attribute points from 10 to 0, according to each respective position, thus: 1^{st} = 10,2^{nd} = 8, 3^{rd} = 6, etc. In addition, if the sensor was able to claim equivalency to reference ***#A***, it will be attributed 10 points. Therefore,

the points will be summed and the pyranometers will be ranked from the highest point equipment to the lowest.

3.4.5 Characterize seasonal proportion of overirradiance events as % fraction accumulated energy over the year

Furthermore, the overirradiance events will be gathered and stratified, in order to assess their percentual contribution to the total accumulated energy over the year. In addition, it will be evaluated for each season. This specific subsection will be evaluated only for the best-ranked pyranometer and **#G**.

4 RESULTS AND DISCUSSION

This chapter demonstrates and discusses the results of the proposed analyses from section 3.

4.1 DATASET

This section is related to the data treatment and qualification performed in the evaluated dataset.

4.1.1 Quality control

The dataset comprises one-second resolution data starting on 2018-08-01 and finishing on 2019-09-01. In the case of further temporal resolutions, its mean value was taken according to its specifications. As this work aims to evaluate sensors with paired data, anomalous data from one sensor automatically eliminates the entire sample for a specific time.

The data quality was assessed according to BSRN parameters, as described in section 3.1.2, the impossible values were instantly eliminated and the rare ones were evaluated separately. For instance, there were no flagged impossible values, moreover, the majority of rare ones were posteriorly identified as overirradiance events.

Furthermore, the zenith angles for each instant were calculated and merged into the dataset. Thus, it was filtered for values below 80°.

Internally, the laboratory keeps an up to date logbook of all events related to the radiometric station, such as routine maintenance, power outage, and eventual failures. Therefore, the logbook details were analyzed for this specific period and used to identify possible anomalous data. As a matter of fact, in February 2019 the station went through a monthly maintenance period. Thus, the dataset for this specific month has only two days of high-quality data.

4.1.2 Offset correction

Afterward, three clear sky days were manually selected. As stated in section 3.1.4, an iteration was made to fit the combined GHI and the observed curve. A fit iteration occurred

repeatedly until the maximum R^2 value was achieved. Then, the correction value was extracted. This process was repeated for each sensor and each clear day. In order to obtain the final offset factor, an average for the three respective days was made

Table 6 - Offset factor for each sensor according to combined GHI, for radiometers #A (SMP22), #B (SMP22), #C (SMP11), #D (SR20-T1), #E (MS-80), #F (SPN1), #G (SI02PT100).

Sensor	Offset factor
#A	0,9626
#B	0,9654
#C	0,9708
#D	0,9921
#E	0,9881
#F	1,0008
#G	1,0349

Source: elaborated by the author

Observing the offset factors obtained at one second temporal resolution, it is possible to infer that all sensors are quite accurate, generating slightly small deviations from their reference. As expected, one of the biggest variations was due to the photodiode, which can be simply explained due to its different spectral range. In addition, the digitally measured sensors appear to be slightly overestimating measurements, by effects of this work, these values will be considered to be corrected by the proposed offset, as a formal calibration in a certified institution would not be possible within this work time span. Furthermore, as clear days were selected to assess these measurements, variation features such as response time would not interfere in the offset calculation, as irradiance ramps and fast variations do not happen.

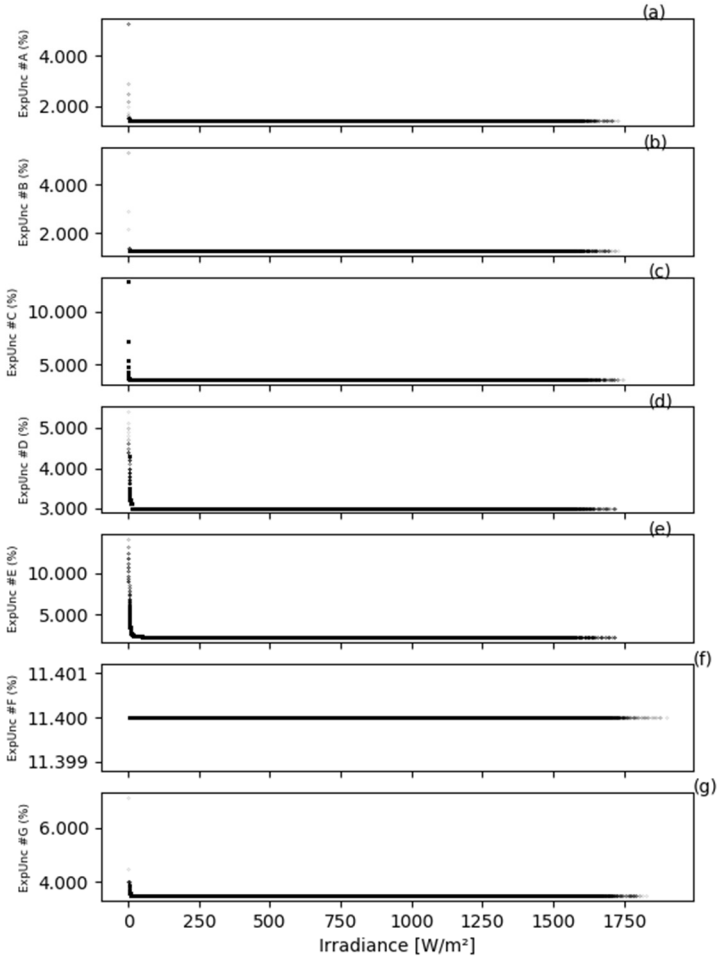
Furthermore, the offset factor was applied to each respective sensor and all data analyses were based on data considering this factor.

4.2 UNCERTAINTIES

The uncertainties were assessed for all time resolutions, according to what was explained in section 3.2. Some important assumptions were made, such as considering the directional error as constant, being represented as the average of its measured errors, or in case of information unavailability, it was considered the worst-case from the other radiometers.

Thus, the values in Table 4 were inserted into SOLARUN Application (National Renewable Energy Laboratory (NREL), 2019). Furthermore, the treated datasets for each time resolution were inserted to calculate each specific expanded uncertainty. The expanded uncertainty (%) relative to its respective irradiance is illustrated throughout scatterplot graphs, for each time resolution.

Figure 4 - Expanded Uncertainty [%] in relation to Irradiance [W/m²] for one second time resolution. ((a) For sensor ***#A*** (SMP22); (b) For sensor ***#B*** (SMP22); (c) For sensor ***#C*** (SMP11); (d) For sensor ***#D*** (SR20-T1); (e) For sensor ***#E*** (MS-80); (f) For sensor ***#F*** (SPN1); (g) For sensor ***#G*** (SI02PT100)).



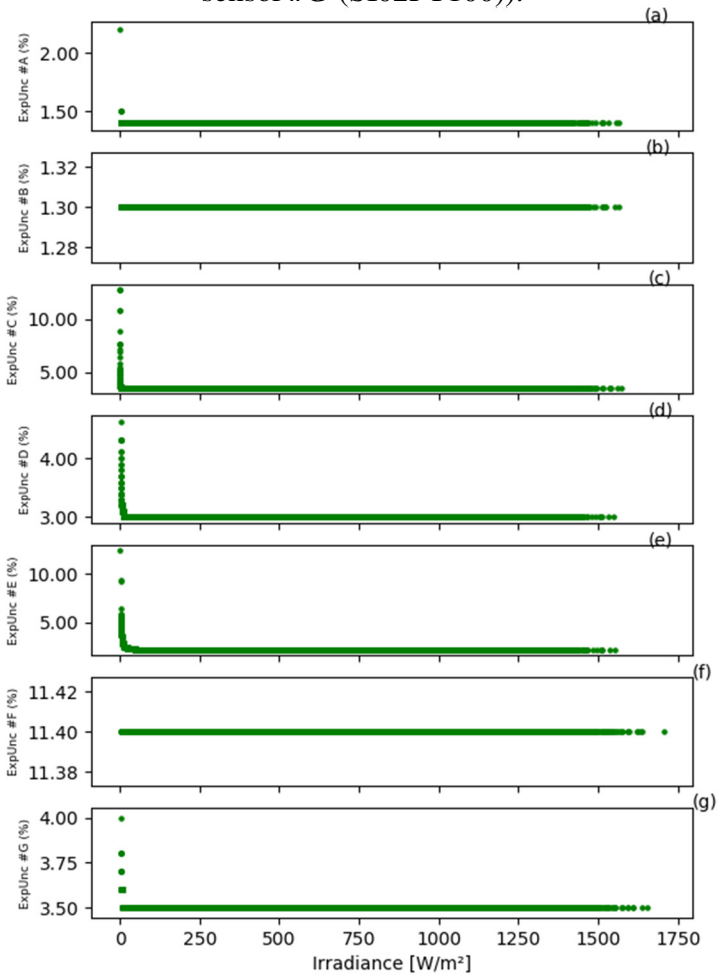
Source: elaborated by the author

As expected, due to the assumptions made, the percentual expanded uncertainty maintains roughly constant throughout irradiance variation, for all sensors. However, for very low irradiance values ($< 25_{[W/m^2]}$) the uncertainty increases drastically, for most of the sensors. This phenomenon is directly related to the data acquisition system's uncertainty, even though

it is not significantly high, very precise sensors, such as MS-80 (***#E***) and SR-20T1 (***#D***), suffer a strong effect due to its absolute nature; for instance, MS-80's system uncertainty of $1{,}62\ _{[W/m^2]}$ would represent 6,5% of an $25_{[W/m^2]}$ measurement, as the other uncertainty sources are significantly low, the system's uncertainty has its contribution increased in low irradiance situations Thus, as the overall uncertainty is small, the absolute data acquisition's uncertainty imposes a significant increase, in the percentual form, for minor irradiance measurements.

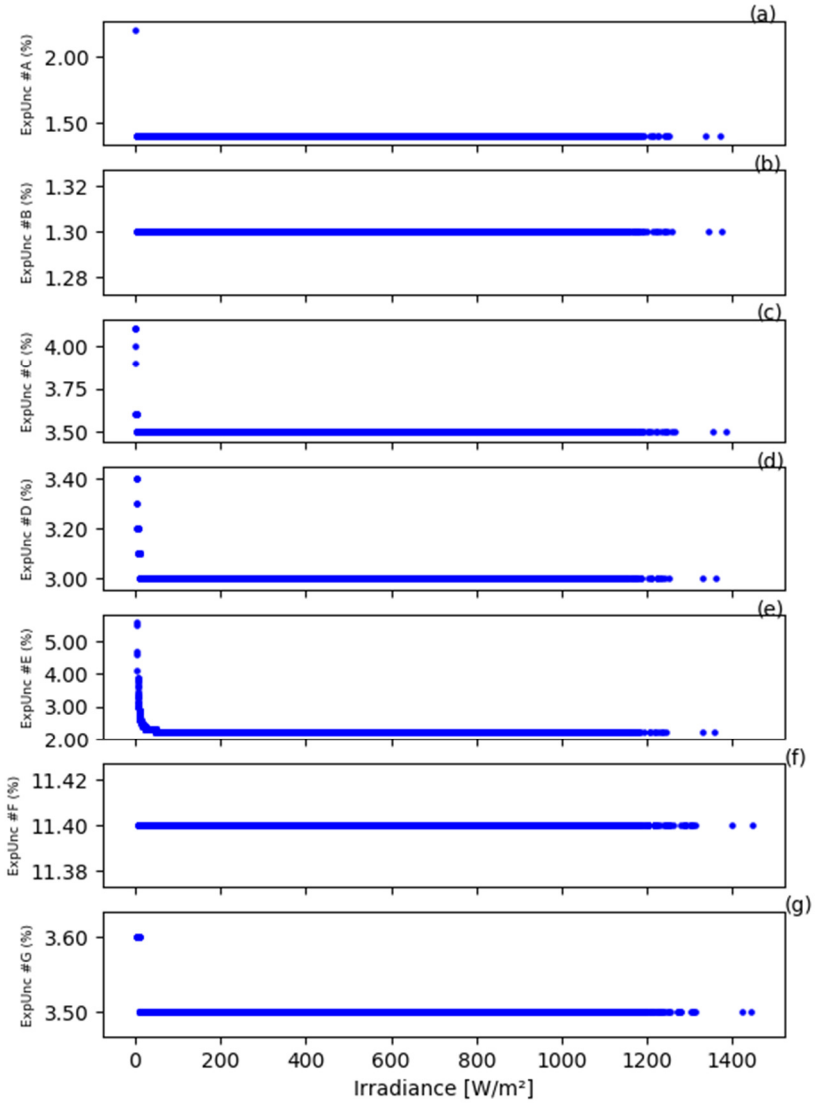
In addition, it is important to state that this information was not available for sensors digitally measured (***#A, #B, #C***) (Mantelli et al., 2020). Therefore, it is reasonable to infer, that their real uncertainties at low irradiances could be much higher than what was calculated in this work. In the case of sensor ***#F***, all of its uncertainties are already significantly high; thus, the influence of the data acquisition system is diminished and does not impose a great deviation in the expanded uncertainty, for low measurements.

Figure 5 - Expanded Uncertainty [%] in relation to Irradiance [W/m²] for one minute average. ((a) For sensor ***#A*** (SMP22); (b) For sensor ***#B*** (SMP22); (c) For sensor ***#C*** (SMP11); (d) For sensor ***#D*** (SR20-T1); (e) For sensor ***#E*** (MS-80); (f) For sensor ***#F*** (SPN1); (g) For sensor ***#G*** (SI02PT100)).



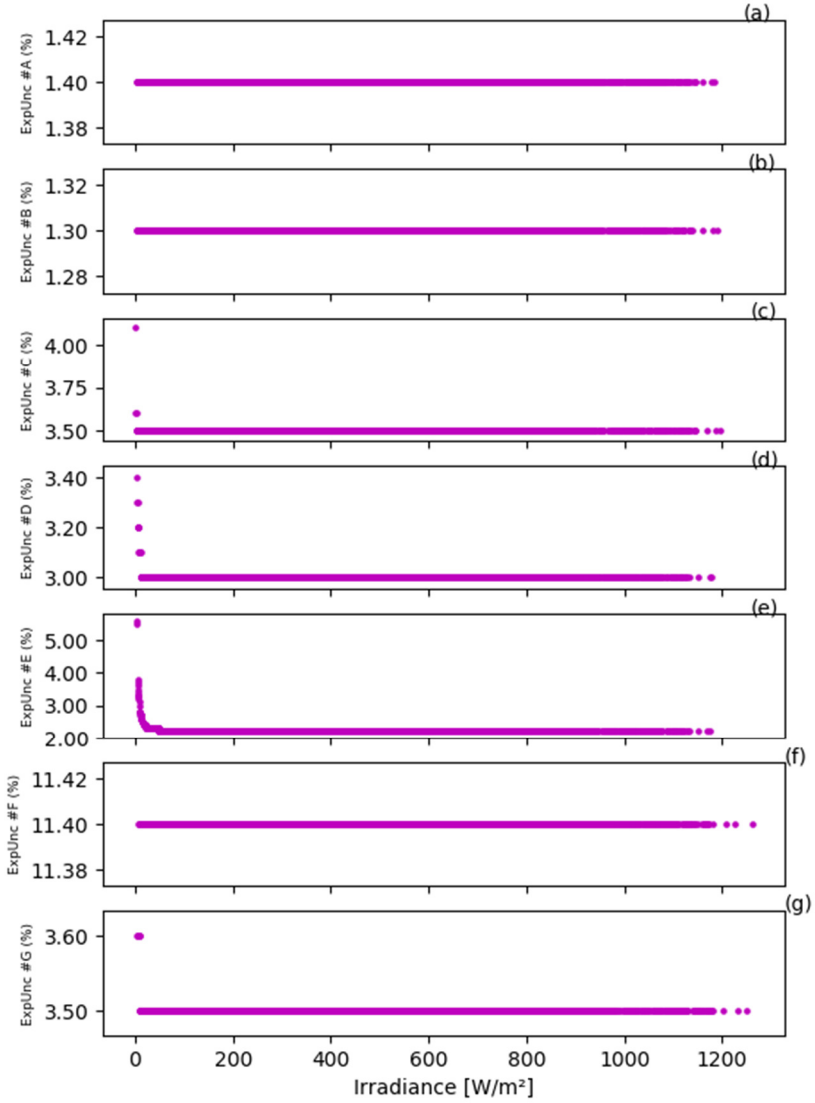
Source: elaborated by the author

Figure 6 - Expanded Uncertainty [%] in relation to Irradiance [W/m²] for fifteen minutes average. ((a) For sensor ***#A*** (SMP22); (b) For sensor ***#B*** (SMP22); (c) For sensor ***#C*** (SMP11); (d) For sensor ***#D*** (SR20-T1); (e) For sensor ***#E*** (MS-80); (f) For sensor ***#F*** (SPN1); (g) For sensor ***#G*** (SI02PT100)).



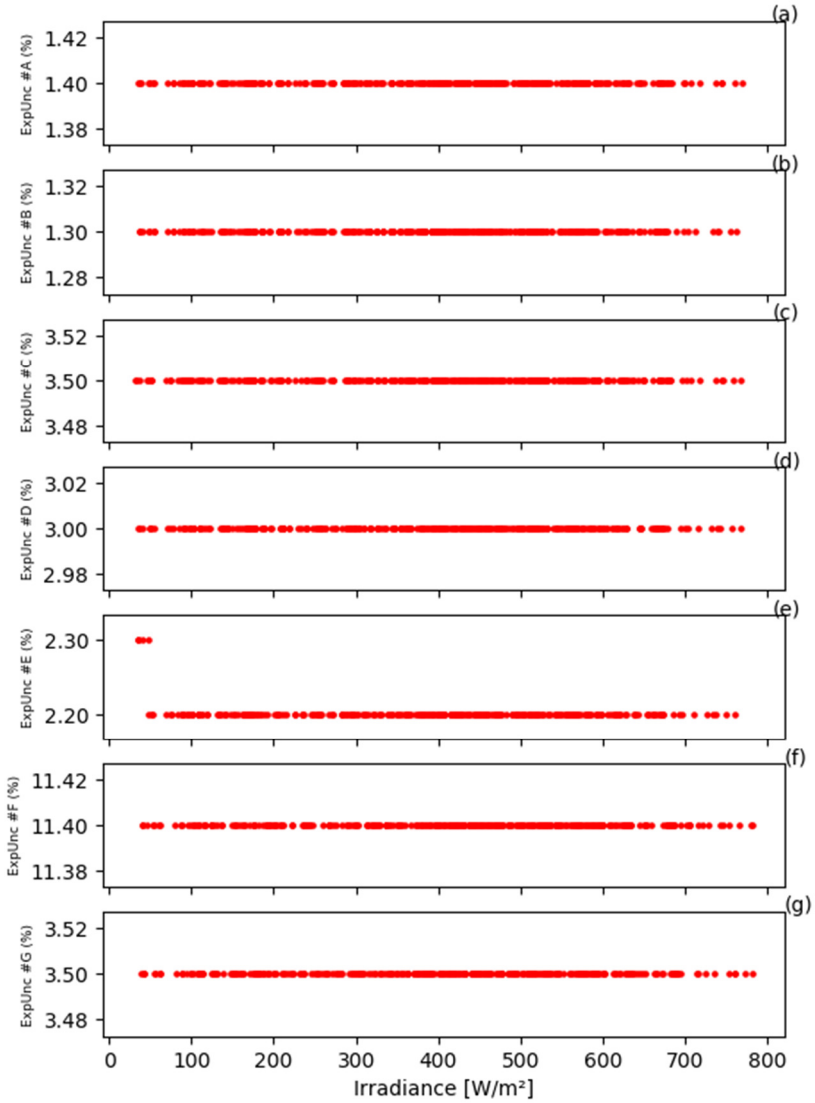
Source: elaborated by the author

Figure 7 - Expanded Uncertainty [%] in relation to Irradiance [W/m²] for one average. ((a) For sensor ***#A*** (SMP22); (b) For sensor ***#B*** (SMP22); (c) For sensor ***#C*** (SMP11); (d) For sensor ***#D*** (SR20-T1); (e) For sensor ***#E*** (MS-80); (f) For sensor ***#F*** (SPN1); (g) For sensor ***#G*** (SI02PT100)).



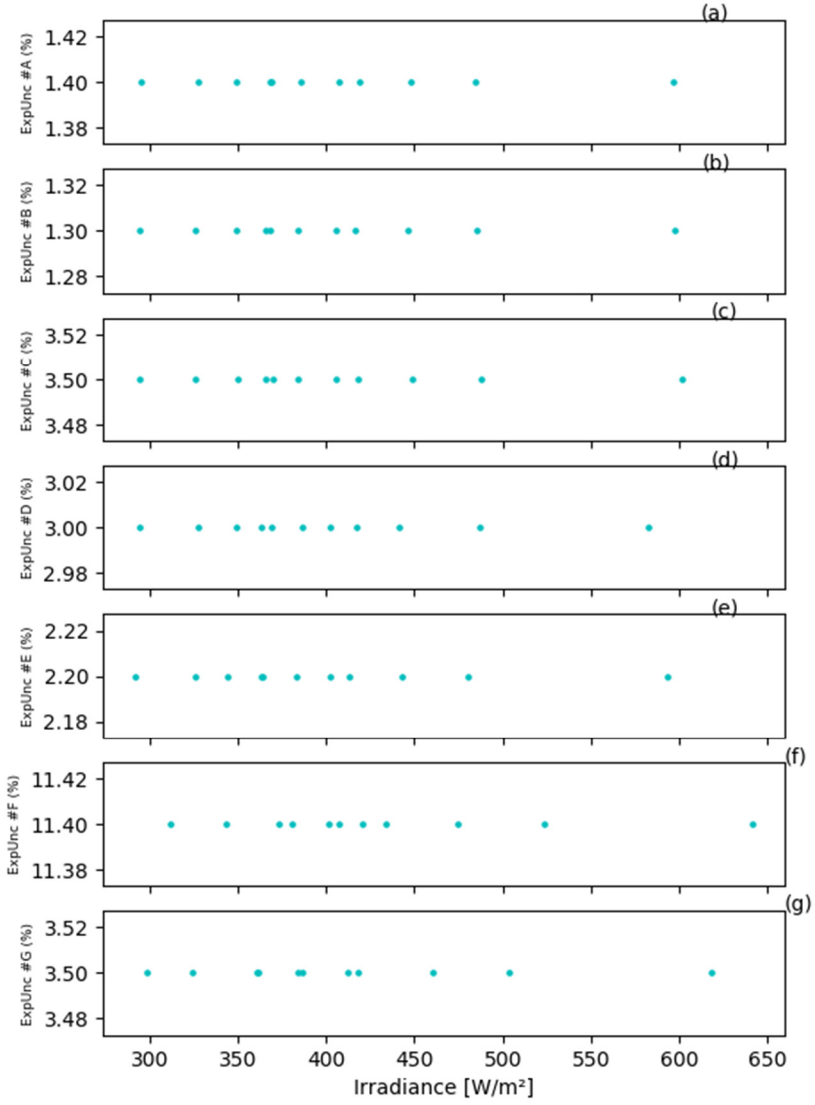
Source: elaborated by the author

Figure 8 – Expanded Uncertainty [%] in relation to Irradiance [W/m²] for one day average. ((a) For sensor ***#A*** (SMP22); (b) For sensor ***#B*** (SMP22); (c) For sensor ***#C*** (SMP11); (d) For sensor ***#D*** (SR20-T1); (e) For sensor ***#E*** (MS-80); (f) For sensor ***#F*** (SPN1); (g) For sensor ***#G*** (SI02PT100)).



Source: elaborated by the author

Figure 9 – Expanded Uncertainty [%] in relation to Irradiance [W/m²] for one month average. ((a) For sensor ***#A*** (SMP22); (b) For sensor ***#B*** (SMP22); (c) For sensor ***#C*** (SMP11); (d) For sensor ***#D*** (SR20-T1); (e) For sensor ***#E*** (MS-80); (f) For sensor ***#F*** (SPN1); (g) For sensor ***#G*** (SI02PT100)).



Source: elaborated by the author

As expected, as higher the average range is, the measurements tend towards a mean value. Therefore, the influence of absolute uncertainty is reduced and, consequently, the expanded uncertainty variability as well.

Moreover, an average of the calculated expanded uncertainty was taken for each temporal resolution dataset. The output values were identical for an all-time basis, considering only one decimal place. This situation is specially related to the fact that irradiance is a highly variable measurand; therefore, assuming that its standard deviation could not be taken into account, did not allow a reduction of its final uncertainty.

Finally, Table 7 shows the mean expanded uncertainty calculated. These values are considered to be stable for different irradiance situations, but should, however, be utilized carefully when analyzing very low irradiance measurements.

Table 7 - Calculated Mean Expanded Uncertainty (%), for radiometers ***#A*** (SMP22), ***#B*** (SMP22), ***#C*** (SMP11), ***#D*** (SR20-T1), ***#E*** (MS-80), ***#F*** (SPN1), ***#G*** (SI02PT100).

Sensor	Expanded Uncertainty [%]
#A	1,4%
#B	1,3%
#C	3,5%
#D	3,0%
#E	2,2%
#F	11,4%
#G	3,5%

Source: elaborated by the author

4.3 SENSOR EQUIVALENCE EVALUATION

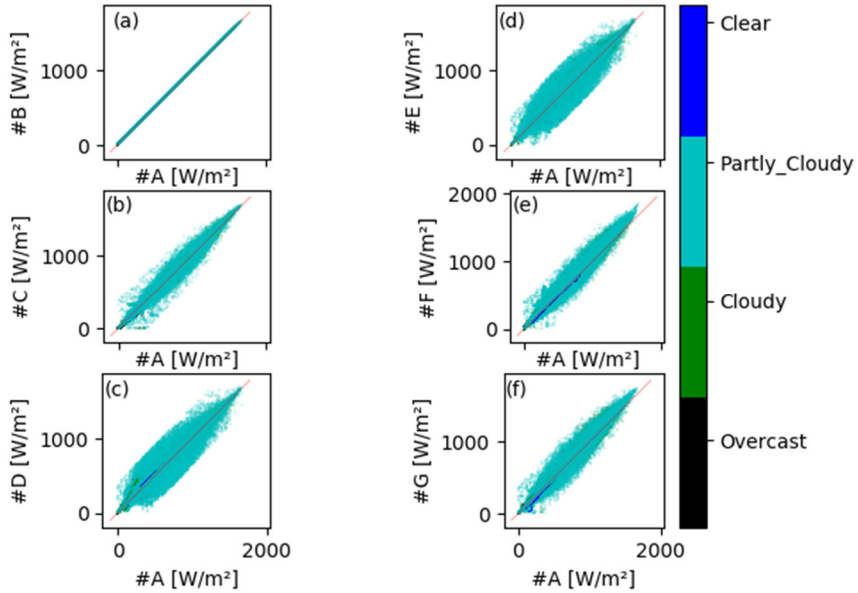
4.3.1 Scatterplot variation

In order to evaluate the radiometers' performance, it was carried out a comparison of each one to a reference, a statistical analysis was carried out. Initially, all sensors were plotted, in relation to sensor ***#A,*** to illustrate their behavior for different temporal resolutions.

Figure 10 demonstrates that sensor ***#B*** produces results practically equal to the reference, which is expected as both are the same pyranometer model, are physically nearby, and were calibrated by the same reference. Pyranometer ***#C*** showed small deviations from the reference as well. On the other hand, the Class A analog measured sensors (***#D*** and ***#E***) are illustrated with a higher magnitude of dispersion in relation to the reference line, in red.

In addition, it could be inferred by Figure 10(e), that ***#F*** could be generating overestimated irradiance data, as the data shifts upwards the reference line. For the reference cell (***#G***), higher deviations can be noticed for measurements over 1400 $[W/m^2]$, which is its trustable maximum measurement limit.

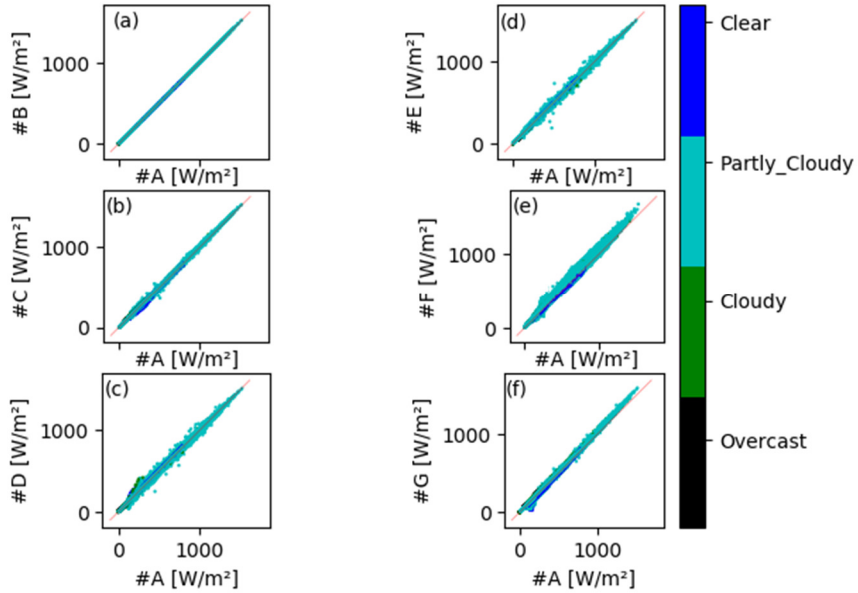
Figure 10 – Scatterplots of each sensor in relation to reference ***#A*** (SMP22), for one second time resolution, colored in relation to day type; (For: (a) ***#B*** (SMP22); (b) ***#C*** (SMP11); (c) ***#D*** (SR20-T1); (d) ***#E*** (MS-80); (e) ***#F*** (SPN1); (f) ***#G*** (SI02PT100)).



Source: elaborated by the author.

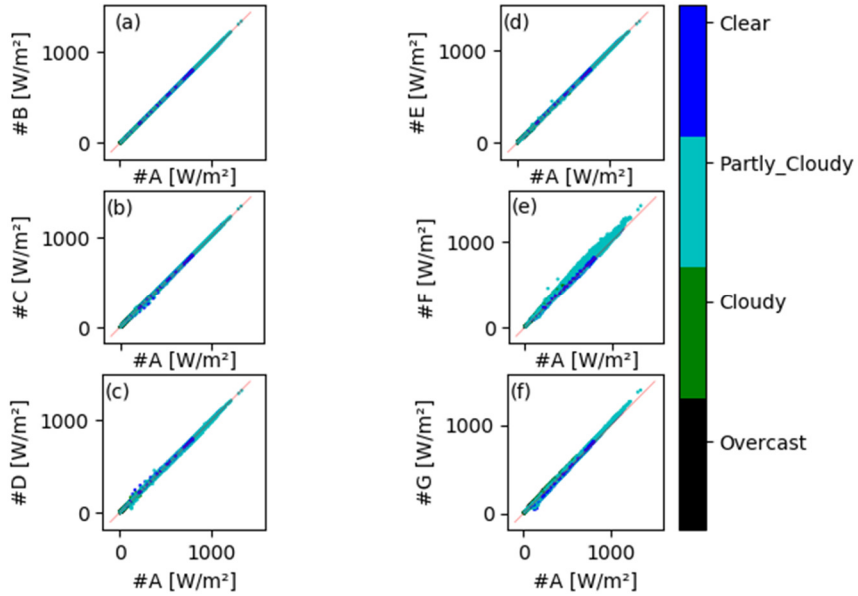
Furthermore, due to the amount of data, and the substantial majority of partly cloudy days, it is not possible to initially differentiate the behavior for each day type; even though clear days can be observed achieving practically a measurement equality.

Figure 11 - Scatterplots of each sensor in relation to reference #A (SMP22), for one minute average, colored in relation to day type; (For: (a) #B (SMP22); (b) #C (SMP11); (c) #D (SR20-T1); (d) #E (MS-80); (e) #F (SPN1); (f) #G (SI02PT100)).



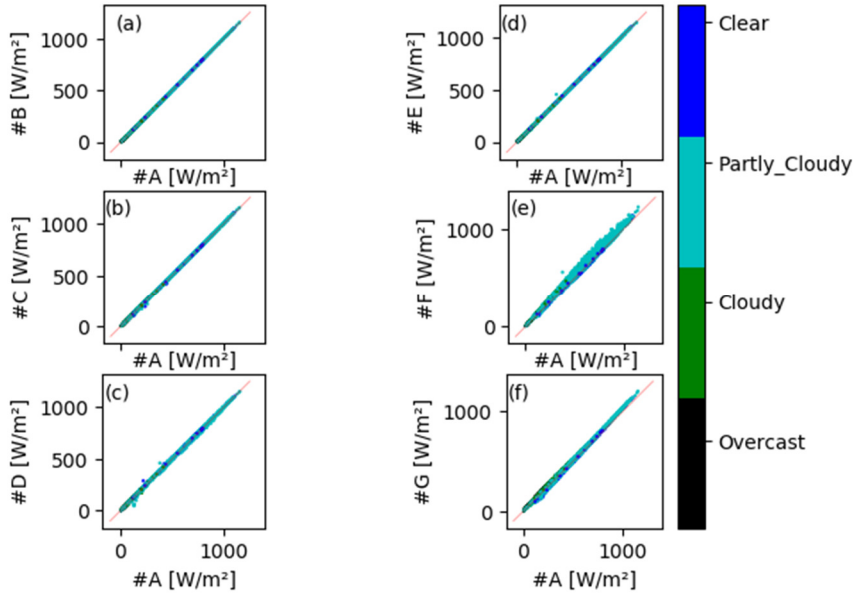
Source: elaborated by the author.

Figure 12 - Scatterplots of each sensor in relation to reference #A (SMP22), for fifteen minutes average, colored in relation to day type; (For: (a) #B (SMP22); (b) #C (SMP11); (c) #D (SR20-T1); (d) #E (MS-80); (e) #F (SPN1); (f) #G (SI02PT100)).



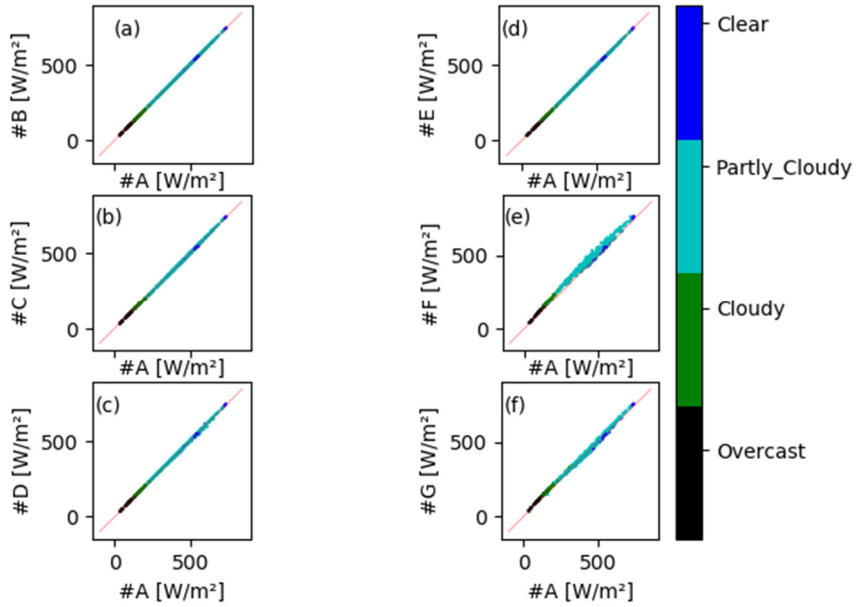
Source: elaborated by the author.

Figure 13 - Scatterplots of each sensor in relation to reference #A (SMP22), for one hour time resolution, colored in relation to day type; (For: (a) #B (SMP22); (b) #C (SMP11); (c) #D (SR20-T1); (d) #E (MS-80); (e) #F (SPN1); (f) #G (SI02PT100)).



Source: elaborated by the author.

Figure 14 - Scatterplots of each sensor in relation to reference #A (SMP22), for one day average, colored in relation to day type; (For: (a) #B (SMP22); (b) #C (SMP11); (c) #D (SR20-T1); (d) #E (MS-80); (e) #F (SPN1); (f) #G (SI02PT100)).

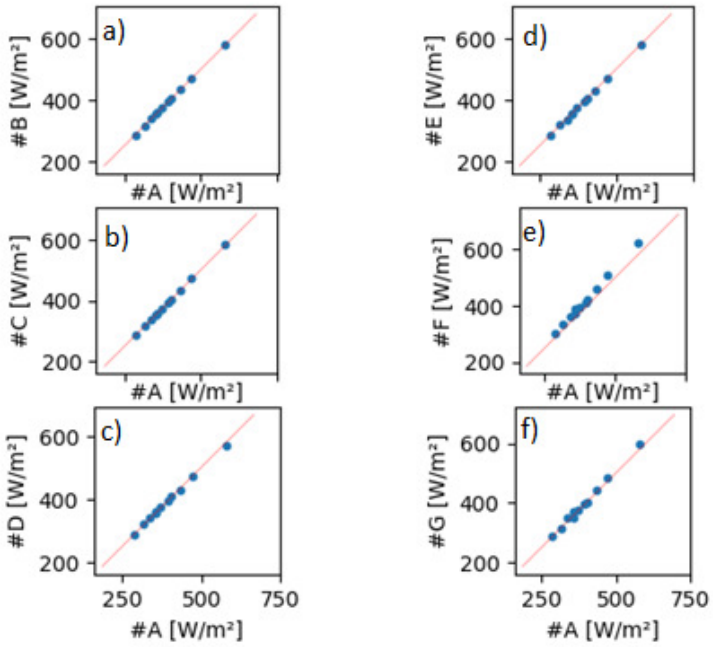


Source: elaborated by the author.

As average ranges increases, it is noticeable that sensors #C, #D, and #E tend to achieve analogous measurements in relation to the reference, regardless of the day type situation. On the other hand, #F demonstrates an overestimation pattern, which could be especially related to its high expanded uncertainty; moreover, this situation occurs mostly on partly cloudy, whilst clear and overcast ones perform normally, a fact that can be inferred clearly throughout Figure 14(e). #G shows slightly bigger variations, overestimating measurements over 1400[W/m²].

Moreover, Figure 15 illustrates the results for the monthly average. Thus, the recently discussed patterns are shown more smoothly.

Figure 15 - Scatterplots of each sensor in relation to reference #A (SMP22), for one month average; (For: (a) #B (SMP22); (b) #C (SMP11); (c) #D (SR20-T1); (d) #E (MS-80); (e) #F (SPN1); (f) #G (SI02PT100)).



Source: elaborated by the author.

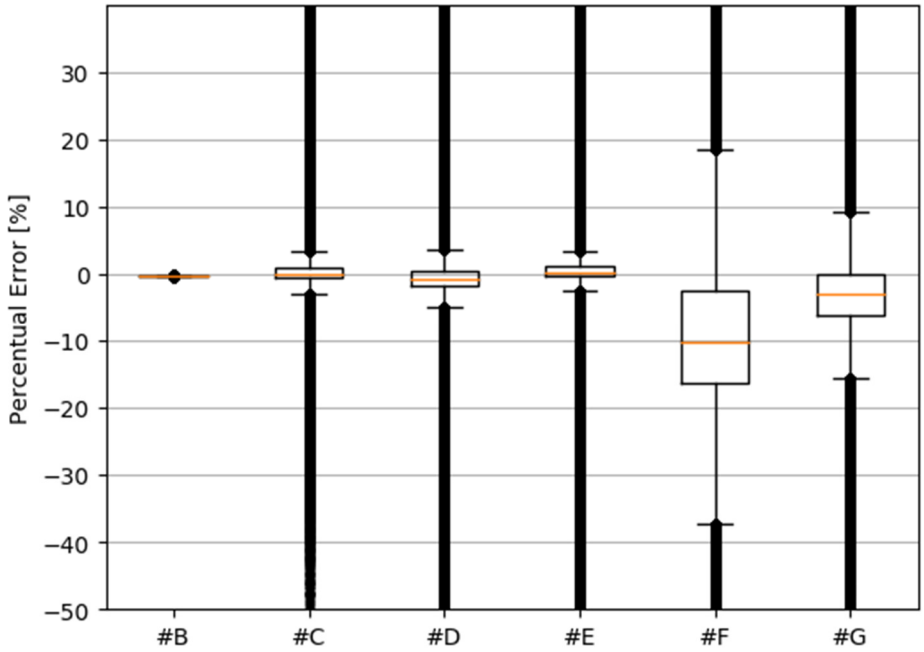
4.3.2 Percentual Error & Other Error Metrics

The percentual error (PE), described in section 2.2.1, was calculated for each evaluated sensor, in all six time resolutions. The figures below illustrate the boxplot of these calculations, where the black dots represents the outliers.

Outliers are defined here using the median and interquartile deviation method; thus, it is considered an outlier, a value outside of an interval of confidence of three times the sample's standard deviation. Previously, the results already showed high variability for high-frequency data acquisition; in addition, due to PE formulation, it tends to overestimate the error for small differences, causing outliers. Therefore, these extreme measurements will not be evaluated separately, as has occurred in previous research papers (Habte et al., 2016).

Figure 16 shows that ***#E*** has a small degree of underestimation, however, its boxplot is negatively skewed, thus its distribution pattern tends to zero. In addition, the MS-80 radiometer (***#E***) allegedly possesses a faster response time than the SMP22 radiometer (***#A***), according to both sensors datasheet. Thus, these observed variations may be in truth, a situation caused due to faster measurement response. Nonetheless, the fast response of each sensor will be evaluated in a further section.

Figure 16 - Percentual Error (PE) Boxplot graph for radiometers ***#B*** (SMP22), ***#C*** (SMP11), ***#D*** (SR20-T1), ***#E*** (MS-80), ***#F*** (SPN1), ***#G*** (SI02PT100). in relation to the reference (***#A*** (SMP22)), for one second time resolution.

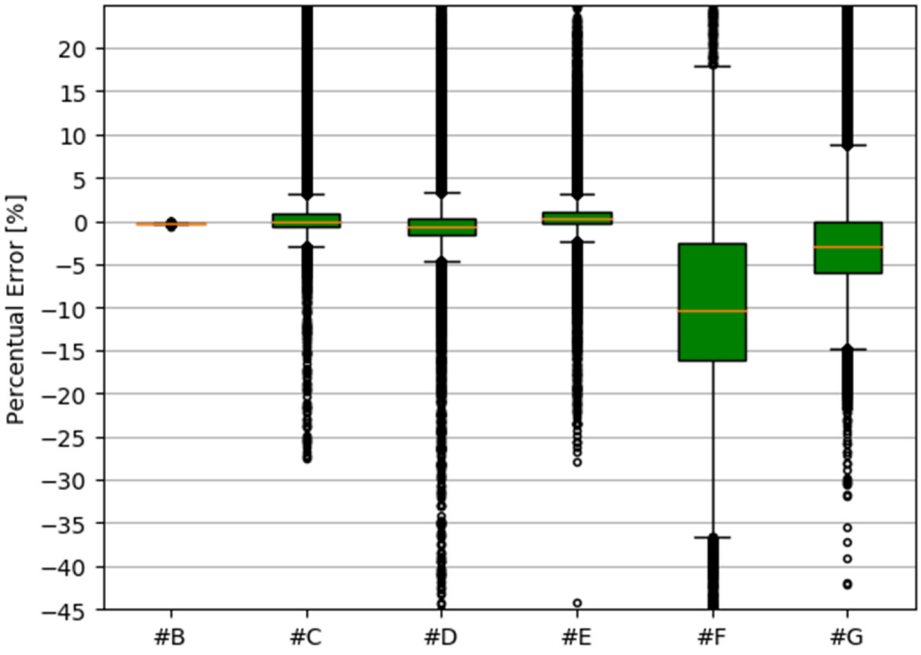


Source: elaborated by the author.

Moreover, PE of sensor ***#F*** has the broadest range for the dataset, which is intrinsically related to its high expanded uncertainty, thus causing measurements to be more disperse. In addition, the boxplot position in the graph already indicates an overestimation of irradiance values, since the PE average is negative. Furthermore, its interquartile is negatively skewed, showing that its distribution is shifted in the negative direction, demonstrating once more that is probable that embedded systematical errors are causing SPN1 (***#F***) to overestimate its measurements.

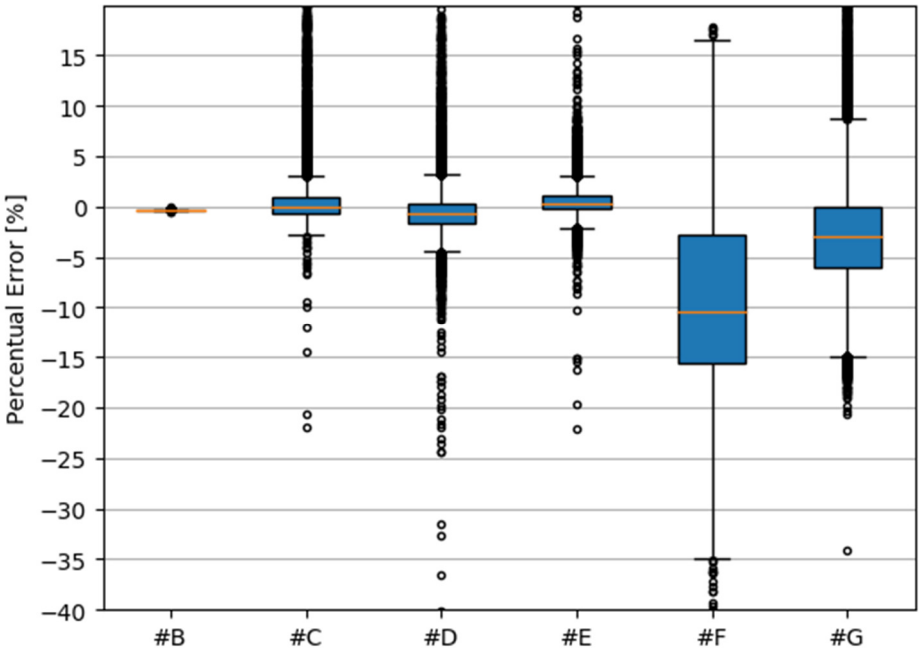
In the case of the photodiode radiometer (***#G***) the results show, as well as in the last case, that the sensor could have somehow a systematical error that is causing it to overestimate measurements; however, in a significantly smaller degree.

Figure 17 - Percentual Error (PE) Boxplot graph for radiometers ***#B*** (SMP22), ***#C*** (SMP11), ***#D*** (SR20-T1), ***#E*** (MS-80), ***#F*** (SPN1), ***#G*** (SI02PT100). in relation to the reference (***#A*** (SMP22)),for one minute average.



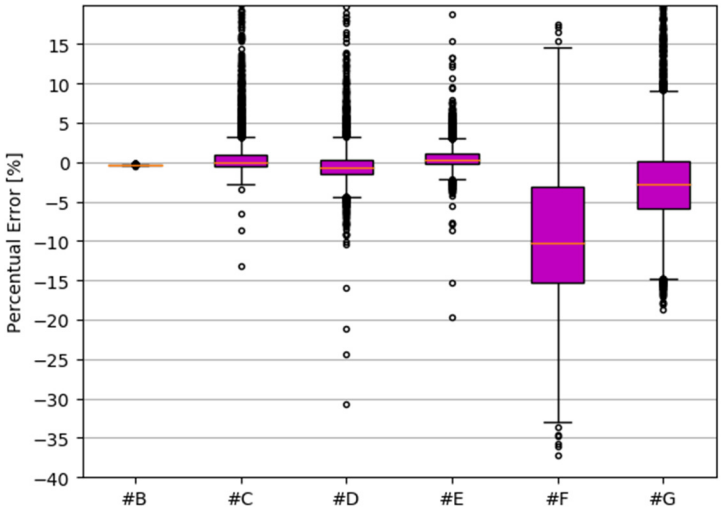
Source: elaborated by the author.

Figure 18 - Percentual Error (PE) Boxplot graph for radiometers ***#B*** (SMP22), ***#C*** (SMP11), ***#D*** (SR20-T1), ***#E*** (MS-80), ***#F*** (SPN1), ***#G*** (SI02PT100). in relation to the reference (***#A*** (SMP22)),for fifteen minutes time resolution.



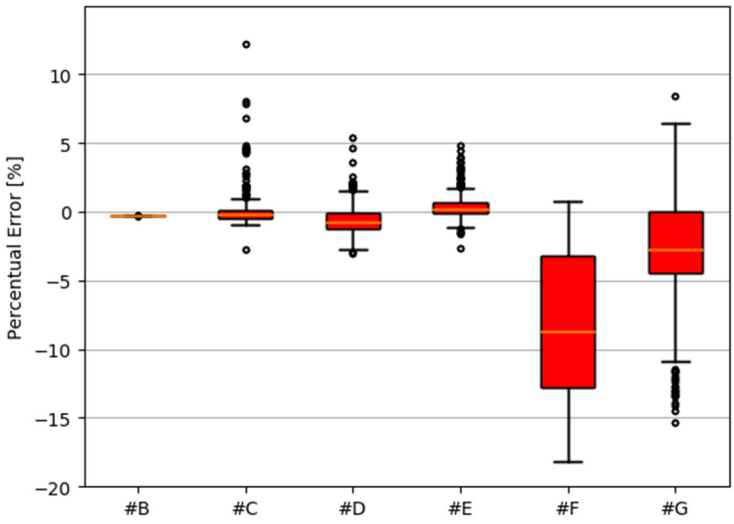
Source: elaborated by the author.

Figure 19 - Percentual Error (PE) Boxplot graph for radiometers ***#B*** (SMP22), ***#C*** (SMP11), ***#D*** (SR20-T1), ***#E*** (MS-80), ***#F*** (SPN1), ***#G*** (SI02PT100). in relation to the reference (***#A*** (SMP22)), for one-hour average.



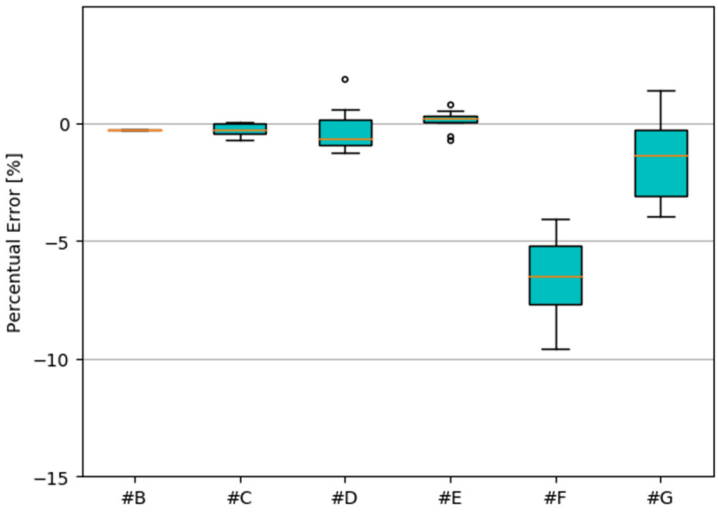
Source: elaborated by the author.

Figure 20 - Percentual Error (PE) Boxplot graph for radiometers ***#B*** (SMP22), ***#C*** (SMP11), ***#D*** (SR20-T1), ***#E*** (MS-80), ***#F*** (SPN1), ***#G*** (SI02PT100). in relation to the reference (***#A*** (SMP22)),for one-day average.



Source: elaborated by the author.

Figure 21 - Percentual Error (PE) Boxplot graph for radiometers ***#B*** (SMP22), ***#C*** (SMP11), ***#D*** (SR20-T1), ***#E*** (MS-80), ***#F*** (SPN1), ***#G*** (SI02PT100). in relation to the reference (***#A*** (SMP22)),for one-month average.



Source: elaborated by the author.

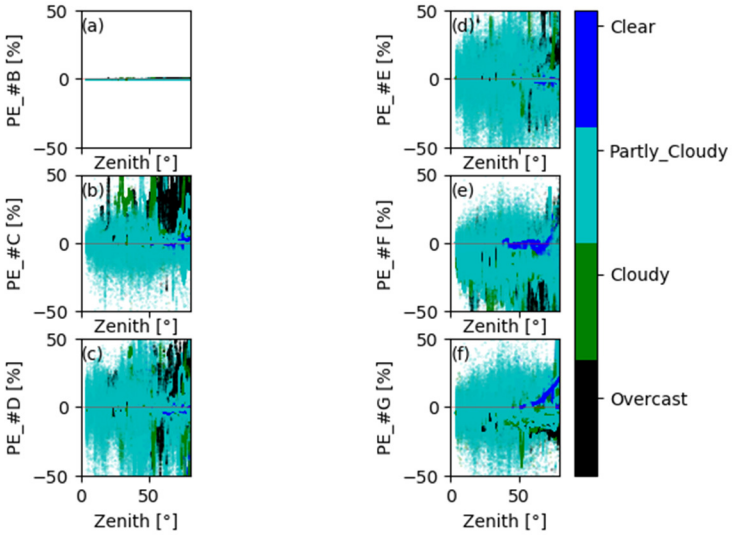
After the boxplots for all time resolutions were plotted, it was possible to have a general overview of the PE for different sensors.

As expected, as values are being averaged for higher interval means the outliers reduce drastically; moreover, higher temporal intervals tend to diminish major error deviations, such as illustrated by Figure 16 to Figure 21.

Class A sensors generated the best results for PE. ***#B*** performed better than the others, however as it is essentially the same sensor model as the reference, this is expected. Moreover, ***#C***, ***#D,*** and ***#E*** had some smaller deviations of results among them, however not significative. Besides, the small variation observed for ***#E*** will be assessed using further results. Sensor ***#F*** has demonstrated a significantly high percentual error, however approximate to its expanded uncertainty, of 11,4%, in most of the time resolutions. Finally, ***#G*** has demonstrated variations in PE, which could be related to its physical geometry, relating to poorer measurements near sunrise and sunset. Thus, a deeper analysis of PE in relation to the zenith angle will be done.

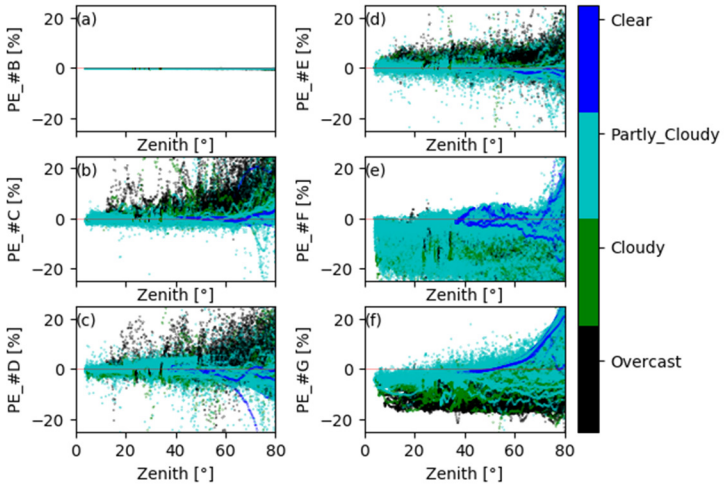
Therefore, in order to better characterize the sensors and their error origins and reasons, the percentual error was plotted in relation to the zenith angle. The figures for one-day and one-month time resolution will not be displayed, as it would not be reasonable to compare a zenith angle average for such a long period.

Figure 22 - Percentual Error (PE) in relation to Zenith Angle, for one second average, colored according to day type. (For: (a) ***#B*** (SMP22); (b) ***#C*** (SMP11); (c) ***#D*** (SR20-T1); (d) ***#E*** (MS-80); (e) ***#F*** (SPN1); (f) ***#G*** (SI02PT100)).



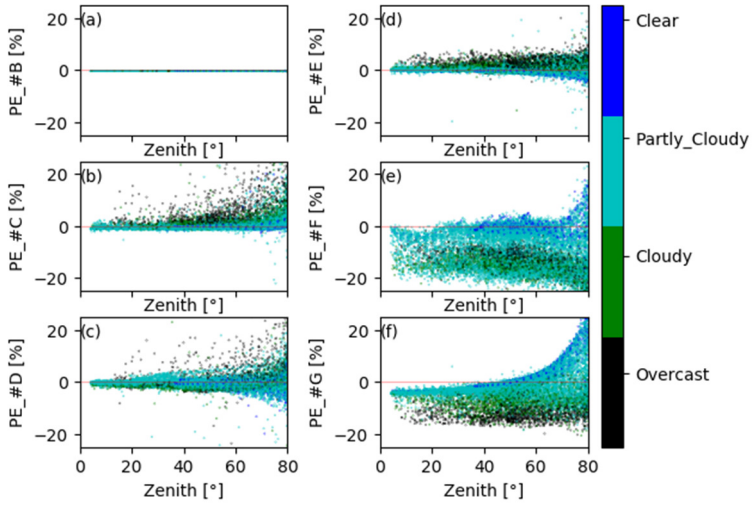
Source: elaborated by the author.

Figure 23 - Percentual Error (PE) in relation to Zenith Angle, for one-minute average, colored according to day type. (For: (a) ***#B*** (SMP22); (b) ***#C*** (SMP11); (c) ***#D*** (SR20-T1); (d) ***#E*** (MS-80); (e) ***#F*** (SPN1); (f) ***#G*** (SI02PT100)).



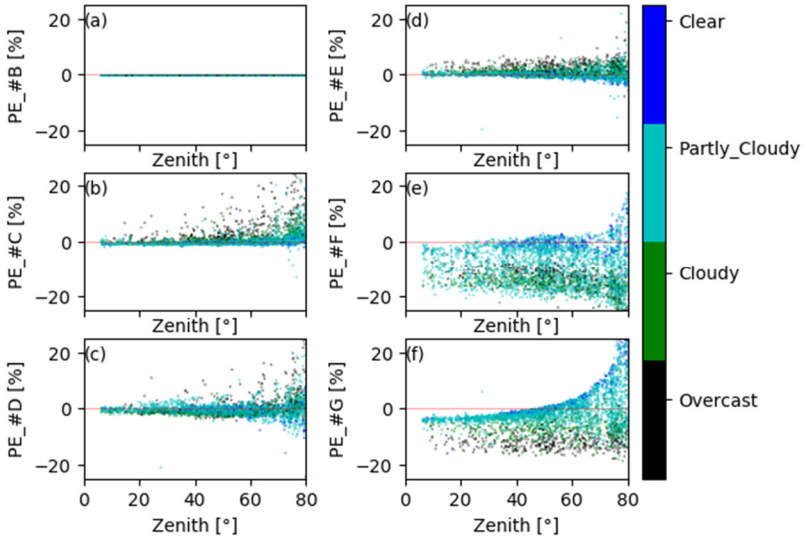
Source: elaborated by the author.

Figure 24 - Percentual Error (PE) in relation to Zenith Angle, for fifteen minutes average, colored according to day type. (For: (a) ***#B*** (SMP22); (b) ***#C*** (SMP11); (c) ***#D*** (SR20-T1); (d) ***#E*** (MS-80); (e) ***#F*** (SPN1); (f) ***#G*** (SI02PT100)).



Source: elaborated by the author.

Figure 25 - Percentual Error (PE) in relation to Zenith Angle, for one-hour average, colored according to day type. (For: (a) ***#B*** (SMP22); (b) ***#C*** (SMP11); (c) ***#D*** (SR20-T1); (d) ***#E*** (MS-80); (e) ***#F*** (SPN1); (f) ***#G*** (SI02PT100)).



Source: elaborated by the author.

The figures above allow some important interpretations regarding the PE variation for each sensor. Initially, the one-second time resolution does not permit a proper visualization, due to a high quantity of data points; however, it is already noticeable that high zenith angles and overcast days play an important role for high PE.

As the values are averaged, the trends and behavior of sensors become more clear. Apart from sensor ***#B***, Sensors ***#C***, ***#D,*** and ***#E*** present themselves as possessing the most linear

pattern in accordance with reference ***#A***. However, observing Figure 23(d) and Figure 24(d), it can be inferred that underestimated measurements, by ***#E***, occur mostly on cloudy and overcast days, reinforcing the idea that PE is overestimating low magnitude measurement errors.

Furthermore, ***#C*** is illustrated to have its error increasing proportionally to the zenith angle. Another important fact is that, as well for other cases, the cloudy and overcast days are responsible for most PE higher deviations.

For ***#D,*** a mirrored PE dispersion is noticed in all subplots. Presenting a higher deviation as zenith angles increases and, as for the other sensors, higher PE when in cloudy and overcast day situations.

In the case of ***#F***, the available results demonstrate that the systematic variation of the previously shown boxplots is being generated by a majority of cloudy and overcast days as well. The former day type is related to several irradiance ramps, thus the response time could be an important factor affecting the sensor performance. On the other hand, the latter has normally low irradiance measurements, due to sky condition; thus, adding to sensor ***#F***'s high uncertainties and PE overestimations for small magnitude values, this should explain the high deviations in overcast days. However, despite these day types were to be excluded, SPN1 still has highly variable measurements and would not perform as well as its pairs.

Sensor ***#G*** presents the same situation for cloudy and overcast days as previously explained, as it is clearly illustrated in Figure 24(f). Moreover, it has shown a unique pattern for clear days, increasing its PE significantly according to the zenith angle; thus, it could be explained due to the difference in spectral range, and a possible solar spectrum variation in sunrise and sunset. However, this supposition would require further studies and experiments to be affirmed. Moreover, another explanation would be its physical geometry, as a flat glass have more issues when assessing higher zenith angles.

In order to have a better general view of the dataset errors, different error metrics were used to characterize each sensor in relation to the reference. These values are displayed in the tables below.

Table 8 - Calculated Error metrics for complete dataset, for one-second time resolution, for radiometers ***#B*** (SMP22), ***#C*** (SMP11), ***#D*** (SR20-T1), ***#E*** (MS-80), ***#F*** (SPN1), ***#G*** (SI02PT100).

Time Resolution: 1 Second							
Sensor	R² [%]	RMSE [W/m²]	nRMSE [%]	MAE [W/m²]	nMAE [%]	MBE [W/m²]	nMBE [%]
#B	100,00%	1,43	0,36%	1,15	0,29%	-1,15	-0,29%
#C	99,94%	7,34	1,85%	3,55	0,89%	-0,94	-0,24%
#D	99,81%	12,41	3,13%	5,72	1,44%	-1,95	-0,49%
#E	99,85%	11,35	2,86%	3,94	0,99%	0,92	0,23%
#F	98,16%	39,08	9,86%	28,57	7,21%	-26,60	-6,71%
#G	99,54%	19,62	4,95%	14,34	3,62%	-7,91	-2,00%

Source: elaborated by the author.

Table 9 - Calculated Error metrics for complete dataset, for one-minute time resolution, for radiometers ***#B*** (SMP22), ***#C*** (SMP11), ***#D*** (SR20-T1), ***#E*** (MS-80), ***#F*** (SPN1), ***#G*** (SI02PT100).

Average: 1 Minute							
Sensor	R² [%]	RMSE [W/m²]	nRMSE [%]	MAE [W/m²]	nMAE [%]	MBE [W/m²]	nMBE [%]
#B	100,00%	1,42	0,36%	1,15	0,29%	-1,15	-0,29%
#C	99,97%	4,61	1,16%	3,00	0,76%	-0,94	-0,24%
#D	99,93%	7,55	1,91%	4,91	1,24%	-1,95	-0,49%
#E	99,97%	4,74	1,20%	2,87	0,73%	0,91	0,23%
#F	98,21%	38,30	9,67%	28,27	7,14%	-26,58	-6,71%
#G	99,61%	17,79	4,49%	13,76	3,47%	-7,91	-2,00%

Source: elaborated by the author.

Table 10 - Calculated Error metrics for complete dataset, for fifteen minutes time resolution, for radiometers ***#B*** (SMP22), ***#C*** (SMP11), ***#D*** (SR20-T1), ***#E*** (MS-80), ***#F*** (SPN1), ***#G*** (SI02PT100).

Average: 15 Minutes							
Sensor	R² [%]	RMSE [W/m²]	nRMSE [%]	MAE [W/m²]	nMAE [%]	MBE [W/m²]	nMBE [%]
#B	100,00%	1,39	0,36%	1,13	0,29%	-1,13	-0,29%
#C	99,98%	4,02	1,03%	2,76	0,71%	-0,86	-0,22%
#D	99,94%	6,68	1,72%	4,55	1,17%	-1,89	-0,49%
#E	99,99%	3,30	0,85%	2,42	0,62%	0,89	0,23%
#F	98,24%	37,09	9,55%	27,57	7,09%	-26,08	-6,71%
#G	99,61%	17,33	4,46%	13,55	3,49%	-7,51	-1,93%

Source: elaborated by the author.

Table 11 - Calculated Error metrics for complete dataset, for one-hour time resolution, for radiometers ***#B*** (SMP22), ***#C*** (SMP11), ***#D*** (SR20-T1), ***#E*** (MS-80), ***#F*** (SPN1), ***#G*** (SI02PT100).

Average: 1 Hour							
Sensor	R^2 [%]	RMSE [W/m²]	nRMSE [%]	MAE [W/m²]	nMAE [%]	MBE [W/m²]	nMBE [%]
#B	100,00%	1,34	0,36%	1,08	0,29%	-1,08	-0,29%
#C	99,98%	3,71	1,00%	2,60	0,70%	-0,70	-0,19%
#D	99,94%	6,81	1,84%	4,40	1,19%	-1,74	-0,47%
#E	99,99%	3,24	0,87%	2,29	0,62%	0,80	0,22%
#F	98,34%	34,98	9,44%	26,15	7,06%	-24,92	-6,72%
#G	99,62%	16,79	4,53%	13,19	3,56%	-6,58	-1,77%

Source: elaborated by the author.

Table 12 - Calculated Error metrics for complete dataset, for one-day time resolution, for radiometers ***#B*** (SMP22), ***#C*** (SMP11), ***#D*** (SR20-T1), ***#E*** (MS-80), ***#F*** (SPN1), ***#G*** (SI02PT100).

Average: 1 Day							
Sensor	R^2 [%]	RMSE [W/m²]	nRMSE [%]	MAE [W/m²]	nMAE [%]	MBE [W/m²]	nMBE [%]
#B	99,99%	1,23	0,32%	1,13	0,29%	-1,13	-0,29%
#C	99,98%	2,25	0,58%	1,74	0,45%	-0,84	-0,22%
#D	99,94%	4,20	1,08%	3,38	0,87%	-1,89	-0,49%
#E	99,98%	2,29	0,59%	1,79	0,46%	0,77	0,20%
#F	96,77%	30,36	7,82%	25,78	6,64%	-25,63	-6,60%
#G	99,52%	11,75	3,03%	10,31	2,66%	-7,00	-1,80%

Source: elaborated by the author.

Table 13 - Calculated Error metrics for complete dataset, for one-month time resolution, for radiometers ***#B*** (SMP22), ***#C*** (SMP11), ***#D*** (SR20-T1), ***#E*** (MS-80), ***#F*** (SPN1), ***#G*** (SI02PT100).

Average: 1 Month							
Sensor	R^2 [%]	RMSE [W/m²]	nRMSE [%]	MAE [W/m²]	nMAE [%]	MBE [W/m²]	nMBE [%]
#B	99,98%	1,16	0,39%	1,14	0,29%	-1,14	-0,29%
#C	99,95%	1,71	0,58%	1,20	0,31%	-1,11	-0,28%
#D	99,68%	4,34	1,31%	3,38	0,86%	-0,68	-0,17%
#E	99,96%	1,53	1,10%	1,29	0,33%	0,54	0,14%

#F	87,22%	27,63	6,43%	25,93	6,64%	-25,93	-6,64%
#G	98,35%	9,93	2,83%	7,96	2,04%	-6,61	-1,69%

Source: elaborated by the author.

Furthermore, the error metrics displayed in the tables above are in accordance with what was already discussed in this section. R^2 accuracy were all above 99%, in exception for SPN1 (***#F***) independently of its time resolution and for ***#G*** in Table 13.

Another important aspect is that ***#B*** and ***#E*** have had the most accurate nRMSE and nMAE results; in addition, ***#E*** has the only positive nMBE, which can be clearly illustrated by Figure 24(d), demonstrating a different pattern from its pairs.

#C and ***#D*** performed as expected, achieving similar error results in relation to ***#B*** and ***#E***. In addition, the nMBE for ***#D*** was found out to be twice as higher as for these other three pyranometers; however, its highest dispersion, displayed in Figure 24(c), would explain this result.

The results for ***#F*** confirm the fact that it generates highly variable measurements, which can be inferred by the higher nRMSE in relation to nMAE for high-frequency data acquisition, as nRMSE is firstly elevated to the power of two, it inputs more weight in larger differences; however, as the values are averaged, this two metrics tend to equalize themselves. Furthermore, a negative and high nMBE also confirmed the overestimation of SPN1 (***#F***) measurements.

#G has presented an nRMSE = 4,95% and nMAE = 3,62% for one second time resolution. These values are in accordance with expectation, due to previous analyses; in addition, an nMBE varying around -1,8% was a reasonable result. Even though #G has a relatively small expanded uncertainty, these poorer results are probably related to the fact that it is a silicon photodiode, and has different properties from thermopile pyranometers.

4.3.3Hypothesis Test

The paired ratio hypothesis test, described in section 3.3.2, was used in order to evaluate the null hypothesis. Moreover, as the test is based on a ratio, its result would not be altered by a different time resolution, which is the average of the former time resolution. Therefore, only the one second time resolution results will be displayed.

From section 3.3.2 we have that:

H_0: "*The sensor does NOT present equivalent measurement data in relation to the reference*".

H_1: "*The sensor presents equivalent measurement data in relation to the reference"*.

In addition, this is a two-sided hypothesis which is limited by the expanded uncertainty of reference ***#A***. Thus, resulting from section 4.2 a value of 1,4%. Therefore, the upper limit is 1,014, and the lower limit 0,986, which will be analyzed for a 95% interval of confidence.

Then, mathematically we would have that:

$$H_0 : \text{Ratio} \leq 0{,}986 \text{ and Ratio} \geq 1{,}014$$

$$H_1 : 0{,}986 < \text{Ratio} < 1{,}014$$

Thus, the results are displayed in the table below.

Table 14 – Paired ratio hypothesis test results, for radiometers ***#B*** (SMP22), ***#C*** (SMP11), ***#D*** (SR20-T1), ***#E*** (MS-80), ***#F*** (SPN1), ***#G*** (SI02PT100) in relation to the reference (***#A*** (SMP22)).

Sensor	Null Hypothesis	T - Value	P-Value	Neglect Null Hypothesis
#B	Ratio ≤ 0,986	4716,1	≅ 0	Yes
	Ratio ≥ 1,014	-4715,7	≅ 0	
#C	Ratio ≤ 0,986	2331,7	≅ 0	Yes
	Ratio ≥ 1,014	-2294,4	≅ 0	
#D	Ratio ≤ 0,986	2018,6	≅ 0	Yes
	Ratio ≥ 1,014	-944,74	≅ 0	
#E	Ratio ≤ 0,986	1326,0	≅ 0	Yes
	Ratio ≥ 1,014	-1843,2	≅ 0	
#F	Ratio ≤ 0,986	3709,7	≅ 0	No
	Ratio ≥ 1,014	2573,3	≅ 1	
#G	Ratio ≤ 0,986	2298,1	≅ 0	No
	Ratio ≥ 1,014	489,98	≅ 1	

Source: elaborated by the author.

Table 14 shows the results for the hypothesis test, which concluded that sensors ***#B***, ***#C***, ***#D,*** and ***#E*** can claim equivalence to sensor ***#A***. However, sensors ***#F*** and ***#G*** cannot. These test results are a conclusion of what has been discussed in the previous sections. Since the noticeable measurement overestimation of ***#F*** neglected the alternative hypothesis in its upper

limit. Moreover, this situation was analogous for ***#G***, however, in a smaller magnitude, thus if the reference sensor was not so accurate, with an expanded uncertainty of 1,4%, the reference cell would probably neglect H_0. For instance, if the objective would be to compare with sensor ***#C***, with a 3,5% expanded uncertainty, ***#G*** would be able to claim equivalence, whilst ***#F*** still could not.

4.3.4 Results Overview

Due to information discussed in this section, we can conclude that sensors ***#B***, ***#C***, ***#D,*** and ***#E*** can claim equivalency of measurement in relation to reference ***#A***. For these four radiometers, the nRMSE achieved values up to 1,91% for all-sky conditions, which is in accordance with recent studies published in the literature (Habte et al., 2016). Furthermore, the error metrics were not separated for each day type for individual analysis, as the aim of this study is to evaluate equivalency regarding all-sky conditions. However, graphical illustrations demonstrated that the biggest deviations are related to cloudy and overcast day types; in addition, to high zenith angles. Furthermore, a more stratified analysis, analyzing the data error metrics for specific zenith angle ranges and day types, separately, are left for future works.

Sensor ***#F*** presented the poorest results among all equipment. Resulting in a nRMSE up to 9,86% and a nMBE of -6,72%, demonstrating an unprecise measurement pattern and systematically biased deviations. As well as for the other sensors, its poorest PE results were related to cloudy and overcast sky conditions. In addition, the literature proposes several calibration approaches that would reduce SPN1 (***#F***)'s uncertainty (Badosa et al., 2014; Möllenkamp et al., 2020). Thus, it would be plausible that these procedures would cause ***#F*** to perform better and, perhaps, be able to claim equivalence. However, these procedures were not implemented or evaluated in this work, and are left for future work.

The reference cell (***#G)*** was not able to claim equivalency either. Recent studies results showed that, for a desert environment, annual differences between a photodiode and a pyranometer could achieve up to 1,5% for GHI (Al-Rasheedi et al., 2018). In addition, another study carried in Morocco reported that, for global plan of array (GPOA), monthly deviations can be up to -4,8% for high temperature periods (Azouzoute et al., 2019). Therefore, in Florianópolis, Brazil, a city with a warm humid subtropical climate (Alvares et al., 2013; Peel et al., 2007), with a majority of partly cloudy days, it is expected that annual deviations will be bigger than 1,5%, as it was shown by the Tables in section 4.3.2. Thus, comparing to a reference

with an expanded uncertainty of 1,4% would not be plausible that their measurements would be equivalent. However, whilst comparing with sensor ***#C***, which possesses a much higher uncertainty concerning ***#A***, the hypothesis test outputted a positive result for the photodiode.

4.4 Overirradiance behavior evaluation

This section aims to evaluate the behavior of each sensor in relation to overirradiance. The events will be separated into two sections: an overirradiance (OIR) dataset containing all events and an extreme overirradiance (EOIR) dataset, filtered for irradiance values above the defined G_0.

The data will be analyzed quantitatively and qualitatively, thus, the number of events, and its duration, will be accounted for and separated in time intervals, in order to demonstrate the capabilities of each sensor to identify such events. Furthermore, the time response will be evaluated by the second derivative and its ratio in relation to reference ***#G***.

4.4.1 Preliminary processing

The dataset corrected offset and the extraterrestrial horizontal irradiance (ETH) were used to calculate the kt_0.

Furthermore, a python script was made in order to identify all events in the dataset. For instance, as it was defined in section 3.4.3, an overirradiance event begins at the first available measurement before $kt_0 > 1$ and ends at the subsequent value of $kt_0 < 1$.

4.4.2 Evaluation of overirradiance and extreme overirradiance events

In this section, the quantitative results of overirradiance measurements are going to be assessed. Initially, in order to observe how the radiometers are performing in relation to each other in extreme events, each maximum irradiance measurement and its respective clearness index were extracted from the dataset. Table 15 displayed these measurements.

Table 15 - Maximum irradiance measurement occurred in the dataset, for radiometers ***#A*** (SMP22), ***#B*** (SMP22), ***#C*** (SMP11), ***#D*** (SR20-T1), ***#E*** (MS-80), ***#F*** (SPN1), ***#G*** (SI02PT100), and its respective clearness index (kt_0).

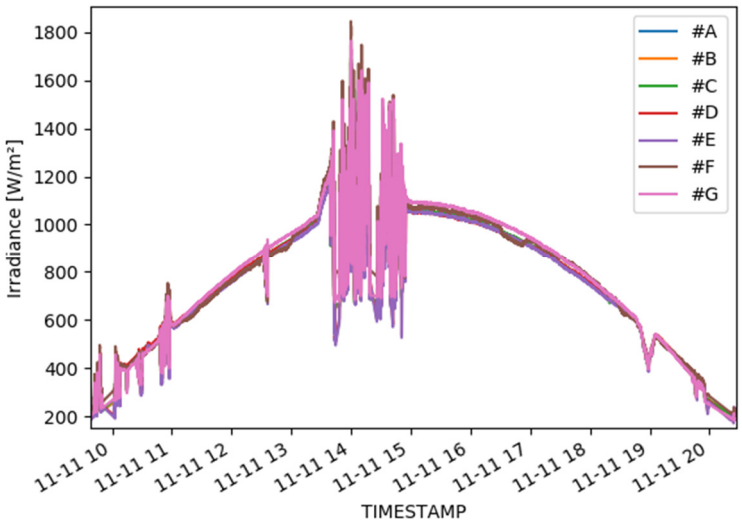
Sensor	*Maximum Irradiance [W/m²]*	*kt0*
#A	1673,0	1,25
#B	1677,9	1,26
#C	1692,1	1,27
#D	1672,7	1,25
#E	1672,9	1,25
#F	1845,5	1,38
#G	1764,5	1,32

Source: elaborated by the author.

For instance, Class A pyranometers have acquired similar maximum values, with smaller variation in their kt_0. Which by themselves already represent important information, as such high magnitude irradiance measurements at low altitude have started only to be reported from a few years (do Nascimento et al., 2019; Yordanov et al., 2015).

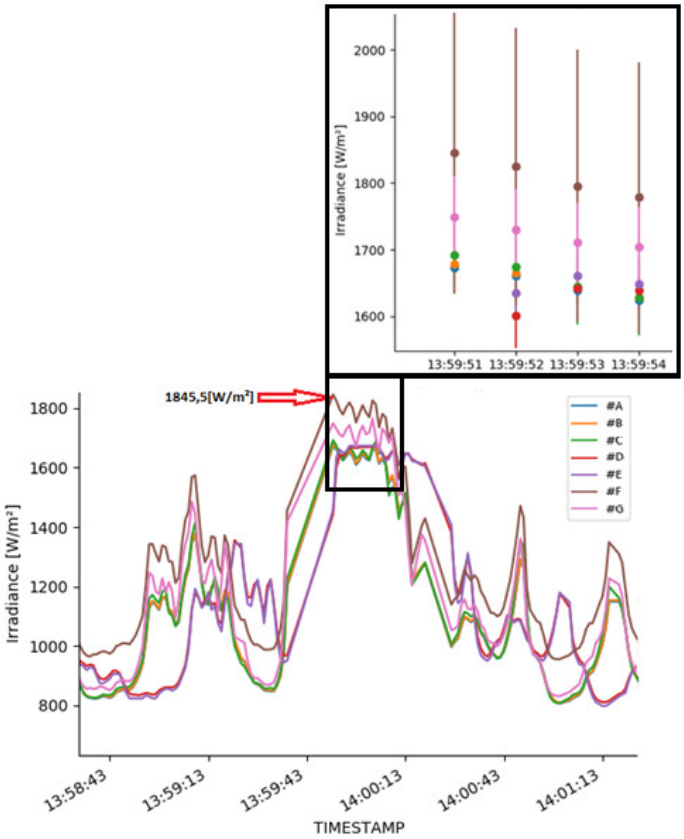
Even though $1764,5_{[W/m^2]}$ goes far beyond the trusted limit measurement for the photodiode ***#G***, this value should not be discarded as this sensor possess the fastest time response among all evaluated equipment. Although sensor #F recorded one of the highest irradiance measurements recorded in the literature (do Nascimento et al., 2019), it should be confirmed later in this work, due to its high expanded uncertainty. As illustrated from Figure 25 and Figure 27, its value surpasses through the ranges of all radiometers on-site, arising more doubts in relation to this measurement veracity. However, this situation will be further analyzed after the response time assessment has been discussed.

Figure 26 - Daily data for the highest irradiance measurement (2018-11-11), for radiometers ***#A*** (SMP22), ***#B*** (SMP22), ***#C*** (SMP11), ***#D*** (SR20-T1), ***#E*** (MS-80), ***#F*** (SPN1), ***#G*** (SI02PT100).



Source: elaborated by the author.

Figure 27 - Approximate data for the highest irradiance measurement (2018-11-11) and its respective error bars, for radiometers ***#A*** (SMP22), ***#B*** (SMP22), ***#C*** (SMP11), ***#D*** (SR20-T1), ***#E*** (MS-80), ***#F*** (SPN1), ***#G*** (SI02PT100).



Source: elaborated by the author.

4.4.2.1 Overirradiance (OIR) Events

In this subsection, overirradiance events and their number of occurrences are displayed and discussed.

Table 16 – Assessment of OIR events, their duration in minutes and total accumulated in hours of data observation period, for radiometers ***#A*** (SMP22), ***#B*** (SMP22), ***#C*** (SMP11), ***#D*** (SR20-T1), ***#E*** (MS-80), ***#F*** (SPN1), ***#G*** (SI02PT100).

Overrirradiance Events			
Sensor	*Number of Events*	*Longest Event [min]*	*Total Events Time [h]*
#A	1582	4,7	6,1
#B	1623	5,0	6,5
#C	2057	4,7	7,5
#D	1677	5,0	6,4
#E	1887	5,0	6,2
#F	4393	12,4	16,9
#G	3112	6,9	11,5

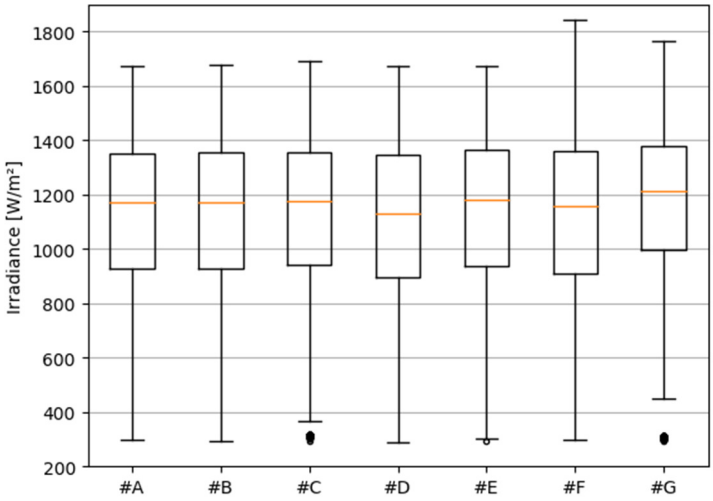
Source: elaborated by the author.

Table 17 – Assessment of OIR events for specific time intervals, for radiometers ***#A*** (SMP22), ***#B*** (SMP22), ***#C*** (SMP11), ***#D*** (SR20-T1), ***#E*** (MS-80), ***#F*** (SPN1), ***#G*** (SI02PT100).

Overrirradiance Events						
Sensor	$x \leq 1s$	$1s < x \leq 5s$	$5s < x \leq 30s$	$30s < x \leq 60s$	$60s < x \leq 300s$	$x > 300s$
#A	166	567	680	104	65	0
#B	147	580	716	105	74	1
#C	271	756	823	122	85	0
#D	167	617	723	108	61	1
#E	271	715	736	106	58	1
#F	678	1572	1708	258	169	8
#G	447	1124	1244	174	121	2

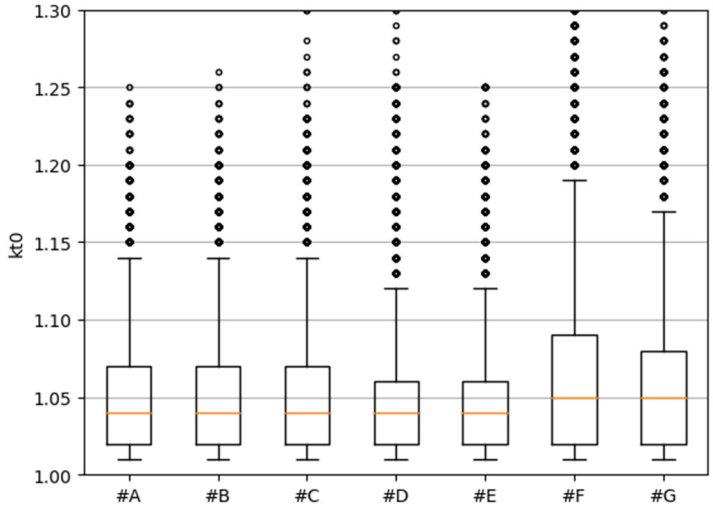
Source: elaborated by the author.

Figure 28 – Boxplot for measured irradiance during overirradiance events, for radiometers ***#A*** (SMP22), ***#B*** (SMP22), ***#C*** (SMP11), ***#D*** (SR20-T1), ***#E*** (MS-80), ***#F*** (SPN1), ***#G*** (SI02PT100).



Source: elaborated by the author.

Figure 29 – Boxplot for calculated kt_0 from measured irradiance during overirradiance events, for radiometers ***#A*** (SMP22), ***#B*** (SMP22), ***#C*** (SMP11), ***#D*** (SR20-T1), ***#E*** (MS-80), ***#F*** (SPN1), ***#G*** (SI02PT100).



Source: elaborated by the author.

From the results shown in the tables and figures above, sensor ***#F*** can initially be seen as the most representative whilst observing OIR events, accounting for even more events than the reference photodiode. However, previous analyses of its expanded uncertainty and its measurement pattern have demonstrated that this high rate of events identification is due to its uncertainty magnitude. Therefore, we cannot account for this specific analysis that ***#F*** has trustable results in relation to the other sensors, due to their significantly better uncertainty.

Sensor ***#C*** has identified over 65% of events that reference ***#G*** has measured. Thus, at a first analysis, performing better than more precise sensors. However, Figure 28 illustrates that overirradiance events can vary from less than $400_{[W/m^2]}$ until almost $1900_{[W/m^2]}$; thus the ***#C***'s better performance can be related to the same factor as the one mentioned for SPN1 (***#F***), its 3,5% expanded uncertainty could be generating false data above the clearness index. However, sensor ***#C*** uncertainty has a small magnitude, thus it would not be reasonable to consider this assumption, and neglect SMP11 (***#C***) performance in identifying such events.

In addition, sensors ***#A***, ***#B***, ***#D*** have achieved similar performances, identifying around 50% to 54% of the events identified by the reference cell (***#G***). Among these three, sensor ***#D*** has had the best performance; however, its higher uncertainty, twice the time of ***#A*** or ***#B***, could be corroborating to its performance, as it was already supposed for ***#C*** as well.

Furthermore, sensor ***#E*** has demonstrated itself highly capable of identifying events, especially at small frequencies (Time resolution ≤ 5s), thus producing the second best result among the evaluated pyranometers.

4.4.2.2 Extreme Overirradiance (EOIR) Events

In this subsection, the dataset was filtered to correspond only to extreme events, thus related to high irradiance measurements. The results are presented analogously to the previous section, in order to provide better visualization and allow a comparison between them.

Table 18 - Assessment of EOIR events, their duration in minutes and total accumulated in hours of data observation period,, for radiometers ***#A*** (SMP22), ***#B*** (SMP22), ***#C*** (SMP11), ***#D*** (SR20-T1), ***#E*** (MS-80), ***#F*** (SPN1), ***#G*** (SI02PT100).

Extreme Overirradiance Events			
Sensor	*Number of Events*	*Longest Event [min]*	*Total Events Time [h]*
#A	475	3,3	1,4
#B	477	3,3	1,5
#C	505	3,3	1,5
#D	477	3,3	1,4
#E	495	3,3	1,4
#F	517	3,3	1,7
#G	518	3,3	1,7

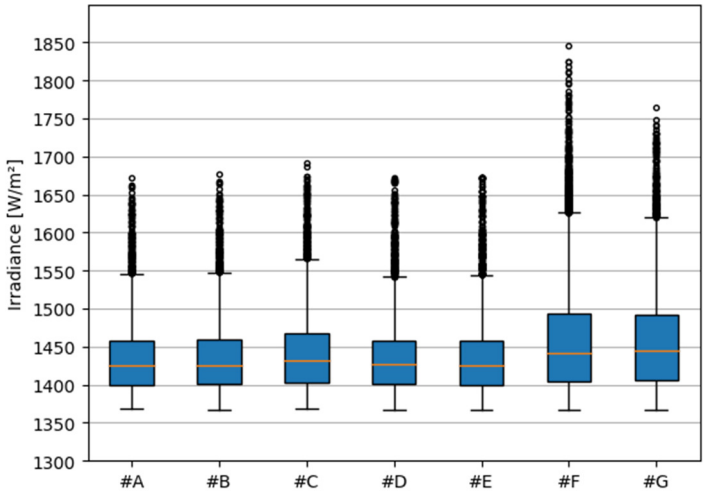
Source: elaborated by the author.

Table 19 - Assessment of EOIR events for specific time intervals, for radiometers ***#A*** (SMP22), ***#B*** (SMP22), ***#C*** (SMP11), ***#D*** (SR20-T1), ***#E*** (MS-80), ***#F*** (SPN1), ***#G*** (SI02PT100).

Extreme Overirradiance Events					
Sensor	$x \leq 1s$	$1s < x \leq 5s$	$5s < x \leq 30s$	$30s < x \leq 60s$	$x > 60s$
#A	57	185	190	34	9
#B	51	192	189	33	12
#C	60	198	200	35	12
#D	66	179	195	30	7
#E	72	184	202	30	7
#F	51	204	211	36	15
#G	55	201	212	35	15

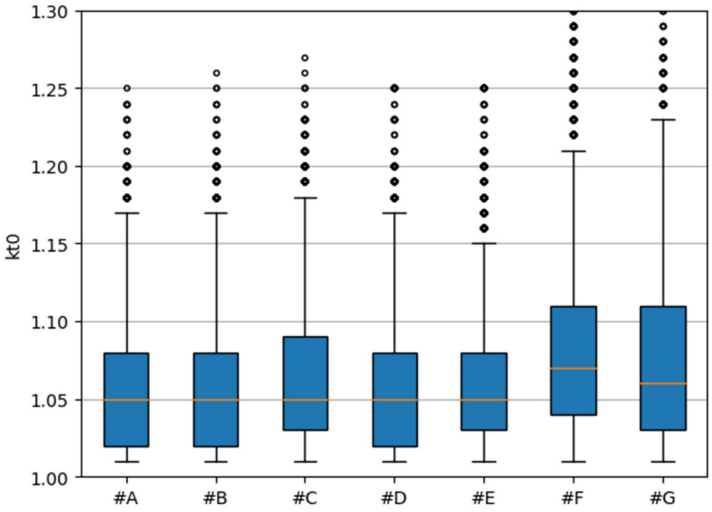
Source: elaborated by the author.

Figure 30 - Boxplot for measured irradiance during extreme overirradiance events, for radiometers ***#A*** (SMP22), ***#B*** (SMP22), ***#C*** (SMP11), ***#D*** (SR20-T1), ***#E*** (MS-80), ***#F*** (SPN1), ***#G*** (SI02PT100).



Source: elaborated by the author.

Figure 31 - Boxplot for calculated kt0 from measured irradiance during extreme overirradiance events, for radiometers #A (SMP22), #B (SMP22), #C (SMP11), #D (SR20-T1), #E (MS-80), #F (SPN1), #G (SI02PT100).



Source: elaborated by the author.

Initially, it is possible to notice the same patterns for the previous subsection occur. Sensor ***#C*** still has the best performance among the Class A pyranometers; however, its total events became a lot similar to the other sensors, reinforcing the fact that its higher uncertainty could be playing an important role when assessing low irradiance cloud enhancement events. Furthermore, ***#A***, ***#B***, ***#D,*** and ***#E*** obtained similar results, where ***#E*** maintained its best general performance among these four radiometers, as well as having the best results for high-frequency data acquisition.

Furthermore, sensor ***#F*** has measured a similar number of events than ***#G***, reducing significantly the over-identification of events; thus, demonstrating, once more, that its supposedly outstanding results are a consequence of its high uncertainty. Nevertheless, ***#F*** results are interesting, it is not reasonable to accept them as a good performance. Therefore, it would be a conservative decision to consider that SPN1 (***#F***) is not suitable to be compared with the other sensors in this specific sub-section.

Generally, all sensors performed much better for extreme irradiance events, even the poorest performance identified around 91% of the measured events of reference ***#G***, whilst these values were around 50% for overirradiance events.

4.4.3 Response time assessment

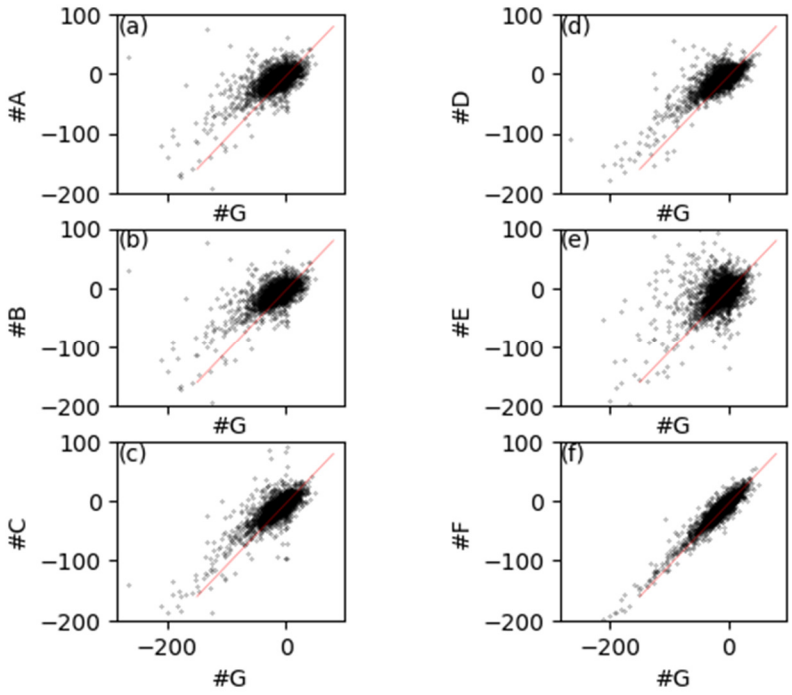
In this section, the aim is to assess the response time of each sensor in accordance with reference ***#G***. In order to do it, the variability rate of specific points are used, which is calculated throughout the second derivative. Moreover, these results will provide a qualitative output, illustrating which sensor has a faster response than the other one. As the aim is to observe the variability rate, uncertainties and specific measurement results have a reduced influence.

To calculate the second derivative, reference ***#G*** events were used. Thus, it was possible to calculate each variability rate for measurements with a clearness index bigger than one.

4.4.3.1 Overirradiance (OIR) Events

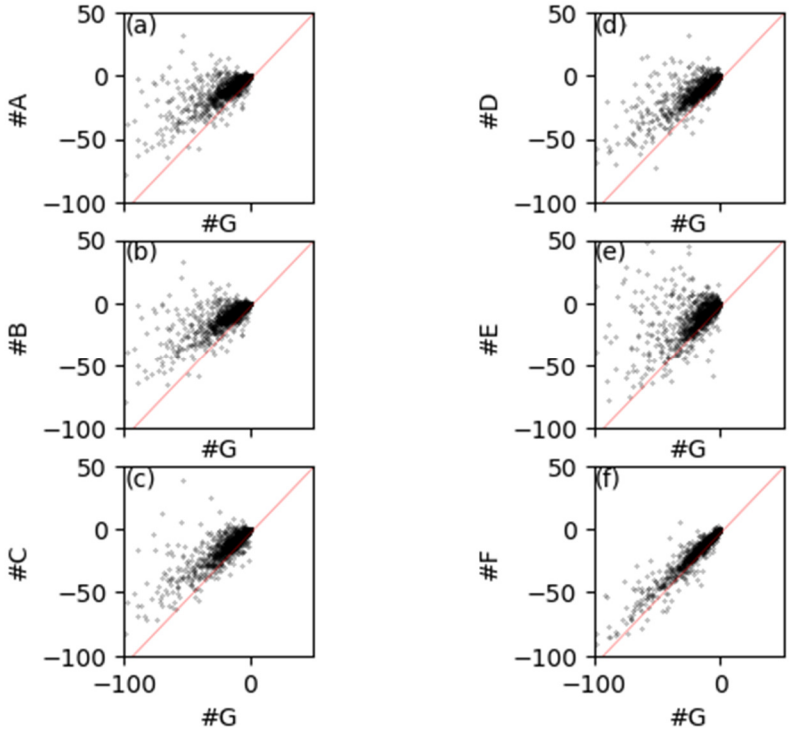
The results for the sensors' second order derivative are displayed in the scatterplots below:

Figure 32 - Scatterplots, relating the second derivate of each sensor to reference ***#G*** (SI02PT100), for overirradiance events. ((a) For sensor ***#A*** (SMP22); (b) For sensor ***#B*** (SMP22); (c) For sensor ***#C*** (SMP11); (d) For sensor ***#D*** (SR20-T1); (e) For sensor ***#E*** (MS-80); (f) For sensor ***#F*** (SPN1)).



Source: elaborated by the author.

Figure 33 - Scatterplots graphs, showing the average of the second derivative of each event. Relating each sensor to the reference ***#G*** (SI02PT100), for overirradiance events. ((a) For sensor ***#A*** (SMP22); (b) For sensor ***#B*** (SMP22); (c) For sensor ***#C*** (SMP11); (d) For sensor ***#D*** (SR20-T1); (e) For sensor ***#E*** (MS-80); (f) For sensor ***#F*** (SPN1)).



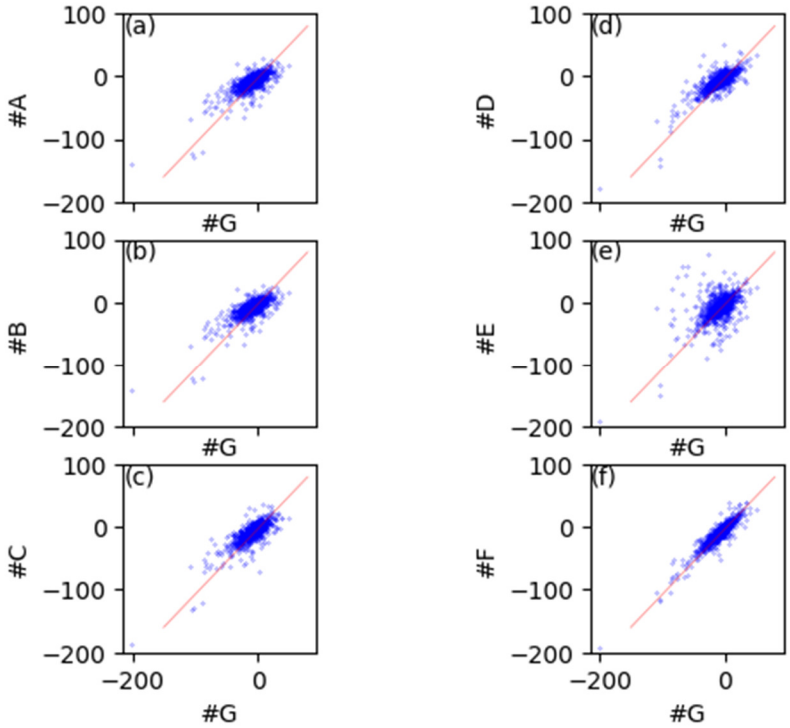
Source: elaborated by the author.

The scatterplot results illustrated that ***#F*** appears to have the fastest response concerning the other sensors, as its data points follow quite precisely the reference line. Furthermore, ***#A***, ***#B***, ***#C,*** and ***#D*** presented very similar formations, being possible to infer that the dataset provides a less inclined curve in relation to the reference, thus possessing a slower time response. In addition, even though sensor ***#E*** has a variation alongside the mean values, it is visible that its values are aligned alongside the reference line, demonstrating a faster response behavior in relation to the other Class A radiometric sensors.

4.4.3.2Extreme Overirradiance (EOIR) Events

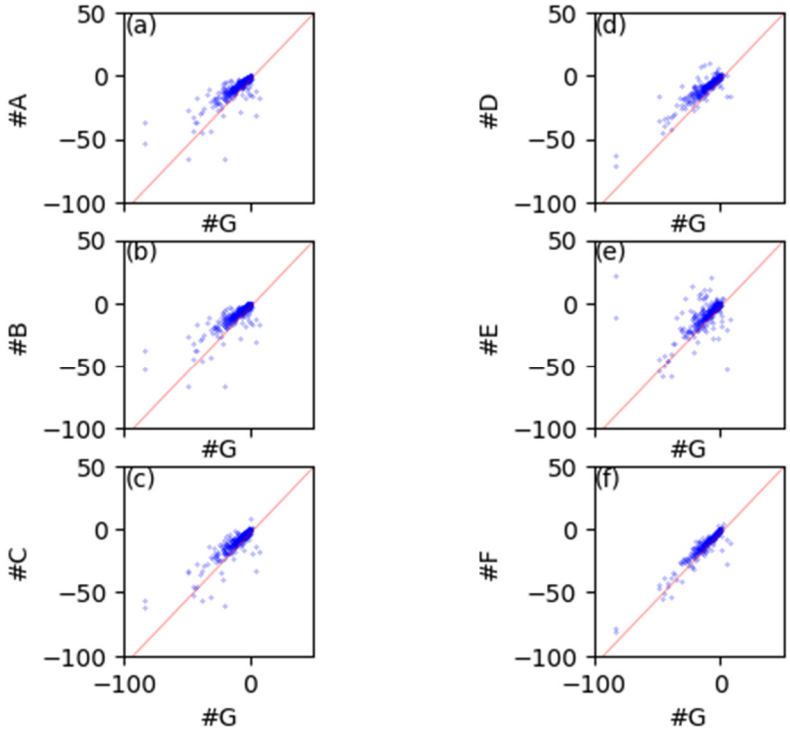
The results below demonstrate the sensors' second order derivative for extreme overirradiance events, which is displayed throughout scatterplots.

Figure 34 - Scatterplots, relating the second derivate of each sensor to reference ***#G*** (SI02PT100), for extreme overirradiance events. ((a) For sensor ***#A*** (SMP22); (b) For sensor ***#B*** (SMP22); (c) For sensor ***#C*** (SMP11); (d) For sensor ***#D*** (SR20-T1); (e) For sensor ***#E*** (MS-80); (f) For sensor ***#F*** (SPN1)).



Source: elaborated by the author.

Figure 35 - Scatterplots graphs, showing the average of the second derivative of each event. Relating each sensor to the reference ***#G*** (SI02PT100), for extreme overirradiance events. ((a) For sensor ***#A*** (SMP22); (b) For sensor ***#B*** (SMP22); (c) For sensor ***#C*** (SMP11); (d) For sensor ***#D*** (SR20-T1); (e) For sensor ***#E*** (MS-80); (f) For sensor ***#F*** (SPN1)).



Source: elaborated by the author.

The results obtained in this section aggregate to the ones displayed in section 4.4.3.1, as a matter of fact, ***#F*** demonstrates an undoubtedly faster response in relation to the other sensor. The other five pyranometers do not show great differences among them. In the case of ***#E***, the scatterplot pattern illustrates that, despite the existence of dispersed values, its results are aligned with the reference line, in red. In addition, ***#A, #B***, ***#C,*** and ***#D*** have similar scatterplots illustrations, thus not being possible to visually assess which one would be faster than the other.

4.4.4 Results Overview

When observing general overirradiance events it was clear that higher uncertainties can cause misinterpretation of sensor behavior. Lower irradiance events can generate dubious data for radiometers with high expanded uncertainty. This can be explained because overirradiance events at lower irradiance commonly occur near sunrise and sunset, as

extraterrestrial horizontal irradiance has a lower magnitude, allowing small deviations to be identified as an event. Even though the directional error was used in this work as a constant, it is widely known that it has exponential behavior for high zenith angles, causing the sensor to be less accurate. Furthermore, as it was observed from results in section 4.2, the individual expanded uncertainty has a significant increase at lower irradiance, due to the data acquisition uncertainty source. Therefore, it can be concluded that as imprecise as the radiometer is, harder is to truly identify an overirradiance event, especially at lower irradiances.

In addition, due to the facts discussed in the last paragraph, further analysis should be taken into account when characterizing the behavior of radiometers for overirradiance events. Thus, stratifying the results for zenith angle ranges and assuming a variable directional error would be an interesting topic to improve this methodology. However, it will be left for future works. Besides, the extreme overirradiance events will be more relevant when evaluating sensors' overirradiance assessment characteristics, as it occurs at higher irradiances and smaller zenith angles, diminishing the associated error previously discussed.

Moreover, due to its notably poor uncertainty, sensor ***#F*** cannot be properly evaluated whilst identifying such events. In addition, pyranometer ***#C*** presented itself as the aptest to observe such events, although the same caveats for sensor ***#F*** imply, however to a much smaller degree.

Pyranometer ***#E*** represents the second position when observing general and extreme overirradiance events; in addition, ***#E*** has achieved the best performance when assessing high-frequency measurements. Furthermore, radiometers ***#A***, ***#B,*** and ***#D*** have presented very similar results, especially when assessing extreme overirradiance events. Thus, all three will be accounted for the third best performance.

Radiometric sensors response time is a difficult metric to be assessed throughout general measurements, even a time resolution of one second could not be fast enough to generate comparable results, as most of the pyranometers have very similar response time, usually ranging from 0,5 to 4 seconds.

However, the second derivative presented itself as a robust evaluation metric, generating results in accordance with what was provided by manufacturers. Uncertainties and spectral range variation are embedded in each sensor measurement; however, in order to assess the response time, it was assumed that, due to the high amount of second derivatives calculated, the random part of the data would be diminished, demonstrating essentially the response time behavior in relation to the ***#G***.

It can be concluded that ***#F*** achieved the fastest response among the pyranometers. Moreover, ***#E*** will be considered to be the second fastest pyranometer, since the scatterplot illustrated its behavior alongside the reference line, much more visible than for any other Class A pyranometer.

#A, ***#B***, ***#C,*** and ***#D*** presented very similar patterns. Their deviations among each other are not clear, especially for individual values assessment. Therefore, these four radiometers will be designated as the third fastest pyranometers.

As results and discussion were stated, it is important to readdress an aspect presented at the beginning of this section, regarding the irradiance measurement of $1845{,}5_{[W/m^2]}$ done by SPN1 (***#F***). As it was stated, this sensor is not a precise equipment, in comparison to the other pyranometers, and its data should be available carefully. However, throughout section 4.4.3 results and discussions it was conclusive, according to the available evaluation metric, that ***#F*** is the pyranometer with the fastest response time on-site. Therefore, as the other sensors are not capable to attend such a response time, is recommended that this unique measurement is considered to be valid, despite ***#F***'s high expanded uncertainty. Thus, it is important to emphasize that whilst there is not a more precise and faster response pyranometer on-site, it is not possible to affirm whether the measurement was either smaller or higher than what was observed by SPN1.

Furthermore, the section 3.4.4 proposed ranking metric was done with the acquired results.

Table 20 - Respective position of each sensor in relation to the evaluation metric, for radiometers ***#A*** (SMP22), ***#B*** (SMP22), ***#C*** (SMP11), ***#D*** (SR20-T1), ***#E*** (MS-80), ***#F*** (SPN1).

Sensor	Expanded Uncertainty	Phenomena Observation	Time response	Equivalency	Total Points
#A	2nd	3rd	3rd	Yes	30
#B	1st	3rd	3rd	Yes	32
#C	5th	1st	3rd	Yes	28
#D	4th	3rd	3rd	Yes	26
#E	3rd	2nd	2nd	Yes	32
#F	6th	4th	1st	No	14

Source: elaborated by the author.

In order to untie the results, as all metrics are considered to have the same weight, the sensor who performed better in most of the metrics will be granted the best position. Thus, as

MS-80 (***#E***) has performed better than ***#B*** in most part of the metrics, it will be considered the pyranometer who possess the best behavior, or characteristics, in order to assess overirradiance and extreme overirradiance events.

Table 21 - Ranking for best behavior pyranometer in order to characterize overirradiance events, for radiometers ***#A*** (SMP22), ***#B*** (SMP22), ***#C*** (SMP11), ***#D*** (SR20-T1), ***#E*** (MS-80), ***#F*** (SPN1).

Position	Sensor
1st	***#E***
2nd	***#B***
3rd	***#A***
4th	***#C***
5th	***#D***
6th	***#F***

Source: elaborated by the author.

4.4.5 Seasonal proportion of overirradiance events as % fraction accumulated energy over the year

The seasonal proportion of overirradiance events were extracted from the dataset and displayed in the tables below.

Table 22 - Percentual fraction of accumulated energy for general and extreme overirradiance events, stratified for each season, for measured data of pyranometer ***#E*** (MS-80).

Sensor: ***#E***		
Season	Overirradiance Events	Extreme Overirradiance Events
Summer	0,72%	0,30%
Autumn	0,42%	0,00%
Winter	0,30%	0,00%
Spring	0,73%	0,35%
All	0,55%	0,17%

Source: elaborated by the author.

Table 23 - Percentual fraction of accumulated energy for general and extreme overirradiance events, stratified for each season, for measured data of reference cell ***#G*** (SI02PT100).

Sensor: ***#G***

Season	Overirradiance Events	Extreme Overirradiance Events
Summer	3,11%	0,68%
Autumn	0,75%	0,01%
Winter	0,45%	0,00%
Spring	1,39%	0,66%
All	0,78%	0,34%

Source: elaborated by the author.

Initially, it is possible to observe, the already discussed fact, that a photodiode identifies around 50% more overirradiance events than a pyranometer. In this case, this situation is emphasized in the summer months for general overirradiance events. However, extreme events maintain this ratio almost constant. Furthermore, as a consequence, Table 22 and Table 23 show that it affects the site energy assessment, as ***#G*** demonstrates a bigger contribution of these events in the accumulated energy over the year.

As expected, summer and spring represent the biggest fraction of overirradiance energy, which can be especially related to its sky conditions. Moreover, in the accumulated energy point of view, extreme overirradiance events are irrelevant in winter and autumn.

Furthermore, it is possible to conclude that for the site of Florianópolis, Brazil, the season affects significantly the parcel of energy generated by overirradiance events. An important aspect, that can be inferred from the tables, is that months with higher insolation are more affected by extreme overirradiance events, which could impact PV power plants operation whilst they should be producing power at a high rate. However, its percentual fraction over a year can be up to 0,78%; therefore it cannot be seen as relevant when focusing only on these events' available energy contribution.

5 CONCLUSION

To conclude, this work presented several important aspects of six pyranometers and one photodiode installed at Florianópolis, Brazil. The work characterized the expanded uncertainties of each sensor, throughout the SOLARUN Application, using uncertainty source data provided by calibration certificates, datasheets, and from previous research studies. Class A pyranometers on-site were found to be very accurate, achieving 1,3% of expanded uncertainty for ***#B***. However, the most unprecise sensor, ***#F***, had an uncertainty of 11,4%.

Two different methodologies were developed and applied. The first one, in order to evaluate statistically which of the sensors measures equivalently as the most stable and accurate sensor on-site, ***#A***. The second one provided a methodology to characterize the behavior of pyranometers when observing overirradiance events. Thus, characterizing the capacity of phenomena observation and the response time of each sensor, in accordance with the reference cell (***#G***) results.

Finally, an important conclusion of this work is that sensor **#E**, a MS-80 model is the most capable pyranometer on-site to identify overirradiance and extreme overirradiance events.

In addition, an irradiance value of 1845,5 $_{[W/m^2]}$ is reported to be measured by ***#F*** in this work, thus marking a new second highest irradiance measurement in the literature; an important aspect of this measurement is that it was measured at an altitude of 6$_{[m]}$, thus having no benefit of reduced atmospheric absorption. Thus, showing a new pattern of overirradiance measurements, which have started to be reported more often in recent years (do Nascimento et al., 2019; Gueymard, 2017a; Yordanov et al., 2015).

Moreover, the percentual fraction of accumulated energy for overirradiance events over a year is around 0,7%, not being so relevant for a year energy generation. However, these events are more common during summer and spring, which are the seasons that generate more energy; thus, fuse blows or other damages caused by extreme irradiance events (do Nascimento et al., 2019) could impact more significantly a local PV power plant generation.

6 RECOMMENDATIONS FOR FUTURE WORKS

For future works, the author recommends the implementation of SPN1 calibration procedures available in the literature (Badosa et al., 2014; Möllenkamp et al., 2020). Thus, with an improvement in uncertainty results, it would be possible to reassess the methodology, which could generate better results for this respective sensor.

An evaluation of the effect of overirradiance events in the irradiance spectrum would further complement the analysis; thus, being able to determine how energy in different wavelengths variates when an overirradiance event occur.

A better characterization of directional error would be interesting in order to assess cosine error deviations for different azimuthal and zenithal angles. Thus, providing an even more precise uncertainty characterization.

Besides, an improvement in methodology could be done by analyzing error metrics throughout different zenith angle ranges and separate sky conditions. Moreover, both overirradiance events identification and response time assessment could benefit from this stratified analysis.

In addition, the methodology developed in this work should be tested for different sites and sensors, to validate it for different environmental conditions. Furthermore, a local characterization of overirradiance events throughout the years could be done utilizing the best-ranked sensor, however, is necessary more data to be available to do such an analysis.

In order to evaluate the cost-benefit of sensors, both methodologies could be adapted to assess the sensor performances in relation to cost. However, it would be interesting that more Class B and C pyranometers to be added to the analyses.

REFERENCES

Al-Rasheedi, M., Gueymard, C.A., Ismail, A., Hussain, T., 2018. Comparison of two sensor technologies for solar irradiance measurement in a desert environment. Sol. Energy 161, 194–206. https://doi.org/10.1016/j.solener.2017.12.058

Albertazzi, A.;, Souza, A.R., 2013. Fundamentos de Metrologia Científica e Industrial, 3rd ed.

Almeida, M.P., Zilles, R., Lorenzo, E., 2014. Extreme overirradiance events in São Paulo, Brazil. Sol. Energy 110, 168–173. https://doi.org/10.1016/j.solener.2014.09.012

Alvares, C.A., Stape, J.L., Sentelhas, P.C., de Moraes Gonçalves, J.L., Sparovek, G., 2013. Köppen's climate classification map for Brazil. Meteorol. Zeitschrift 22, 711–728. https://doi.org/10.1127/0941-2948/2013/0507

Azouzoute, A., Merrouni, A.A., Bennouna, E.G., Gennioui, A., Azouzoute, A., Alami, A., Pina, A., Ferrão, P., Fournier, J., Lacarrière, B., Corre, O. Le, 2019. Accuracy Measurement of Pyranometer vs Reference cell for PV resource assessment. Energy Procedia 157, 1202–1209. https://doi.org/10.1016/j.egypro.2018.11.286

Badosa, J., Wood, J., Blanc, P., Long, C.N., Vuilleumier, L., Demengel, D., Haeffelin, M., 2014. Solar irradiances measured using SPN1 radiometers: Uncertainties and clues for development. Atmos. Meas. Tech. 7, 4267–4283. https://doi.org/10.5194/amt-7-4267-2014

Balfour, J., Shaw, M., Nash, N.B., 2011. Introduction to Photovoltaic System Design. Jones & Bartlett Learning.

Braga, M., De Oliveira, A.K. V, Burnham, L., Dittmann, S., Gottschalg, R., Betts, T., Rodríguez-Gallegos, C.D., Reindl, T., Rüther, R., 2020. Solar Over-Irradiance Events: Preliminary Results from a Global Study, in: Conference Record of the IEEE Photovoltaic Specialists Conference. IEEE.

Brinkworth, B.J., Hughes, T.D.R., 1976. Accelerated response of thermopile pyranometers. Sol. Energy 18, 403–404. https://doi.org/10.1016/0038-092X(76)90005-0

Burger, B., Rüther, R., 2006. Inverter sizing of grid-connected photovoltaic systems in the light of local solar resource distribution characteristics and temperature. Sol. Energy 80, 32–45. https://doi.org/10.1016/j.solener.2005.08.012

Calaza, C., Rubio, R., Santander, J., 2004. Thermal AFM : a thermopile case study 101, 153–159. https://doi.org/10.1016/j.ultramic.2004.05.004

Canfield, L.R., 1999. Photodiode Detectors. Vac. Ultrav. Spectrosc. 117–138. https://doi.org/10.1016/b978-012617560-8/50028-1

Chen, S., Li, P., Brady, D., Lehman, B., 2013. Determining the optimum grid-connected photovoltaic inverter size. Sol. Energy 87, 96–116. https://doi.org/10.1016/j.solener.2012.09.012

Denholm, P., Margolis, R.M., 2007a. Evaluating the limits of solar photovoltaics (PV) in traditional electric power systems. Energy Policy 35, 2852–2861. https://doi.org/10.1016/j.enpol.2006.10.014

Denholm, P., Margolis, R.M., 2007b. Evaluating the limits of solar photovoltaics (PV) in electric power systems utilizing energy storage and other enabling technologies. Energy Policy 35, 4424–4433. https://doi.org/10.1016/j.enpol.2007.03.004

Dittmann, S., Friesen, G., Strepparava, D., Meoli, R., Domine, D., Burà, E., Chianese, D., 2011. Energy Yield Measurements at SUPSI -- Importance of Data Quality Control and Its Influence on kWh/Wp Inter-Comparison: 6 pages / 26th European Photovoltaic Solar Energy Conference and Exhibition; 3629-3634 / 26th European Photovoltaic Solar Energy Confere. 26th Eur. Photovolt. Sol. Energy Conf. Exhib. 3629–3634.

https://doi.org/10.4229/26thEUPVSEC2011-4AV.2.47
Do Nascimento, L.R., Braga, M., Campos, R.A., Naspolini, H.F., Rüther, R., 2020. Performance assessment of solar photovoltaic technologies under different climatic conditions in Brazil. Renew. Energy 146, 1070–1082. https://doi.org/10.1016/j.renene.2019.06.160
do Nascimento, L.R., Viana, T.D.S., Campos, R.A., Rüther, R., de Souza Viana, T., Campos, R.A., Rüther, R., 2019. Extreme solar overirradiance events: Occurrence and impacts on utility-scale photovoltaic power plants in Brazil. Sol. Energy 186, 370–381. https://doi.org/10.1016/j.solener.2019.05.008
Gueymard, C.A., 2017a. Cloud and albedo enhancement impacts on solar irradiance using high-frequency measurements from thermopile and photodiode radiometers. Part 1: Impacts on global horizontal irradiance. Sol. Energy 153, 755–765. https://doi.org/10.1016/j.solener.2017.05.004
Gueymard, C.A., 2017b. Cloud and albedo enhancement impacts on solar irradiance using high-frequency measurements from thermopile and photodiode radiometers. Part 2: Performance of separation and transposition models for global tilted irradiance. Sol. Energy 153, 766–779. https://doi.org/10.1016/j.solener.2017.04.068
Habte, A.., Sengupta, M.., Reda, I.., Andreas, A.., Konings, J., 2014. Calibration and Measurement Uncertainty Estimation of Radiometric Data: Preprint.
Habte, A., Sengupta, M., Andreas, A., Wilcox, S., Stoffel, T., 2016. Intercomparison of 51 radiometers for determining global horizontal irradiance and direct normal irradiance measurements. Sol. Energy 133, 372–393. https://doi.org/10.1016/j.solener.2016.03.065
Haskell, R.C., Svaasand, L.O., Tsay, T.-T., Feng, T.-C., Tromberg, B.J., McAdams, M.S., 1994. Boundary conditions for the diffusion equation in radiative transfer. J. Opt. Soc. Am. A 11, 2727. https://doi.org/10.1364/josaa.11.002727
Hauschke, D., Kieser, M., Diletti, E., Burke, M., 1999. Sample size determination for proving equivalence based on the ratio of two means for normally distributed data. Stat. Med. 18, 93–105. https://doi.org/10.1002/(SICI)1097-0258(19990115)18:1<93::AID-SIM992>3.0.CO;2-8
Ineichen, P., Perez, R., 2002. A new airmass independent formulation for the Linke turbidity coefficient. Sol. Energy 73, 151–157. https://doi.org/10.1016/S0038-092X(02)00045-2
IngineurBuro Mencke & Tegtmeyer GmbH, 2016. Silicon Irradiance Sensor.
Inman, R.H., Chu, Y., Coimbra, C.F.M., 2016. Cloud enhancement of global horizontal irradiance in California and Hawaii. Sol. Energy 130, 128–138. https://doi.org/10.1016/j.solener.2016.02.011
Institute for Energy Solutions | [WWW Document], n.d. URL https://energy.arizona.edu/ (accessed 8.6.20).
International Organization for Standardization, 2018. ISO9060:2018 - Solar energy - Specification and classification of instruments for measuring hemispherical solar and direct solar radiation.
International Organization for Standardization, 1998. ISO9847:1992- Solar Energy - Calibration of field pyranometers by comparison to a reference pyranometer.
Iqbal, M., 1983. An Introduction to Solar Radiation. ACADEMIC PRESS CANADA.
Järvelä, M., Lappalainen, K., Valkealahti, S., 2020. Characteristics of the cloud enhancement phenomenon and PV power plants. Sol. Energy 196, 137–145. https://doi.org/10.1016/j.solener.2019.11.090
Kaminski, L., Schepers, U., Wätzig, H., 2010. Analytical method transfer using equivalence tests with reasonable acceptance criteria and appropriate effort: Extension of the ISPE concept. J. Pharm. Biomed. Anal. 53, 1124–1129.

https://doi.org/10.1016/j.jpba.2010.04.034
King, M.L., Zhang, X., Akram, M., 2020. Hypothesis testing based on a vector of statistics. J. Econom. https://doi.org/10.1016/j.jeconom.2020.03.010
Kipp & Zonnen, 2015. Pyranometers for the Accurate Measurement of Solar Irradiance.
Konings, J., Habte, A., 2015. Uncertainty evaluation of measurements with pyranometers and pyrheliometers, in: ISES Solar World Congress 2015, Conference Proceedings. pp. 268–278. https://doi.org/10.18086/swc.2015.07.15
Kratzenberg, M.G., Beyer, H.G., Colle, S., Albertazzi, A., 2006. Uncertainty calculations in pyranometer measurements and application, in: International Solar Energy Conference. https://doi.org/10.1115/ISEC2006-99168
Lappalainen, K., Kleissl, J., 2020. Analysis of the cloud enhancement phenomenon and its effects on photovoltaic generators based on cloud speed sensor measurements. J. Renew. Sustain. Energy 12, 043502. https://doi.org/10.1063/5.0007550
Long, C.N., Dutton, E.G., n.d. BSRN Global Network recommended QC tests, V2, BSRN.
Luoma, J., Kleissl, J., Murray, K., 2012. Optimal inverter sizing considering cloud enhancement. Sol. Energy 86, 421–429. https://doi.org/10.1016/j.solener.2011.10.012
Mantelli, S.L.N., Martins, G.L., Ruther, R., 2020. Uncertainty analysis of solar monitoring station: A case study, in: Proceedings of the ISES Solar World Congress 2019 and IEA SHC International Conference on Solar Heating and Cooling for Buildings and Industry 2019. pp. 2135–2140. https://doi.org/10.18086/swc.2019.44.03
MINITAB LLC, 2020a. Métodos e fórmulas para Média de teste - média de referência para Teste de Equivalência com Dados Pareados - Minitab [WWW Document]. URL https://support.minitab.com/pt-br/minitab/19/help-and-how-to/statistics/equivalence-tests/how-to/equivalence-test-with-paired-data/methods-and-formulas/test-mean---reference-mean/ (accessed 8.10.20).
MINITAB LLC, 2020b. Métodos e fórmulas para Média de teste / média de referência para Teste de Equivalência com Dados Pareados [WWW Document]. URL https://support.minitab.com/pt-br/minitab/19/help-and-how-to/statistics/equivalence-tests/how-to/equivalence-test-with-paired-data/methods-and-formulas/test-mean-reference-mean/ (accessed 10.23.20).
Möllenkamp, J., Beikircher, T., Häberle, A., 2020. Recalibration of SPN1 pyranometers against pyrheliometer and its relevance for the evaluation of concentrating solar process heat plants. Sol. Energy 197, 344–358. https://doi.org/10.1016/j.solener.2019.12.055
Montgomery, D.C., Runger, G.C., 2014. Applied Statistics and Probability for engineers, 6th ed, European Journal of Engineering Education. John Wiley & Sons, Inc. https://doi.org/10.1080/03043799408928333
MS-80 Pyranometer | EKO Instruments [WWW Document], n.d. URL https://eko-eu.com/products/solar-energy/pyranometers/ms-80-pyranometer (accessed 9.4.20).
National Renewable Energy Laboratory (NREL), 2019. SolarResourceTools/Solar Resource Uncertainty (SOLARUN) [WWW Document]. URL https://github.com/NREL/SolarResourceTools/tree/master/Solar Resource Uncertainty (SOLARUN) Application (accessed 8.7.20).
Nelson, D., 2006. a Review of Reference Radiation Scale Transfer To Broadband Radiation Program and Its Predecessors.
Norris, D.J., 1968. Correlation of Solar Radiation with Clouds 12, 107–112.
Package Overview — pvlib-python 0.7.2+0.gb35905a.dirty documentation [WWW Document], n.d. URL https://pvlib-python.readthedocs.io/en/stable/package_overview.html (accessed 8.6.20).
Pecenak, Z.K., Mejia, F.A., Kurtz, B., Evan, A., Kleissl, J., 2016. Simulating irradiance

enhancement dependence on cloud optical depth and solar zenith angle. Sol. Energy 136, 675–681. https://doi.org/10.1016/j.solener.2016.07.045

Peel, M.C., Finlayson, B.L., McMahon, T.A., 2007. Updated world map of the Köppen-Geiger climate classification. Hydrol. Earth Syst. Sci. 11, 1633–1644. https://doi.org/10.5194/hess-11-1633-2007

Piacentini, R.D., Cede, A., Bárcena, H., 2003. Extreme solar total and UV irradiances due to cloud effect measured near the summer solstice at the high-altitude desertic plateau Puna of Atacama (Argentina). J. Atmos. Solar-Terrestrial Phys. 65, 727–731. https://doi.org/10.1016/S1364-6826(03)00084-1

Piacentini, R.D., Salum, G.M., Fraidenraich, N., Tiba, C., 2011. Extreme total solar irradiance due to cloud enhancement at sea level of the NE Atlantic coast of Brazil. Renew. Energy 36, 409–412. https://doi.org/10.1016/j.renene.2010.06.009

Reda, I., 2011. Method to Calculate Uncertainties in Measuring Shortwave Solar Irradiance Using Thermopile and Semiconductor Solar Radiometers, NREL.

Reda, I., Myers, D., Stoffel, T., 2008. Uncertainty Estimate for the Outdoor Calibration of Solar Pyranometers: A Metrologist Perspective, NCSLI Measure. https://doi.org/10.1080/19315775.2008.11721448

Ruther, R., Nascimento, L.R. do, Campos, R.A., 2017. Performance assessment issues in utility-scale photovoltaics in warm and sunny climates. Renew. Energy Environ. Sustain. 2, 35. https://doi.org/10.1051/rees/2017035

Sandia National Laboratories: Exceptional Service in the National Interest [WWW Document], 2020. URL https://www.sandia.gov/ (accessed 8.6.20).

Schade, N.H., Macke, A., Sandmann, H., Stick, C., 2007. Enhanced solar global irradiance during cloudy sky conditions. Meteorol. Zeitschrift 16, 295–303. https://doi.org/10.1127/0941-2948/2007/0206

Segal, M.., Davis, J., 1992. The Impact of Deep Cumulus Reflection on the Ground-Level Global Irradiance. Am. Meteorol. Soc. 6–8. https://doi.org/10.16309/j.cnki.issn.1007-1776.2003.03.004

Singh, S.K., Yadav, M.K., Khandekar, S., 2017. Measurement issues associated with surface mounting of thermopile heat flux sensors. Appl. Therm. Eng. 114, 1105–1113. https://doi.org/10.1016/j.applthermaleng.2016.12.076

SONDA - Validação dos Dados [WWW Document], n.d. URL http://sonda.ccst.inpe.br/infos/validacao.html (accessed 8.6.20).

Suehrcke, H., McCormick, P.G., 1988. The diffuse fraction of instantaneous solar radiation. Sol. Energy 40, 423–430. https://doi.org/10.1016/0038-092X(88)90097-7

Thapa, S., Mahesh, S., Guilbeau, E.J., Crews, N.D., 2012. Sensors and Actuators A : Physical The thermopile : An anisotropic temperature sensor. Sensors Actuators A. Phys. 187, 132–140. https://doi.org/10.1016/j.sna.2012.08.006

The Importance of Pyranometer Temperature Response - Kipp & Zonen [WWW Document], 2015. URL https://www.kippzonen.com/News/582/The-Importance-of-Pyranometer-Temperature-Response#.Xyr6cogzapo (accessed 8.5.20).

Thuillier, G., Perrin, J.-M., Keckhut, P., Huppert, F., 2013. Local enhanced solar irradiance on the ground generated by cirrus: measurements and interpretation. J. Appl. Remote Sens. 7, 073543. https://doi.org/10.1117/1.jrs.7.073543

UDT Sensors Inc, 1982. Silicon Photodiodes, Univie.

Vamvakas, I., Salamalikis, V., Kazantzidis, A., 2020. Evaluation of enhancement events of global horizontal irradiance due to clouds at Patras, South-West Greece. Renew. Energy 151, 764–771. https://doi.org/10.1016/j.renene.2019.11.069

Webb, N., 2020. Sales enquiry via the Delta-T website form - help to answer questions please

...
Wirth, G., Lorenz, E., Spring, A., Becker, G., Pardatscher, R., Witzmann, R., 2015. Modeling the maximum power output of a distributed PV fleet. Prog. Photovoltaics Res. Appl. 23, 1164–1181. https://doi.org/10.1002/pip.2513
Yordanov, G.H., 2015. A study of extreme overirradiance events for solar energy applications using NASA's I3RC Monte Carlo radiative transfer model. Sol. Energy 122, 954–965. https://doi.org/10.1016/j.solener.2015.10.014
Yordanov, G.H., Saetre, T.O., Midtgard, O.-M., 2014. 1.6 suns at 58°20′N - the solar resource in Southern Norway, in: 2014 IEEE 40th Photovoltaic Specialist Conference (PVSC). IEEE, pp. 0815–0820. https://doi.org/10.1109/PVSC.2014.6925040
Yordanov, G.H., Saetre, T.O., Midtgård, O.M., 2015. Extreme overirradiance events in Norway: 1.6 suns measured close to 60°N. Sol. Energy 115, 68–73. https://doi.org/10.1016/j.solener.2015.02.020